HU ISSN 1586–2070

JOURNAL OF COMPUTATIONAL AND APPLIED MECHANICS

An Open Access International Journal

Published by the University of Miskolc

VOLUME 11, NUMBER 2 (2016)

MISKOLC UNIVERSITY PRESS

HU ISSN 1586–2070

JOURNAL OF COMPUTATIONAL AND APPLIED MECHANICS

An Open Access International Journal

Published by the University of Miskolc

VOLUME 11, NUMBER 2 (2016)

MISKOLC UNIVERSITY PRESS

Journal of Computational and Applied Mechanics, Vol. 11., No. 2., (2016), pp. 107–122
DOI: 10.32973/jcam.2016.008

THE DRAG COEFFICIENT IN POWER-LAW NON-NEWTONIAN FLUID OVER MOVING SURFACE

Gabriella Bognár
Institute of Machine and Product Design, University of Miskolc
H-3515 Miskolc-Egyetemváros, Hungary
v.bognar.gabriella@uni-miskolc.hu

[Received: April 17, 2016]

Abstract. This paper deals with a solution to the boundary layer problem of a non-Newtonian power-law fluid flow along a moving flat surface. Two cases are investigated: one when the surface is moving in a fluid flow, the other when the surface is moving through an otherwise quiescent fluid. Applying similarity transformation to the system of the governing partial differential equations, the boundary value problem of one nonlinear ordinary differential equation on $[0,\infty)$ is derived. Numerical solutions obtained for the velocity components and the drag coefficient parameter depending on the velocity ratio and on the power-law exponent are exhibited.

Mathematical Subject Classification: 34B10, 34B15
Keywords: Non-Newtonian fluid, boundary layer, moving surface, similarity method, iterative transformation method, spectral method

Nomenclature

f	[-]	similarity velocity
g	[-]	function
h, h^*	[-]	parameters
K	[Pa s^n]	consistency coefficient
n	[-]	power-law exponent
u, v	[-]	non-dimensional velocity components
U_∞	[m/s]	fluid velocity
U_w	[m/s]	wall velocity
x, y	[-]	non-dimensional variables

Greek symbols

$\gamma, \sigma, \kappa, \mu$	[-]	parameters
Γ	[-]	function
η	[-]	similarity variable
ρ	[kg/m^3]	density of the fluid
ψ	[-]	non-dimensional stream function
τ_{yx}	[Pa]	shear stress

τ_w	[Pa]	wall shear stress
λ	[-]	velocity ratio, U_ω/U_∞
λ_c	[-]	critical velocity ratio

1. Introduction

In fluid dynamics, the drag force or force component in the direction of the flow velocity is proportional to the drag coefficient, to the density of the fluid, to the area of the object and the square of the relative speed between the object and the flow velocity. Blasius applied the similarity method to investigate the model arising for a laminar boundary layer of a Newtonian media [1]. Fluids such as molten plastics, pulps, slurries and emulsions, which do not obey the Newtonian law of viscosity, are increasingly produced in the industry. The first analysis of the boundary layer approximations to non-Newtonian media with power-law viscosity was published by Schowalter [2] in 1960. The author derived the equations governing the fluid flow. Numerical solutions to the problem of a laminar flow of the non-Newtonian power-law model past a two-dimensional horizontal surface were presented by Acrivos at al. [3]. When the geometry of the surface is simple the system of differential equations can be examined in details and fundamental information can be obtained about the flow behavior of a non-Newtonian fluid in motion (e.g., to predict the drag).

The production of sheeting material, which includes both metal and polymer sheets, arises in a number of industrial manufacturing processes. The fluid dynamics due to a continuous moving solid surface appears in aerodynamic extrusion of plastic sheets, cooling of a metallic plate in a cooling bath, the boundary layer along material handling conveyers, boundary layer along a liquid film in condensation processes, etc. Much theoretical work has been done on this problem since the pioneering papers by Sakiadis [4] and Tsou et al. [5], and extensive references can be found in the papers by Magyari and Keller [6], [7], Liao and Pop [8], and Nazar et al. [9].

Various types of non-Newtonian fluids are nano fluid, Casson fluid, viscoelastic fluid, couple stress fluid, micro polar fluid, power-law flow, etc. [10]. These include pseudo plastic, dilatant, blood, foodstuff, slurries, paints, cosmetics and toiletries. Heat transfer in boundary layer over a stretching sheet has important applications in extrusion of plastic sheets, polymer, spinning of fibers, cooling of elastic sheets, etc. ([11], [12], [13]). The MHD boundary layer flow of heat and mass transfer problems about an stretching sheet have become important research topics in view of its significant applications in industrial manufacturing processes such as plasma studies, petroleum industries, magneto-hydrodynamics power generator, cooling of nuclear reactors, boundary layer control in aerodynamics, glass fiber production and paper production ([14], [15]).

Several numerical methods have been developed and introduced for the solution of these type of fluid mechanics' problems. It was shown in [16] that a non-iterative Töpfer-like transformation can be applied for the determination of the dimensionless wall gradient on a stationary flat surface. Due to the challenging problem of the solution of the boundary value problem to nonlinear differential equation(s) on infinite interval, it is beneficial to obtain the solution with different numerical simulations for

comparison. The aims of the paper are to give numerical results on the drag coefficient in non-Newtonian media along moving flat surfaces for two cases and to introduce two numerical methods, an iterative transformation method and a spectral method, for the numerical evaluation.

2. Mathematical Model

Consider an incompressible uniform parallel flow of a non-Newtonian power-law fluid, with a constant velocity U_∞ along an impermeable semi-infinite flat plate whose surface is moving with a constant velocity U_w in the opposite direction to the main stream. The x–axis extends parallel to the plate, while the y-axis extends upwards, normal to it. Applying the necessary boundary layer approximations, the continuity and momentum equations are [17]:

$$\frac{\partial u}{\partial x} + \frac{\partial v}{\partial y} = 0, \tag{2.1}$$

$$u\frac{\partial u}{\partial x} + v\frac{\partial u}{\partial y} = \frac{1}{\rho}\frac{\partial \tau_{yx}}{\partial y}, \tag{2.2}$$

where u, v are the velocity components along x and y coordinates, respectively. The shear stress and the shear rate relation is assumed to be the power-law relation

$$\tau_{yx} = K\left|\frac{\partial u}{\partial y}\right|^{n-1}\frac{\partial u}{\partial y},$$

where K stands for the consistency and n is called the power-law index; that is $n < 1$ for pseudoplastic, $n = 1$ for Newtonian, and $n > 1$ for dilatant fluids. Therefore, differential equation (2.2) is rewritten as

$$u\frac{\partial u}{\partial x} + v\frac{\partial u}{\partial y} = \frac{\partial}{\partial y}\left(\mu_c\left|\frac{\partial u}{\partial y}\right|^{n-1}\frac{\partial u}{\partial y}\right), \tag{2.3}$$

where $\mu_c = K/\rho$.

2.1. **Fluid flow of velocity U_∞.** In the first case, the surface is placed in a fluid flow of velocity U_∞. The wall is impermeable and no-slip boundary condition is supposed. For the investigated model, the boundary conditions are formulated as

$$u|_{y=0} = -U_w, \quad v|_{y=0} = 0, \quad u|_{y=+\infty} = U_\infty. \tag{2.4}$$

2.2. **Flow in an otherwise quiescent fluid.** In the second case, the ambient fluid velocity is zero and we suppose that the plate is moving at a constant velocity; therefore:

$$u|_{y=0} = -U_w, \qquad v|_{y=0} = 0, \qquad u|_{y=+\infty} = 0. \tag{2.5}$$

2.3. **Introduction of stream function.** The continuity equation (2.1) is automatically satisfied by introducing a stream function ψ as

$$u = \frac{\partial \psi}{\partial y}, \tag{2.6}$$

$$v = -\frac{\partial \psi}{\partial x}. \tag{2.7}$$

The momentum equation can be transformed into an ordinary differential equation by the similarity transformations

$$\psi(x,y) = \mu_c^{\frac{1}{n+1}} \left(U_\infty\right)^{\frac{2n-1}{n+1}} x^{\frac{1}{n+1}} f(\eta), \tag{2.8}$$

$$\eta = \mu_c^{-\frac{1}{n+1}} \left(U_\infty\right)^{\frac{2-n}{n+1}} y x^{-\frac{1}{n+1}}, \tag{2.9}$$

where η is the similarity variable and $f(\eta)$ is the dimensionless stream function for the boundary value problem (2.1), (2.3) and (2.4). Equation (2.3) with the transformed boundary conditions can be written as

$$\left(|f''|^{n-1} f''\right)' + \frac{1}{n+1} f f'' = 0, \tag{2.10}$$

$$f(0) = 0, \quad f'(0) = -\lambda, \quad f'(\infty) = \lim_{\eta \to \infty} f'(\eta) = 1, \tag{2.11}$$

where the prime denotes the differentiation with respect to the similarity variable η, and the velocity ratio parameter is $\lambda = U_w/U_\infty$. Equation (2.10) is called the generalized Blasius equation and the case $\lambda = 0$ corresponds to the Blasius problem. It should be noted that for $\lambda > 0$, the fluid and the plate move in opposite directions, while they move in the same directions if $\lambda < 0$. Now, the dimensionless velocity components have the form:

$$u(x,y) = U_\infty f'(\eta), \tag{2.12}$$

$$v(x,y) = \frac{U_\infty}{n+1} Re_x^{\frac{n}{n+1}} (\eta f'(\eta) - f(\eta)), \tag{2.13}$$

and

$$\eta = Re_x^{\frac{1}{n+1}} y/x, \tag{2.14}$$

where

$$Re_x = U_\infty^{2-n} x^n / \mu_c \tag{2.15}$$

is the local Reynolds number.

For $U_\infty = 0$, λ is not defined. Here the momentum equation can be transformed into an ordinary differential equation by the similarity transformations

$$\psi(x,y) = \mu_c^{\frac{1}{n+1}} \left(U_w\right)^{\frac{2n-1}{n+1}} x^{\frac{1}{n+1}} f(\eta), \tag{2.16}$$

$$\eta = \mu_c^{-\frac{1}{n+1}} \left(U_w\right)^{\frac{2-n}{n+1}} y x^{-\frac{1}{n+1}} \tag{2.17}$$

for the boundary value problem (2.1), (2.3) and (2.4). The transformed form of equation (2.3) has the same form as (2.10), but the boundary conditions (2.5) are formed by

$$f(0) = 0, \quad f'(0) = 1, \quad f'(\infty) = \lim_{\eta \to \infty} f'(\eta) = 0. \tag{2.18}$$

The dimensionless velocity components can be given as:

$$u(x,y) = U_w f'(\eta), \quad [v(x,y) = \frac{U_w}{n+1} Re_x^{\frac{n}{n+1}} (\eta f'(\eta) - f(\eta)), \tag{2.19}$$

and

$$\eta = Re_x^{\frac{1}{n+1}}\, y/x, \tag{2.20}$$

where

$$Re_x = U_w^{2-n} x^n / \mu_c. \tag{2.21}$$

Since the pioneering work by Acrivos at al. [3], different approaches have been investigated for $f''(0) = \gamma$ in the case of non-Newtonian fluids. It has a physical meaning in *drag force* or force due to *skin friction*. It is a fluid dynamic resistive force, which is a consequence of the fluid and the pressure distribution on the surface of the object. The *skin friction parameter* γ originates from the non-dimensional *drag coefficient*

$$C_D = (n+1)^{\frac{1}{n+1}}\, Re^{\frac{-n}{n+1}}\, |\gamma|^{n-1}\, \gamma, \tag{2.22}$$

and it is involved in the *wall shear stress*

$$\tau_w(x) = \left[\frac{\rho^n K U_\infty^{3n}}{x^n}\right]^{\frac{1}{n+1}} |\gamma|^{n-1}\, \gamma \tag{2.23}$$

for $U_\infty \neq 0$ and

$$\tau_w(x) = \left[\frac{\rho^n K U_w^{3n}}{x^n}\right]^{\frac{1}{n+1}} |\gamma|^{n-1}\, \gamma \tag{2.24}$$

for $U_\infty = 0$.

The boundary value problem (2.10), (2.11) is defined on a semi-infinite interval. For Newtonian fluids ($n = 1$), equation (2.10) is equal to the well-known Blasius equation:

$$f''' + \frac{1}{2} f f'' = 0. \tag{2.25}$$

For non-Newtonian fluids on steady surfaces ($\lambda = 0$), the boundary value problem (2.10), (2.11) was investigated in [16]. A non-iterative Töpfer-like transformation was introduced for the determination of γ, when

$$f(\eta) = \gamma^{(2n-1)/3} g\left(\gamma^{(2-n)/3}\eta\right) \tag{2.26}$$

and g is the solution of the initial value problem

$$\left(|g''|^{n-1}\, g''\right)' + \frac{1}{n+1} g g'' = 0, \tag{2.27}$$

$$g(0) = 0, \quad g'(0) = 0, \quad g''(0) = 1. \tag{2.28}$$

By analogy with the Blasius description of Newtonian fluid flows [1], here the goal is to study the similarity solutions and investigate the model arising in the study of a two-dimensional laminar fluid flow with power-law viscosity. A Töpfer-like transformation is applied for the determination of γ.

3. Previous results

The existence and uniqueness of Blasius' boundary layer solution to (2.25), (2.11) with $\lambda = 0$ was rigorously proved by Weyl [18]. The properties of similarity solutions to the boundary layer problem on a moving surface ($\lambda \neq 0$) for Newtonian fluids, have been examined by Hussaini and Lakin [19], Hussaini et al. [20]. It turned out that for a semi-infinite plate, the existence of solutions depends on the ratio of the plate surface velocity U_w to the free stream velocity U_∞. When $n = 1$, $\lambda \leq 0$, the existence, uniqueness and analyticity of solution to (2.10), (2.11) were proved by Callegari and Friedman [21] using the Crocco variable formulation. If $\lambda > 0$, Hussaini and Lakin [19] proved that there is a critical value λ_c such that a solution exists to (2.25), (2.11) only if

$$\lambda \leq \lambda_c \tag{3.1}$$

(see [19]). Dual solutions exist for

$$0 < \lambda < \lambda_c. \tag{3.2}$$

The numerical value of λ_c was found to be 0.3541... for $n = 1$. The non-uniqueness and analyticity of the solution for

$$\lambda \leq \lambda_c \tag{3.3}$$

has been proved by Hussaini et al. [19], [20]. For non-Newtonian fluids ($n \neq 1$) with $\lambda = 0$, the existence, uniqueness and some analytical results for problem (2.10), (2.11) were established when $0 < n < 1$ by Nachman and Callegari [22]. The existence and uniqueness result for $n > 1$ was considered by Benlahsen et al. [17] via Crocco variable transformation. For non-Newtonian fluids the numerical calculations also show that there is a critical value λ_c for each n such that solution exists only if

$$\lambda \leq \lambda_c \tag{3.4}$$

(see [23]). The variations of $f''(0)$ and λ_c with λ for different values of n are given in [24].

In this paper an iterative transformation method is introduced for the determination of γ involved in the drag coefficient and the calculation of the boundary layer thickness for different values n and λ.

4. Numerical solutions

For the determination of the solution to boundary value problems (2.10), (2.11) and (2.10), (2.18) two different methods are applied. The problems are solved on truncated intervals instead of on $[0, \infty)$.

4.1. **Iterative transformation method for the case $U_\infty \neq 0$.** This section is devoted to the application of the scaling concept to numerical analysis of (2.10), (2.11). Solving this problem, proper boundary conditions are not available at infinity.

In the case of $\lambda = 0$ a non-iterative transformation method called Töpfer or Töpfer-like method is be used for solving (2.10), (2.11) either for $n = 1$ [7] or for $n \neq 1$ [24]. The figure of the velocity gradient parameter near the wall $f''(0)$ is exhibited in Figure 1 depending on n [24].

Here an iterative transformation method is described. Non-iterative and iterative transformation methods for boundary value problems were introduced by Fazio [25]. The idea behind the present method is to consider the "partial" invariance of (2.10), (2.11) with respect to a scaling transformation in the sense that the differential equation and one of the boundary conditions at 0 are invariant, while the other two boundary conditions are not invariant. Therefore, the problem modified by introducing a numerical parameter h. Now, equation (2.10) is to be solved with boundary conditions

$$f'(0) = -\lambda h, \tag{4.1}$$

$$f(0) = 0, \quad f'(\infty) = \lim_{\eta \to \infty} f'(\eta) = 1, \tag{4.2}$$

where h is involved, to ensure the invariance of the extended scaling group.

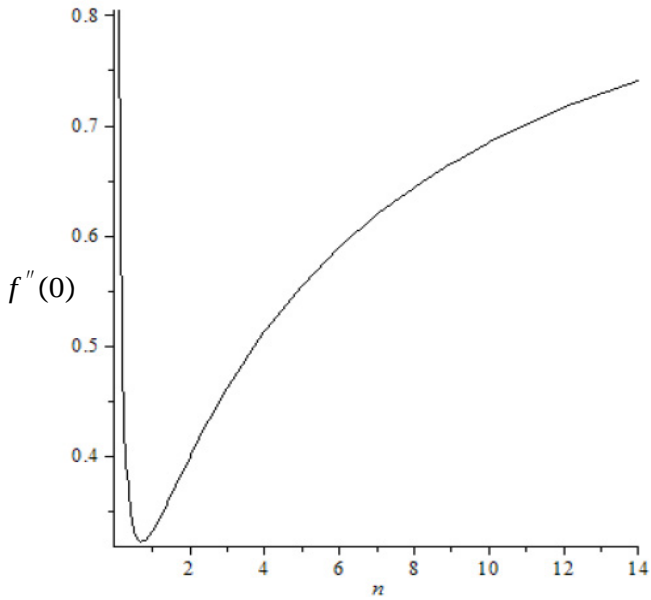

Figure 1. Velocity gradient parameter near the wall $f''(0) = \gamma$ against n for $\lambda = 0$

A Töpfer-like transformation is introduced by

$$g = \sigma^{\kappa} f, \tag{4.3}$$

$$\eta^* = \sigma^{\mu}\, \eta \tag{4.4}$$

to convert the boundary value problem to an initial value problem. Equation (5) is scaling invariant if

$$(2 - n)\kappa = (1 - 2n)\mu. \tag{4.5}$$

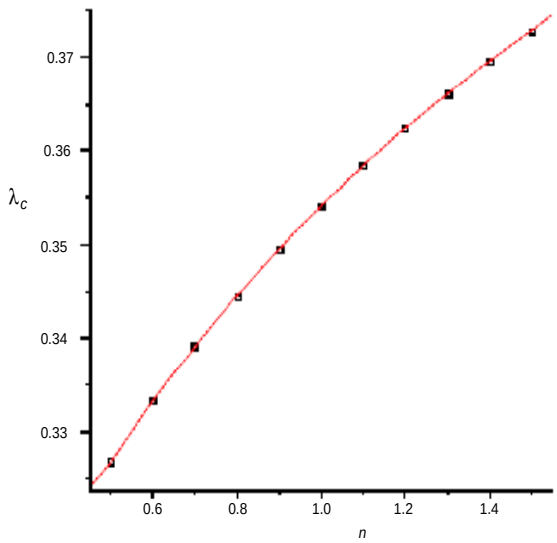

Figure 2. Critical velocity ratio λ_c against n

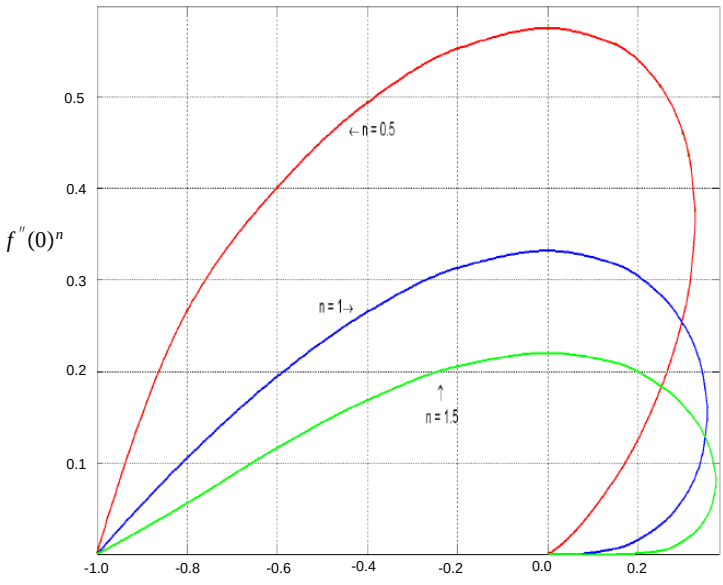

Figure 3. Drag coefficient parameter $f''(0)^n$ against λ for different values of n

Then, one gets

$$\left(|g''|^{n-1}\, g''\right)' + \frac{1}{n+1} g g'' = 0. \tag{4.6}$$

Let us choose $\sigma = \gamma$, then

$$g''(0) = \gamma^{\kappa - 2\mu + 1} \tag{4.7}$$

and with $\kappa - 2\mu + 1 = 0$ one can obtain the appropriate boundary conditions as $\kappa = (1-2n)/3$, $\mu = (2-n)/3$:

$$g(0) = 0, \quad g'(0) = -\lambda h^*, \quad g''(0) = 1, \tag{4.8}$$

where

$$h^* = \gamma^{-\frac{n+1}{3}} h. \tag{4.9}$$

The initial value problem (4.6), (4.8) is solved with the so-called iterative transformation method. A numerical parameter h is applied so that the asymptotic boundary condition remains invariant. By starting with a suitable value of h^*, a root finder algorithm is used to define a sequence h_i^* for $j = 0, 1, ...$ The group parameter σ is obtained by solving numerically the initial value problem after the iterations. The sequence is defined by

$$\Gamma\left(h^*\right) = h - 1 = 0. \tag{4.10}$$

An adequate termination criteria must be used to verify whether

$$\Gamma\left(h_i^*\right) \to 0 \tag{4.11}$$

as $i \to \infty$. The solution of the original problem can be received by rescaling to $h = 1$.

It is important to note that similarity solution exists only for $-1 \leq \lambda \leq \lambda_c$. If $\lambda > \lambda_c$, then the flow separates, the boundary layer structure collapses and the boundary layer approximations are no longer applicable.

Figure 2 provides an upper bound for the critical velocity parameter for non-Newtonian fluids.

The influences of λ and n on the skin friction parameter γ are represented in Figure 3. It can be noticed that there are two solutions for $0 < \lambda < \lambda_c$ (see Figure 3).

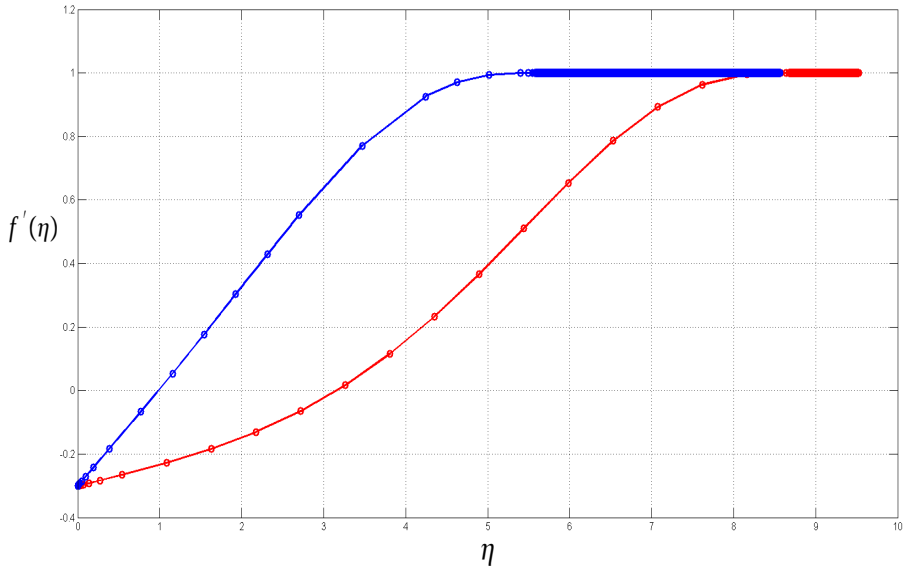

Figure 4. Velocity distribution for $n = 1.5$ and $\lambda = 0.3$

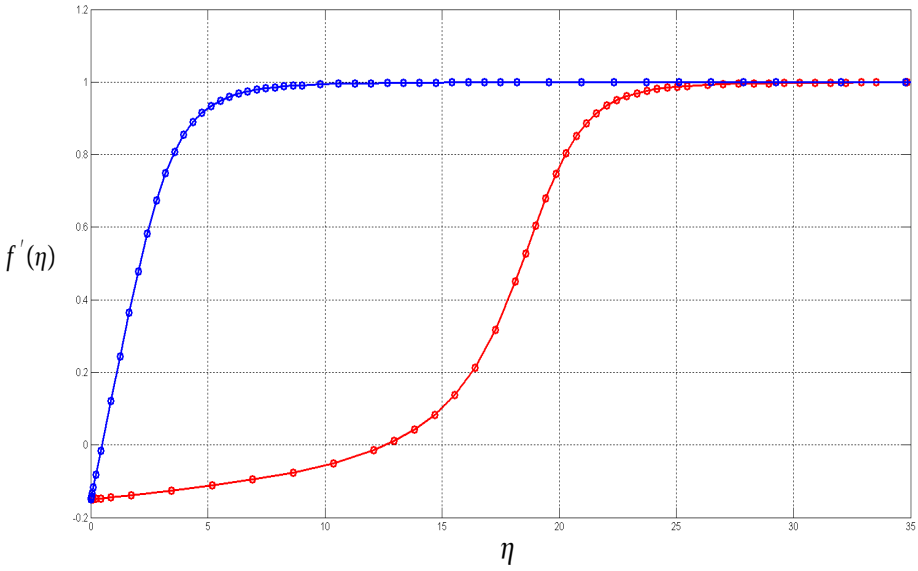

Figure 5. Velocity distribution for $n = 0.5$ and $\lambda = 0.15$

Figures 4-5 show the influence of the positive parameter λ for different power-law exponent n on γ^n. It can be seen that f' monotonically increases from $-\lambda$ to 1 for both the lower and upper solutions. These results are in good agreement with those reported in [23]. Figures 4-6 exhibit the upper and lower solutions for velocities $f' = u(x,y)/U_\infty$ as a function of η for some values of n and λ to show the effect of the velocity parameter λ and power-law exponent n. The figures show that f' monotonically increases from $-\lambda$ to 1 for both the lower and upper solutions. This phenomenon shows that the velocity component u is monotonically increasing in the boundary layer.

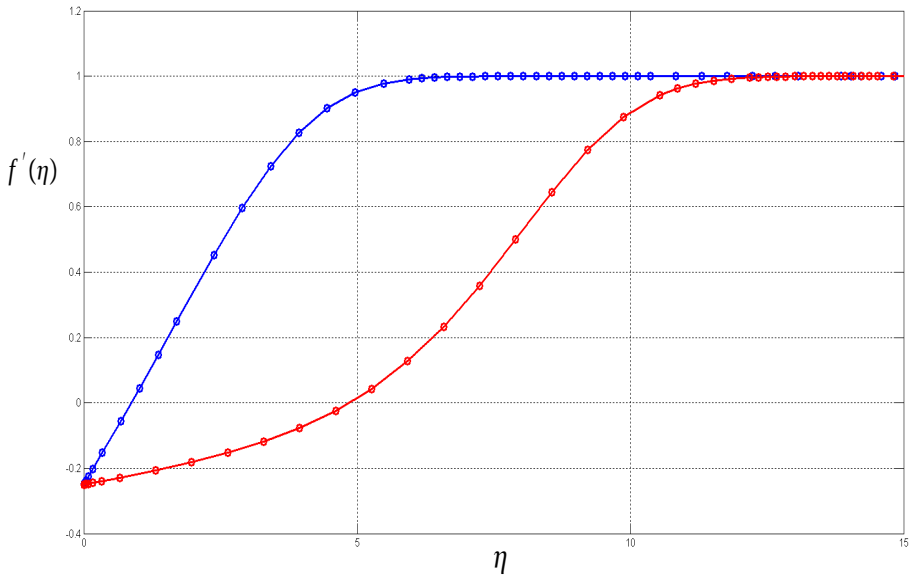

Figure 6. Velocity distribution for $n = 1$ and $\lambda = 0.25$

4.2. **Spectral method for the case $U_\infty = 0$.** In this section a different method is introduced for the numerical solution to (2.10), (2.18) as the iterative transformation method applied in Section 4.1 is not suitable for this case.

With the advent of the spectral element method, complicated domains can be handled. In spite of being mainly used in fluid mechanics, nowadays, this method is more and more frequently utilized in biomechanics, astrophysics and in the study of electromagnetic waves.

We use a spectral method for the determination of the solution to (2.10), (2.18). Spectral methods are able to provide very accurate results when the solution is smooth enough. More precisely, if the solution is differentiable to all orders, an exponential (or infinite order or spectral) convergence is achieved.

All three versions of spectral methods (collocation, Galerkin and tau) belong to the method of weighted residuals and the main classification is carried out according to the type of trial functions used. Trial functions in the Galerkin method are the same as the weight functions and satisfy some of the boundary conditions. In spectral collocation, the trial functions are Dirac-delta functions located at the collocation points while the tau method, similarly to the Galerkin method, operates in the weak form but the trial functions generally do not satisfy the boundary conditions. In our calculations, the collocation method is used. During collocation we determine the function values of the interpolating polynomial at the collocation points (nodal approximation), as opposed to the other two methods, which give results for the coefficients of the truncated approximating series (modal approximation). The n-th order Chebyshev polynomial of the first kind, $T_n(x)$ is defined on [-1; 1] and can be expressed by the recursion

$$T_0(x) = 1,\, T_1(x) = x,$$
$$T_n(x) = 2xT_{n-1}(x) - T_{n-2}(x), \quad n > 1.$$

The modal approximation of function $u(x)$ is calculated by $T_n(x)$. The nodal approximation of $u(x)$ can be evaluated in the Lagrange base. The spectral differentiation for Chebyshev polynomials can be carried out either by a matrix-vector product or by using the Fast Fourier Transform (FFT). We implement the matrix-vector multiplication method because of the relatively low number of collocation points. One of the methods for solving a boundary value problem on an infinite or semi-infinite interval is the so-called domain truncation. Performing the truncation and the linear mapping we have

$$\eta \in [0,\infty) \to \xi \in [0,L] \to \zeta \in [0,1] \to \bar{x} \in [-1,1]\,.$$

Introducing

$$\bar{f}(\bar{x}) = f\left(\eta\left(\bar{x}\right)\right), \tag{4.12}$$

the boundary value problem (2.10), (2.18) is written as

$$\frac{8}{L^3}\bar{f}''' - \frac{1}{n\left(n+1\right)}\left(\frac{4}{L^2}\right)\bar{f}\left|\bar{f}''\right|^{2-n} = 0,$$

$$\bar{f}\left(-1\right) = 0, \quad \bar{f}'\left(-1\right) = L/2, \quad \bar{f}\left(1\right) = 0.$$

After the discretization, $N+2$ number of algebraic equations are at our disposal. The differential equation approximated at the $N-1$ inner nodes and the three boundary conditions. However, the number of unknowns is only $N+1$, therefore the resulting system is overdetermined. One possible solution is to take an interpolant that already satisfies some of the boundary conditions. Let us seek function k such that

$$\bar{f}\left(\bar{x}\right) = P\left(\bar{x}\right)k\left(\bar{x}\right), \quad P\left(\bar{x}\right) = a\bar{x}^2 + b\bar{x} + c. \tag{4.13}$$

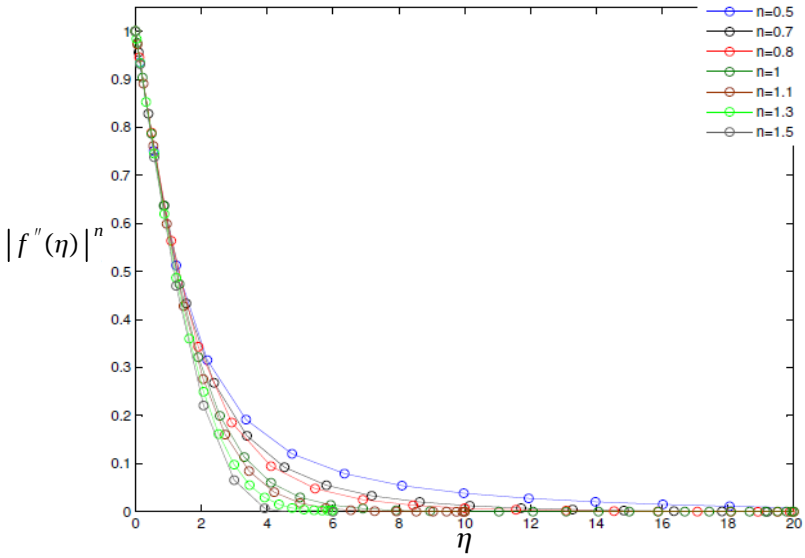

Figure 7. The values of $|f''(0)|^n$ for $n = 0.5...1.5$

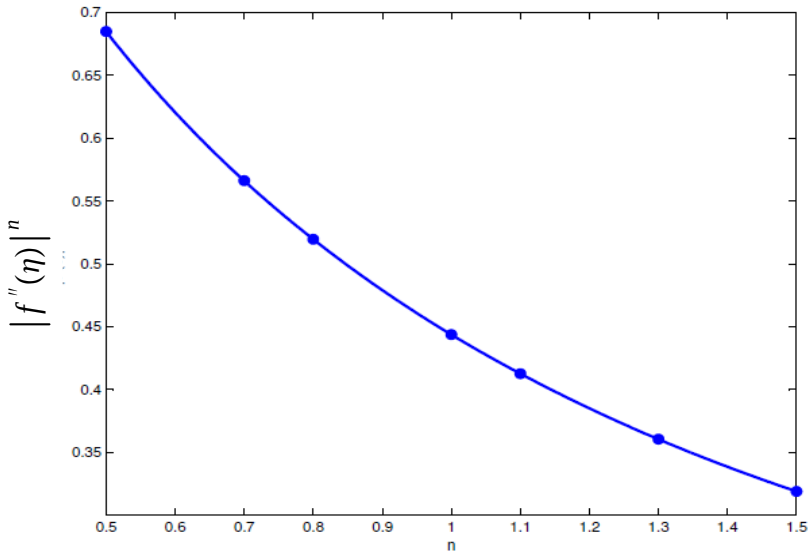

Figure 8. Velocity distribution for different values of n for $U_\infty = 0$

If conditions

$$P(-1) = 0, \quad P'(-1) = L/2 \tag{4.14}$$

and $P'(1) = 0$ are satisfied, then a, b, c can be obtained as follows

$$a = L/8, \quad b = L/4, \quad c = 3L/8. \tag{4.15}$$

Now the differential equation is reformulated for k under boundary conditions

$$k(-1) = 1, \quad k'(1) = 0. \tag{4.16}$$

The boundary value problem is solved with the Chebyshev spectral technique. After the discretization of $k(\bar{x})$ and its derivatives, the resulting system of nonlinear equations is solved with the Levenberg-Marquardt algorithm in Matlab. The numerical results for different power-law exponents are shown in Figure 7, where f' is shown, which is proportional to $u(x, y)$. The figure shows that with larger values of n the boundary layer thickness decreases and shorter interval is enough for the truncation. Because $f''(0) < 0$, both the drag coefficient and the wall shear stress are influenced by $|f''(0)|^n$ and this is exhibited in Figure 8.

5. Conclusions

In this paper the determination of the drag coefficient is shown for two-dimensional, incompressible, laminar non-Newtonian fluid flow along a moving surface. The power-law non-Newtonian approximation is used. The governing partial differential equations are transformed into a third order ordinary differential equation together with the boundary conditions applying the similarity technique. Two main cases are considered: if the velocity U_∞ of the ambient fluid flow is zero or non-zero. For $U_\infty \neq 0$, an iterative transformation method is used for the determination of the numerical results. If $U_\infty = 0$, a spectral method is applied for the simulations. The values of $f''(0) = \gamma$ and the influence on it of the power-law exponent n and the velocity ratio λ on it are exhibited in Figures 1-8.

Acknowledgement. The research work presented in this paper is based on the results achieved within the TÁMOP-4.2.1.B- 10/2/KONV-2010-0001 project and carried out as part of the TÁMOP-4.1.1.C-12/1/KONV-2012-0002 "Cooperation between higher education, research institutes and automotive industry project" in the framework of the New Széchenyi Plan. The realization of this project is supported by the Hungarian Government, by the European Union, and co-financed by the European Social Fund.

References

1. Blasius, H.: Grenzschichten in Flussigkeiten mit kleiner reibung. *Z. Math. Phys.,* **56**, (1908), 1–37.
2. Schowalter, W. R.: The application of boundary layer theory to power-law pseudoplastic fluids: Similar solutions. *AIChE J.,* **6**, (1960), 24–28.
3. Acrivos, A., Shah M. J. and Peterson, E. E.: Momentum and heat transfer in laminar boundary flow of non-Newtonian fluids past external surfaces. *AIChE J.,* **6**, (1960), 312–317.
4. Sakiadis, B. C.: Boundary layers on continuous solid surfaces, *AIChE. J.,* **7**, (1961), 26–28, see also pp. 221–225 and 467–472.
5. Tsou, F., Sparrow, E. and Goldstein R.: Flow and heat transfer in the boundary layer on a continuous moving surface. *Int. J. Heat Mass Transfer,* **10**, (1967), 219–235.

6. Magyari, E. and Keller B.: Heat and mass transfer in the boundary layers on an exponentially stretching continuous surface. *J. Phys. D: Appl. Phys.,* **32**, (1999), 577–585.
7. Magyari, E. and Keller B.: Exact solutions for self-similar boundary-layer flows induced by permeable stretching walls. *Eur. J. Mech. B/Fluids,* **19**, (2000), 109–122.
8. Liao S. J. and Pop, I.: Explicit analytic solution for similarity boundary layer equations. *Int. J. Heat Mass Transfer,* **47**, (2004), 75–85.
9. Nazar R., Amin, N. and Pop, I.: Unsteady boundary layer flow due to a stretching surface in a rotating fluid, *Mech. Res. Comm.,* **31**, (2004), 121–128.
10. Shah Alam Md., Rashedul Islam Md., Ali M., Alim Md. A. and Alam Md. M.: Magnetohydrodynamic boundary layer flow of non-Newtonian fluid and combined heat and mass transfer about an inclined stretching sheet. *Open J. App. Sci.*, **5**, (2015), 279-294.
11. Wei D. M. and Al-Ashhab, S.: Similarity solutions for non-Newtonian power-law fluid flow. *Appl. Math. Mech.*, **35**, (2014), 1155–1166.
12. Grosan, T., Merkin, J. H. and Pop, I.: Mixed convection boundary-layer flow on a horizontal flat surface with a convective boundary condition. *Meccanica*, **48**, (2013), 2149–2158.
13. Su X., Zheng, L. and Jiang, F.: Approximate analytical solutions and approximate value of skin friction coefficient for boundary layer of power law fluids, *Appl. Math. Mech.*, **29**, (2008), 1215-1220.
14. Rama, B. and Goyal, M.: MHD non-Newtonian nano fluid flow over a permeable stretching sheet with heat generation and velocity slip. *Int. J. Math. Comput. Nat. Phys. Eng.*, **8**, (2014), 910-916.
15. Na Noghrehabadi A., Pourrajab R. and Ghalambaz M.: Effect of partial slip boundary condition on the flow and heat transfer of nano fluids past stretching sheet prescribed constant wall temperature. *Int. J. Term. Sci.*, **54**, (2012), 253-261. http://dx.doi.org/10.1016/j.ijthermalsci.2011.11.017
16. Bognár, G.: Similarity solutions of boundary layer flow for non-Newtonian fluids. *Int. J. Nonlinear Sci. Numer. Simul.* **10**, (2010), 1555–1566.
17. Benlahsen, M., Guedda, M. and Kersner, R.: The generalized Blasius equation revisited. *Math. Comput. Model*, **47**, (2008), 1063–1076.
18. Weyl H.: On the differential equations of the simplest boundary-layer problems. *Ann. of Math.,* **43**, (1942), 381-407.
19. Hussaini M. Y. and Lakin W. D.: Existence and nonuniqueness of similarity solutions of a boundary-layer problem, *Q. J. Mech. Appl. Math.*, **39**, (1986), 177–191.
20. Hussaini M. Y., Lakin W. D. and Nachman, A.: On similarity solutions of a boundary layer problem with an upstream moving wall, *SIAMJ. Appl. Math.*, **47**, (1987), 699–709.
21. Callegari, A. J. and Friedman, M. B.: An analytical solution of a nonlinear, singular boundary value problem in the theory of viscous flows. *J. Math. Anal. Appl.*, **21**, (1968), 510–529.
22. Nachman, A. and Callegari A. J.: A nonlinear singular boundary value problem in the theory of pseudoplastic fluids. *SIAM J. Appl. Math.*, **38**, (1980), 275–281.

23. Ishak, A. and Bachok, N.: Power-law fluid flow on a moving wall, *European J. Scie. Res.,* **34** (2009), 55-60.

24. Bognár, G.: On similarity solutions of boundary layer problems with upstream moving wall in non-Newtonian power-law fluids. *IMA J. Appl. Math.*, **77(4)**, (2012), 546-562.

25. Fazio, R.: A novel approach to the numerical solution of boundary value problems on infinite intervals. *SIAM J. Numer. Anal.*, **33**, (1996), 1473–1483.

Journal of Computational and Applied Mechanics, Vol. 11., No. 2., (2016), pp. 123–136
DOI: 10.32973/jcam.2016.009

NUMERICAL MODELING OF A DIRECT SPRING OPERATED PRESSURE RELIEF VALVE

István Erdődi
Budapest University of Technology and Economics
1111 Műegyetem rkp. 3., Budapest, Hungary
ierdodi@hds.bme.hu

Csaba Hős
Budapest University of Technology and Economics
1111 Műegyetem rkp. 3., Budapest, Hungary
cshos@hds.bme.hu

[Received: March 25, 2016, Accepted: July 22, 2016]

Abstract. This paper presents two methods for modeling the response of a direct spring operated pressure relief valve: one approach uses one-dimensional gas dynamical equations coupled with the equation of motion of a one degree-of-freedom oscillator, while the other employs deforming mesh CFD simulations to fully resolve the flow field. We found that if the force and flow rate characteristics of the valve are implemented into the reduced order model, it yields approximately the same results as the CFD computations.

Mathematical Subject Classification: 76N15, 76-04
Keywords: CFD, linear stability, nonlinear vibrations, pressure relief valve

1. Introduction

Pressure relief valves (PRVs) are used as the last line of defense against overpressure in industrial environments. There are two main parameters of these valves regarding their operation: the *set pressure* (p_{set}), which is the minimum pressure at which the valve opens, and the *capacity*, that is by definition the flow rate through the valve at full lift and at 110% of the set pressure. The latter describes how fast the overpressure can be reduced to the desired level and maintaining full capacity is critical from a safety point of view. It is possible that under certain circumstances instabilities arise, which reduce the capacity, endangering the whole system. The goal of this paper is to investigate the behavior of a direct spring operated PRV in gas service with a focus on stability. This configuration consists of a disc pressed against the seat at the pipe end by a pre-compressed spring. The advantage of this simple design is that the set pressure can be easily adjusted through the pre-compression of the spring, and the probability of mechanical failure can be kept at a minimal level due to the low number of moving parts. In order to avoid exceeding the time available for blowdown, adding any kind of artificial damping is forbidden by the current industrial standards [1].

Based on this, the valve disc can be modeled as a one degree-of-freedom oscillator, which — due to the force acting on it— is described by a non-linear differential equation. This means that dynamic instabilities must be taken into account. The RP520 standard of the American Petroleum Institute distinguishes three different kinds of instabilities for direct spring operated PRVs. The first is the so-called *cycling*, during which the set pressure slowly builds up after the valve closes, resulting in small frequency ($< 1\,\mathrm{Hz}$) vibrations. Contrary to this, both *flutter* and *chatter* are large frequency ($> 10\,\mathrm{Hz}$) self-excited vibrations — the difference between them is that during chatter the amplitude is so large that the disc usually impinges on the seat and upper stopper, resulting in not only a decrease in capacity but mechanical damage as well. Cycling is well-understood and means to avoid it are already included in the standards. However, the reasons behind flutter and chatter are not completely clear according to API, but it is mentioned that these are due to the acoustic coupling of the valve disc and the pipe end. Ongoing research activities aim to gain a better understanding of these phenomena [2, 3]. The goals of this paper are (a) to provide a steady-state CFD model for the evaluation of the force acting on the valve disc and the capacity, (b) to study the transient valve response by a deforming mesh CFD model and (c) to compare the results of unsteady CFD runs against a simplified ODE (ordinary differential equation) model including quasi-steady fluid force characteristics.

2. Theoretical Background

The system under analysis consists of a straight pipe section and the valve itself. The governing equations describing the behavior of these components are derived in this section.

2.1. **The valve.** As stated before, the valve disc can be modeled as an oscillator:

$$m\ddot{x} + k\dot{x} + s(x + x_0) = F_{\mathrm{total}}, \tag{2.1}$$

where m is the reduced mass of the system, x is the valve lift, k is the damping coefficient, s is the spring stiffness, x_0 is the pre-compression of the spring and F_{total} is the total force acting on the valve. The force can be traced back to three physical phenomena: force acts because of the pressure difference between the upstream and downstream pressures, due to the change in the momentum of the out-flowing gas, and originates from viscous effects, i.e.

$$F_{\mathrm{total}} = F_{\mathrm{pres}} + F_{\mathrm{mom}} + F_{\mathrm{visc}}, \tag{2.2}$$

where the force from the pressure distribution is

$$F_{\mathrm{pres}} = A_{\mathrm{pipe}}(p_{\mathrm{v}} - p_{\mathrm{b}}), \tag{2.3}$$

where A_{pipe} is the cross-sectional area of the pipe, p_{v} is the pressure upstream of the valve and p_{b} is the back pressure. The problem is that F_{mom} and F_{visc} cannot be calculated analytically, as neither the velocity nor the direction of the flow are known. Their effects can be taken into account through the effective area, which supposes that

the total force can be evaluated as a multiplication of the static pressure difference and an area function [2], that is

$$F_{\text{total}}(x, p_v) = A_{\text{eff}}(x)(p_{\text{v}} - p_{\text{b}}), \tag{2.4}$$

where A_{eff} is the effective area function. As there is no flow when the valve is seated, i.e. $x = 0$, the effective area for that position equals the cross-sectional area of the pipe, resulting in

$$A_{\text{eff}}(0) = A_{\text{pipe}}. \tag{2.5}$$

Substituting the effective area into Equation (2.1) gives

$$m\ddot{x} + k\dot{x} + s(x + x_0) = A_{\text{eff}}(x)(p_{\text{v}} - p_{\text{b}}). \tag{2.6}$$

It can be seen that this equation is indeed a non-linear ordinary differential equation. One of the goals of the stationary mesh CFD simulations presented later is to obtain the $A_{\text{eff}}(x)$ function for the given PRV.

2.2. **Stability of the linearized system.** The first step in the linear stability analysis is finding the equilibria x_{eq} from equation (2.6), taking into account that $\dot{x}_{\text{eq}} \equiv 0$ and $\ddot{x}_{\text{eq}} \equiv 0$, i.e.

$$x_{\text{eq}} = \frac{A_{\text{eff}}(x_{\text{eq}})}{s}(p_{\text{v,eq}} - p_{\text{b}}) - x_0. \tag{2.7}$$

Linearizing the effective area around this point results in

$$A_{\text{eff}}(x) \approx A_{\text{eff}}(x_{\text{eq}}) + \left.\frac{\mathrm{d}A_{\text{eff}}(x)}{\mathrm{d}x}\right|_{x=x_{\text{eq}}} (x - x_{\text{eq}}), \tag{2.8}$$

which can be substituted back into Equation (2.6) to get

$$m\ddot{x}+k\dot{x}+s[(x-x_{\text{eq}})+x_{\text{eq}}+x_0] \approx \left(A_{\text{eff}}(x_{\text{eq}}) + \left.\frac{\mathrm{d}A_{\text{eff}}(x)}{\mathrm{d}x}\right|_{x=x_{\text{eq}}} (x - x_{\text{eq}})\right)(p_{\text{v}}-p_{\text{b}}). \tag{2.9}$$

Utilizing that x_{eq} is an equilibrium solution and introducing $\zeta = x - x_{\text{eq}}$ gives

$$m\ddot{\zeta} + k\dot{\zeta} + \left(s - \left.\frac{\mathrm{d}A_{\text{eff}}}{\mathrm{d}x}\right|_{x=x_{\text{eq}}} (p_{\text{v}} - p_{\text{b}})\right)\zeta = 0. \tag{2.10}$$

This differential equation is linear, and the role of the effective area is highlighted: the linearised force decreases the coefficient of the displacement, i.e. the spring stiffness. The term in the brackets can be regarded as an "effective spring stiffness", and loss of stability occurs when it becomes negative, i.e.

$$s - \left.\frac{\mathrm{d}A_{\text{eff}}}{\mathrm{d}x}\right|_{x=x_{\text{eq}}} (p_{\text{v}} - p_{\text{b}}) < 0. \tag{2.11}$$

Therefore, the stability of an equilibrium solution for a given pressure difference and spring stiffness can be determined from the derivative of the effective area at the equilibrium displacement, meaning that knowing the $A_{\text{eff}}(x)$ function is crucial from the point of stability as well.

2.3. **Mass flow rate through the valve.** As stated before, the mass flow rate through the valve is one of the most important parameters. Two cases must be distinguished based on the ratio of the pressure at the pipe end and the back pressure. The flow is said to be choked if this ratio is above the critical pressure ratio [4], which for air ($\gamma = 1.4$) is

$$\left(\frac{p_\mathrm{v}}{p_\mathrm{b}}\right)_{\mathrm{critical}} = \left(\frac{\gamma+1}{2}\right)^{\frac{\gamma}{\gamma-1}} = 1.8929, \tag{2.12}$$

and the formula for the mass flow rate [4] is

$$\dot{m}_\mathrm{out} = C_\mathrm{D} A_\mathrm{ref} \sqrt{\gamma \rho_\mathrm{v} p_\mathrm{v} \left(\frac{2}{\gamma-1}\right)^{\frac{\gamma+1}{\gamma-1}}}, \tag{2.13}$$

where ρ_v is the density upstream of the valve and the reference area equals

$$A_\mathrm{ref} = D_\mathrm{pipe} \pi x. \tag{2.14}$$

The most problematic part of Equation (2.13) is the discharge coefficient C_D — the other main goal of the stationary mesh CFD simulations is to investigate its values at various valve lifts and pipe end pressures. Similarly, the equation for the mass flow rate for compressible non-choked flows [5] is

$$\dot{m}_\mathrm{out} = C_\mathrm{D} A_\mathrm{ref} \sqrt{2\rho_\mathrm{v} p_\mathrm{v} \left(\frac{\gamma}{\gamma-1}\right) \left[\left(\frac{p_\mathrm{b}}{p_\mathrm{v}}\right)^{\frac{2}{\gamma}} - \left(\frac{p_\mathrm{b}}{p_\mathrm{v}}\right)^{\frac{\gamma+1}{\gamma}}\right]}. \tag{2.15}$$

2.4. **Interaction between the valve and the seat.** There is also the possibility of the valve disc hitting the end of the pipe, which phenomenon is not covered by the equations listed above. This event can have two outcomes: either the disc bounces back with a set loss of kinetic energy or it sticks to the pipe end. As these are not covered by the deforming mesh simulations, their modelling can be omitted if the sole goal of the 1D model is to produce a comparable output to the CFD results.

2.5. **The pipe.** The flow in the pipe can be regarded as a one-dimensional, unsteady, subsonic, compressible gas flow with wall friction, which is described by the following system of partial differential equations [6]. The continuity is

$$\frac{\partial \rho}{\partial t} + \frac{\partial \rho v}{\partial \xi} = 0, \tag{2.16}$$

the 1D equation of motion with pipe friction looks like

$$\frac{\partial \rho v}{\partial t} + \frac{\partial \left(\rho v^2 + p\right)}{\partial \xi} = \frac{\lambda(v)\rho}{2D_\mathrm{pipe}} v|v|, \tag{2.17}$$

and the adiabatic energy equation is

$$\frac{\partial \rho e}{\partial t} + \frac{\partial \left(\rho v e + p v\right)}{\partial \xi} = 0, \tag{2.18}$$

where p is the pressure, v is the velocity, e is the specific energy, t is the time, ξ is the spatial coordinate along the pipe, λ is the Darcy friction factor and D_pipe is the

diameter of the pipe. The friction factor was defined as a function of the velocity using Blasius' approximation for turbulent flows [7], which is

$$\lambda(v) = 0.316\,(Re(v))^{-0.25} = 0.316\left(\frac{vD_{\text{pipe}}}{\nu}\right)^{-0.25} \tag{2.19}$$

2.6. **Numerical solution of the system.** All of these equations were implemented in the 1D model. Equation (2.6) was solved using a 4th/5th order Runge-Kutte solver, while the Lax-Wendroff method [8] was applied to Equations (2.16) to (2.18). A constant total pressure reservoir boundary condition was defined for one end of the pipe, while the other was coupled with the valve. The compressible method of characteristics was used for the numerical implementation of both [6].

3. Steady-state CFD Simulations

The goal of the steady-state CFD simulations is to investigate the flow properties at various *fixed* lifts and reservoir pressures. With these information it will also be possible to obtain the $A_{\text{eff}}(x)$ and C_{D} values required for the 1D model. However, it must be noted that this method of approach assumes that even though these parameters refer to dynamic processes, they can be approximated from steady-state solutions. All the CFD simulations were done using ANSYS-CFX.

Both [9] and [10] investigate the general flow parameters of valves, while [11] uses an approach similar to this work, as it also approximates the dynamic properties from results of fixed lift solutions. An advanced version of this method can be seen in [12]: the authors generated individual meshes for a large number of lifts, and their solver chooses from them based on the calculated displacement values. Its advantage is that the process more or less retains its dynamic nature; however, the valve lifts can only be discrete values and the resolution depends on the number of prepared meshes.

The axisymmetry of both the geometry and the boundary conditions were taken into account, therefore only a wedge shaped domain was generated with a central angle of 5°. This also means that all of the results had to be rescaled for the full 360° geometry. The dimensions of the modeled valve correspond to the measuring equipment located in the laboratory of the Department of Hydrodynamic Systems in order to ease the comparison of the calculated and the measured results in the future. This includes a pipe with an inner diameter of 40.2 mm (corresponding to $1\,1/2''$ nominal) and a valve disc diameter of 55.7 mm. The length of the pipe was set to $10D_{\text{pipe}}$.

3.1. **Simulation settings.** Due to the axisymmetry, a wedge shaped domain with one cell in the radial direction was sufficient for the modeling of the problem. The block structured mesh was created using ICEM and consists of $90,787$ nodes. The domain, the boundary conditions and the element numbers are illustrated in Figure 1. The thinner lines denote the edges of the blocks. A mesh dependency study was also carried out, which is presented at the end of this section.

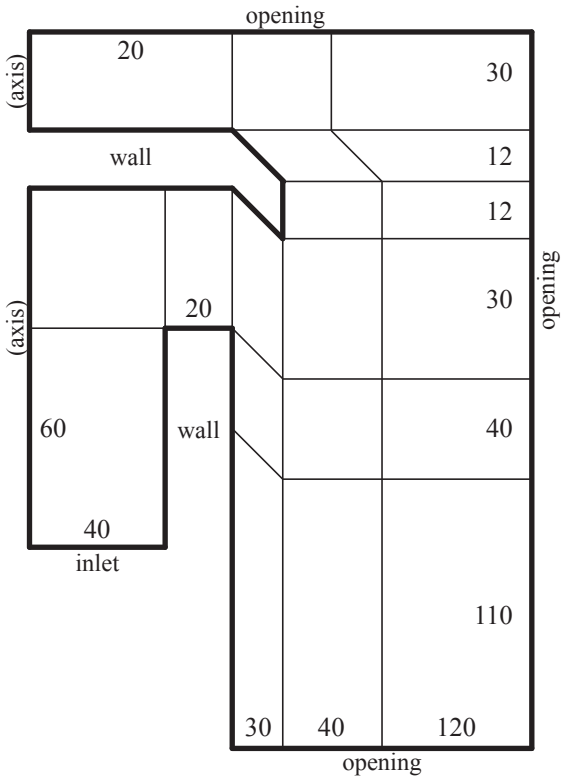

Figure 1. The domain, the boundary conditions and the element numbers (not a proportional illustration)

The opening pressure was set to 1 bar (absolute), while the temperatures at both the inlet and the opening were 293 K. The inlet total pressure was varied between 1–6 bar and the valve lift range of 0.01–$0.35 D_{\text{pipe}}$ was resolved. To ease the notation, relative values for the lift will be used from now on with

$$\bar{x} = x/D_{\text{pipe}}. \tag{3.1}$$

As the steady-state solver only produced converging residuals at very low pressure ratios, a transient solver was used in most cases. These simulations were stopped after both the force acting on the valve and the inlet mass flow rate had converged. The medium was set to air with the ideal gas assumption. High Resolution and Second Order Backward Euler schemes were used for the advection and the time stepping, respectively. The k-ε model was chosen for turbulence, because its scalable wall function supposedly provides reasonable accuracy for the boundary layer even without its full numerical resolution [13]. A turbulence model dependency study was also concluded, which is presented at the end of this section. The time step is variable and is automatically adjusted by the solver to maintain a set number of inner loop iterations (between 5 and 9) .

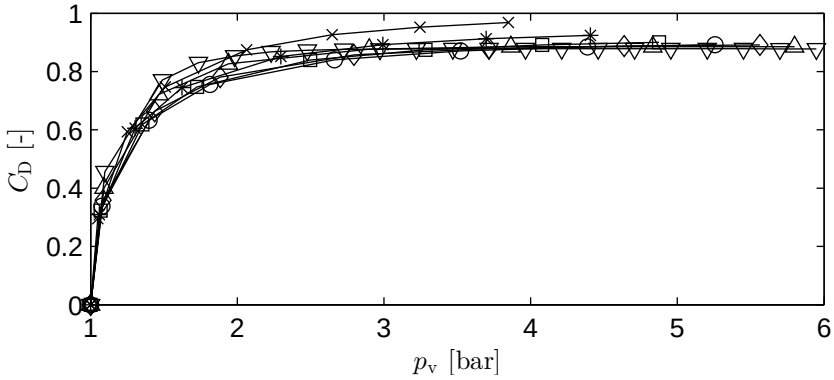

Figure 2. The discharge coefficients at various lifts (▽: $\bar{x} = 0.05$, △: $\bar{x} = 0.10$, ◇: $\bar{x} = 0.15$, ○: $\bar{x} = 0.20$, □: $\bar{x} = 0.25$, ∗: $\bar{x} = 0.30$, ×: $\bar{x} = 0.35$)

3.2. **Results for the discharge coefficient.** The discharge coefficients are obtained from Equation (2.13) by substituting the mass flow rates from the CFD simulations ($\dot{m}_{\text{out}} = \dot{m}_{\text{out,CFD}}$), resulting in

$$C_D = \frac{\dot{m}_{\text{out,CFD}}}{A_{\text{ref}} \sqrt{\gamma \rho_v p_{v,\text{CFD}} \left(\frac{2}{\gamma-1}\right)^{\frac{\gamma+1}{\gamma-1}}}}. \tag{3.2}$$

The pipe end pressures were also taken from the CFD simulations, while the densities were calculated from the inlet temperature, as experience showed that the variations in density along the pipe are negligible. The discharge coefficients can be seen in Figure 2. Note that the above formula for the mass flow rate is only valid for choked flows, i.e. when the pressure ratio at the valve is above critical, therefore it is not expected to be constant in the non-choked range. After averaging the results in the choked range, a value of $C_D = 0.8778$ was obtained for the discharge coefficient.

3.3. **Results for the effective area.** Equation (2.4) gives the effective areas by substituting the total force acting on the valve and the static pressure from the results of the CFD simulations, that is

$$A_{\text{eff}} = \frac{F_{\text{total,CFD}}}{p_{v,\text{CFD}} - p_b}. \tag{3.3}$$

The back pressure (p_b) is known from the boundary condition, therefore the effective area can be obtained. The ratio of the effective area and the cross-sectional area of the pipe is shown in Figure 3. It confirms that it is reasonable to assume that the effective area depends only on the lift, as it does not significantly vary with the pressure. The $A_{\text{eff}}(x)$ function can be calculated by averaging the values corresponding to the same lifts, which can be seen in Figure 4. It also includes the piecewise cubic interpolation of the function.

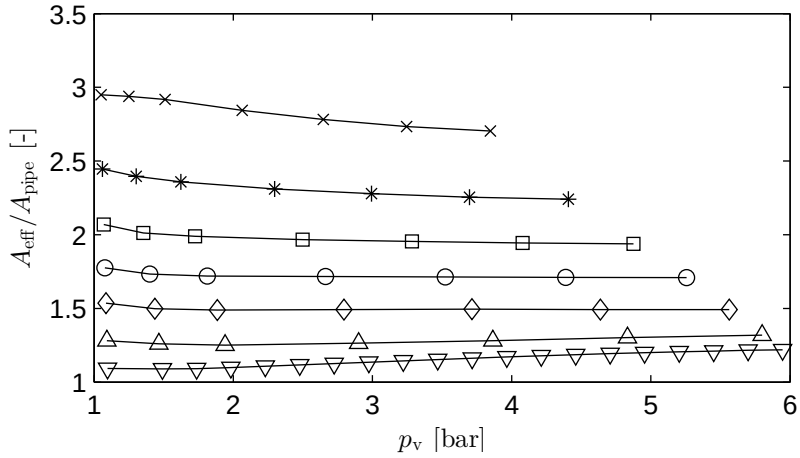

Figure 3. The ratio of the effective area and the cross-sectional area of the pipe at various lifts ($\triangledown$: $\bar{x} = 0.05$, $\triangle$: $\bar{x} = 0.10$, $\diamond$: $\bar{x} = 0.15$, $\ominus$: $\bar{x} = 0.20$, $\boxminus$: $\bar{x} = 0.25$, $*$: $\bar{x} = 0.30$, $\times$: $\bar{x} = 0.35$)

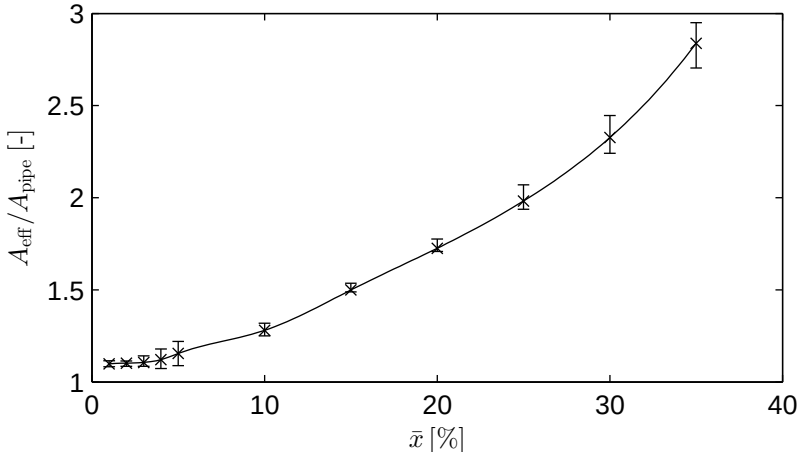

Figure 4. The mean effective area versus the lift ($\times$: CFD results, –: piecewise cubic interpolation) with the maximum and minimum values (errorbars)

3.4. **Equilibrium and stability.** First, the equilibrium points must be calculated from Equation (2.7). The pre-compression can be expressed from the set pressure by substituting $x_{\text{eq}} = 0$ and utilizing that $A_{\text{eff}}(0) = A_{\text{pipe}}$:

$$x_0 = \frac{A_{\text{pipe}}(p_{\text{set}} - p_{\text{b}})}{s} \tag{3.4}$$

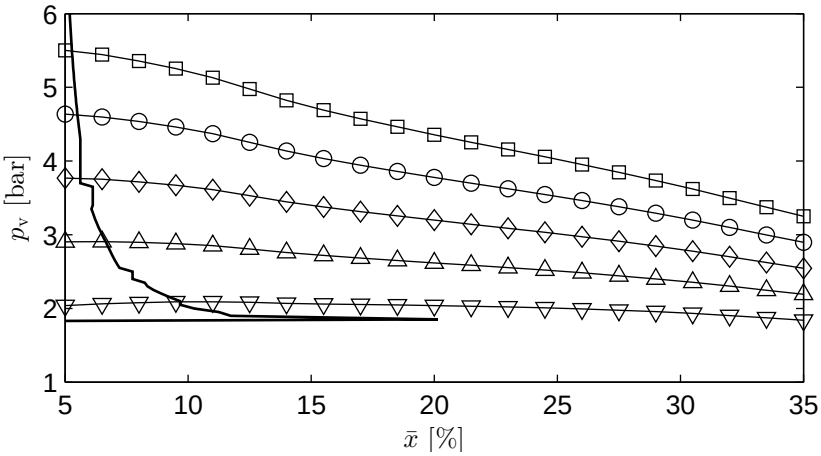

Figure 5. The equilibrium curves (▽: $p_{\text{set}} = 2$ bar, △: $p_{\text{set}} = 3$ bar, ◇: $p_{\text{set}} = 4$ bar, ○: $p_{\text{set}} = 5$ bar, □: $p_{\text{set}} = 6$ bar) and the b.o.s. (–)

The characteristic curves, i.e. the $p_{\text{v,eq}}(x_{\text{eq}})$ functions corresponding to various set pressures can be formulated using Equations (2.7) and (3.4). The stability of the points on the $p_{\text{v}}{-}x$ plane was obtained from Equation (2.11). The equilibrium curves for different set pressures and the boundary of stability (b.o.s.) are shown in Figure 5. The equilibria to the left of the b.o.s. are stable. All of these calculations were made with a spring stiffness of $s = 12\,500\,\text{N/m}$.

3.5. **Mesh and turbulence model dependency study.** To reduce computational time, both the mesh and the turbulence model dependency studies were only concluded at around the corner points of the investigated inlet total pressure and valve lift domain, i.e. at $p_{\text{t,min}} = 1.5\,\text{bar}$ and $p_{\text{t,max}} = 6.0\,\text{bar}$, and at $x_{\text{min}} = 0.05D_{\text{pipe}}$ and $x_{\text{max}} = 0.35D_{\text{pipe}}$. For the mesh dependency study a mesh was generated with two times as many elements on all edges. The relative differences in both the forces acting on the valve and the inlet mass flow rates were under 0.5%, indicating that the domain had been sufficiently resolved by the original mesh. The effect of turbulence modelling was investigated by repeating the simulations in the aforementioned corner points with both the baseline k-ω and the k-ω SST models, and their results were compared to those from the original simulations, where k-ε had been used. The largest relative differences were 3.67% for the force and 5.40% for the mass flow rate, both of which are sufficiently small.

4. Deforming Mesh CFD Simulations

During the calculations of the previous section a method of determining the equilibria and their stability for a direct spring operated pressure relief valve was shown, but it involved the major assumption that the total force acting on the valve can be accurately approximated from steady-state fixed valve results. To investigate the

effect of unsteadiness, another CFD model was assembled in which the valve disc is free to move in the direction of the pipe axis. The spring is taken into account through the *Rigid Body* option of CFX with its built-in *spring* feature. Its stiffness and the reduced mass of the moving bodies had to be defined. As the simulated domain has a centre angle of 5° (instead of the full 360°), both of them had to be rescaled appropriately, i.e. multiplied by 5°/360°. The unloaded position of the spring must also be set, which can be calculated from the pre-compression and the initial position. The movement of the valve disc results in a change in the fluid domain, which is handled by allowing the deformation of the mesh. The *Mesh Stiffness* was set in a way that the larger the cell volume, the less it deforms in order to preserve the mesh quality at the critical regions (at the walls, in the free jet) as much as possible. The chosen value for the stiffness was

$$s_{\text{mesh}} = \frac{1}{V_{\text{cell}}} \left[\frac{\text{m}^2}{\text{s}}\right]. \tag{4.1}$$

Even though this setting permits large displacements from the initial position of the valve, experience showed that the mesh still suffers a significant loss of quality, to the point that sometimes negative cell volumes would occur. To prevent this, the ICEM CFD replay script based remeshing feature was used, which is covered in detail in [14], only its basics will be summarized here. First of all, a condition for the remeshing has to be defined through an *Interrupt Condition* — when this expression becomes *true*, the solver stops. In these simulations it happens when the area average of the *Total Mesh Displacement* at the valve reaches 1 mm. It proved to be a good quantity to monitor, as its value resets to zero after every remeshing. The remeshing itself is set in a *Configuration*, which is triggered by the *Interrupt Condition*. Its *ICEM CFD Replay* option requires the geometry file (*.tin) of the initial position, a replay script for the meshing (*.rpl), the mapping of the moving part between ICEM and CFX, and a monitor for the total displacement. The area average of the *Total Centroid Displacement* at the valve was used for the latter (it is not reset during the remeshing). The unit conversion between ICEM and CFX (i.e. from millimeters to meters in our case) is handled by the *ICEM CFD Geometry Scale*, which was set to 0.001. A remeshing step goes as follows:

1. The *Interrupt Condition* is fulfilled.
2. The solver stops and ICEM is called.
3. The geometry file is loaded into ICEM and is shifted with the value of the corresponding monitor.
4. The meshing replay script is run on the modified geometry.
5. A new simulation — with the new mesh — is initialized with the results of the stopped one.

This way the required mesh quality can be maintained even for extremely large deformations, as long as no change occurs in the topology. An example for the latter would be the seating of the valve, which is not covered by this model. A similar approach, albeit without remeshing, can be found in [15], but in their case the reservoir was also implemented in the CFD model.

5. Comparison of Valve Responses

To check whether the steady-state assumption of the effective area was correct, 1D simulations based on the model described in the first section were compared to the results of the deforming mesh CFD method. The spring stiffness was set to 12 500 N/m, and its pre-compression was defined such that the valve was in an equilibrium position at the start. The discharge coefficient was also set according to the steady-state simulations ($C_{\mathrm{D}} = 0.8778$), while the damping was neglected ($k = 0$). Two cases were simulated with the same inlet total pressure jump but with different jump durations. The valve responses and the pressure profiles are illustrated in Figure 6. The correspondence is satisfactory, as the displacement from the 1D model closely follows that of the deforming mesh solution, even though some difference can be observed in the new equilibria, and also the response seems to be significantly delayed in the case of the slower pressure jump.

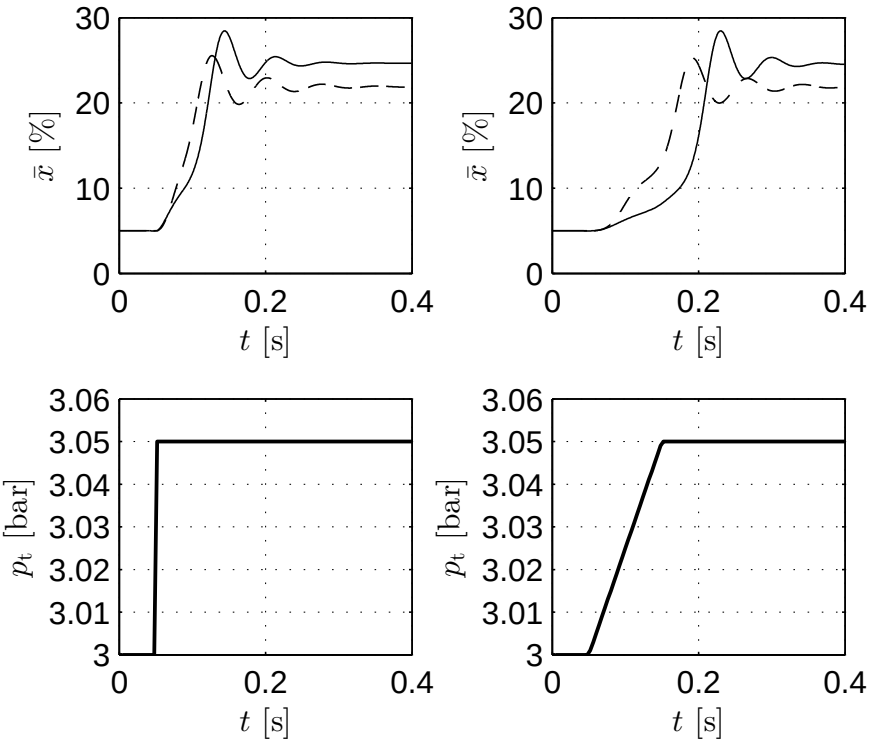

Figure 6. Valve responses of the deforming mesh CFD (cont. line) and the 1D (dashed line) models in the case of a sudden (left) and slow (right) pressure jumps

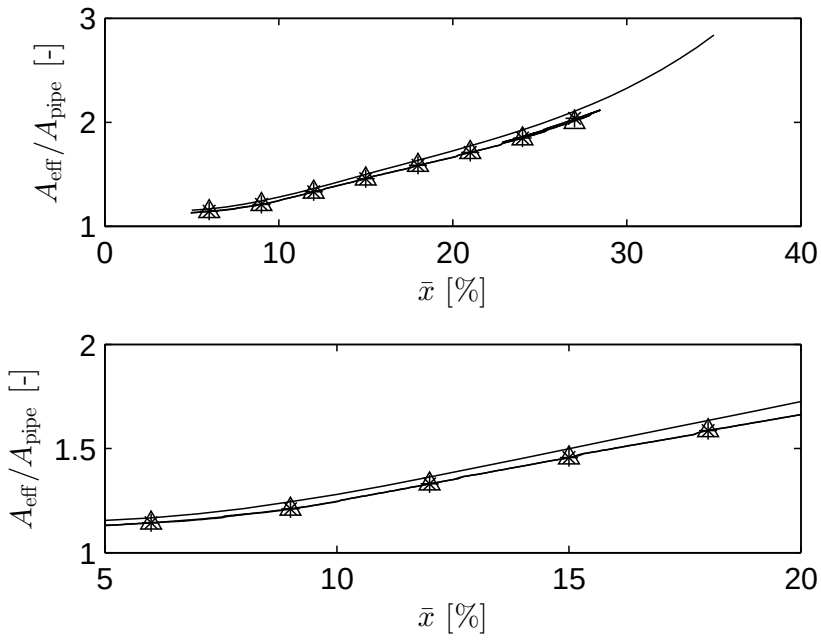

Figure 7. Comparison of the effective areas (–: interpolated steady-state, △: sudden pressure jump, ∗: slow pressure jump)

As the most important modeled parameter is the effective area, it is beneficial to compare the piecewise cubic interpolation of its steady-state result to those from the two deforming mesh simulations. The various effective areas can be seen in Figure 7. The difference between the two deforming mesh cases is negligible, indicating that the rate of change in the pressure had no effect on the effective area in this parameter range. Since the steady-state curve also runs close to the other curves, it is strongly implied that the basic assumption, i.e. the independence of the effective area from the pipe end pressure was correct for the case of exponentially decaying solutions. The steady-state forces are also somewhat higher, which explains the higher equilibrium lifts of the 1D model in Figure 6.

Flutter usually occurs in configurations where long upstream piping is present [2]. Indeed, unstable behaviour was observed at $p_{\text{set}} = 3\,\text{bar}$, $L_{\text{pipe}} = 38 D_{\text{pipe}}$ and $p_{\text{t}}(t) \equiv 3.2\,\text{bar}$. The valve responses can be seen in Figure 8. While the vibration frequencies are similar, there is a significant difference in the amplitudes. Whether this is due to the absence of some damping effect in the one-dimensional model or the overdamping of pressure waves in the CFD code (which is common for solvers based on the finite volume method) requires further studies and is beyond the scope of this paper.

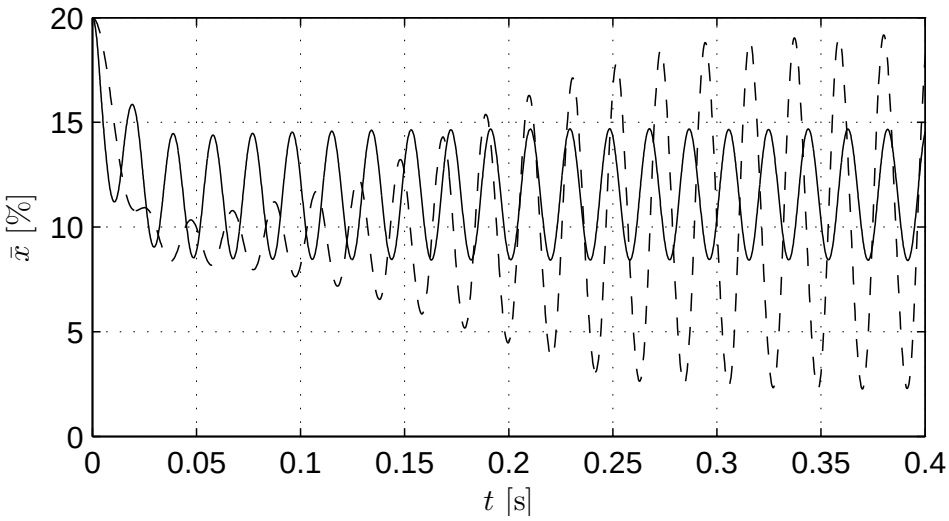

Figure 8. Flutter resolved by the deforming mesh CFD (cont. line) and the 1D (dashed line) models.

6. Conclusions

The stationary mesh simulations proved to be computationally cost-effective in mapping a large segment of the $p_t - \bar{x}$ plane both in terms of the effective area and the discharge coefficient. These also made possible the linear stability analysis of various equilibrium solutions. The piecewise cubic interpolation of the effective area and the averaged value of the discharge coefficient were also useful for the 1D model. The deforming mesh CFD results confirmed that the approximation of the effective area from steady-state flow fields is indeed accurate enough to be used for the modeling of pressure jump scenarios, and that it is also able to qualitatively — and to some extent, quantitatively — produce the same dynamically unstable valve responses as well. Therefore, the 1D model turned out to be an effective and fast tool for transient calculations, albeit strongly depending on the aforementioned input parameters. This behavior also gives flexibility, i.e. it can be easily modified to simulate the response of other PRVs if these parameters are known from CFD simulations or measurements.

Acknowledgement. This research has been supported by the Hungarian Scientific Research Fund OTKA, under grant no. K 116549.

References

1. API: *Sizing, Selection, and Installation of Pressure-Relieving Devices in Refineries*. API RP520 Part II, Sixth Edition, American Petroleum Institute, Washington, USA, 2013.
2. Hős, C., Champneys, A., Paul, K., and McNeely, M.: Dynamic behavior of direct spring loaded pressure relief valves in gas service: Model development, measurements and instability mechanisms. *J. Loss. Prevent. Proc.*, **31**, (2014), 70–81.

3. Bazsó, C. and Hős, C.: An experimental study on the stability of a direct spring loaded poppet relief valve. *J. Fluid. Struct.*, **42**, (2013), 456–465.
4. Zucker, R. D. and Biblarz, O.: *Fundamentals of Gas Dynamics*. John Wiley & Sons, 2nd edn., 2002.
5. Oosthuizen, P. H. and Carscallen, W. E.: *Introduction to Compressible Fluid Flow*. Taylor & Francis Group, 2nd edn., 2013.
6. Zucrow, M. J. and Hoffman, J. D.: *Gas Dynamics*, vol. 1. John Wiley & Sons, 1976.
7. Blasius, H.: Das Aehnlichkeitsgesetz bei Reibungsvorgängen in Flüssigkeiten. *Mitteilungen über Forschungsarbeiten auf dem Gebiete des Ingenieurwesens*, **131**, (1912), 639–643.
8. Lax, P. and Wendroff, B.: Systems of conservation laws. *Commun. Pur. Aappl. Math.*, **13**, (1960), 217–237.
9. Dossena, V., Marinoni, F., Bassi, F., Franchina, N., and Savini, M.: Numerical and experimental investigation on the performance of safety valves operating with different gases. *Int. J. Pres. Ves. Pip.*, **104**, (2013), 21–29.
10. Dempster, W. and Elmayyah, W.: Two phase discharge flow prediction in safety valves. *Int. J. Pres. Ves. Pip.*, **110**, (2013), 61–65.
11. Song, X.-G., Park, Y.-C., and Park, J.-H.: Blowdown prediction of a conventional pressure relief valve with a simplified dynamic model. *Math. Comput. Model.*, **57**, (2013), 279–288.
12. Beune, A., Kuerten, J., and van Heumen, M.: CFD analysis with fluid–structure interaction of opening high-pressure safety valves. *Comput. Fluids.*, **64**, (2012), 108–116.
13. ANSYS: ANSYS CFX-Solver Theory Guide. Release 14.5, 2012.
14. ANSYS: ANSYS CFX Reference Guide. Release 14.5, 2012.
15. Song, X., Cui, L., Cao, M., Cao, W., Park, Y., and Dempster, W. M.: A CFD analysis of the dynamics of a direct-operated safety relief valve mounted on a pressure vessel. *Energ. Convers. Manage.*, **81**, (2014), 407–419.

Journal of Computational and Applied Mechanics, Vol. 11., No. 2., (2016), pp. 137–157
DOI: 10.32973/jcam.2016.010

ENTRANCE REGION FLOW IN CONCENTRIC ANNULI WITH ROTATING INNER WALL FOR BINGHAM FLUID

Srinivasa Rao Nadiminti[1] and A. Kandasamy[2]
Department of Mathematical and Computational Sciences
National Institute of Technology Karnataka, Surathkal, Mangalore - 575025, India
[1]srinudm@gmail.com [2]kandy@nitk.ac.in

[Received: February 25, 2016, Accepted: July 28, 2016]

Abstract. Entrance region flow in concentric annuli with rotating inner wall for Bingham non-Newtonian fluid has been studied numerically. The inner cylinder is assumed to be rotating with a constant angular velocity ω and the outer cylinder to be stationary. Finite difference analysis is used to obtain the velocity components *U, V, W* and the distribution of pressure *P* along the radial direction *R*. With Prandtl's boundary layer assumptions, the continuity and momentum equations are solved iteratively using a finite difference method. Computational results are obtained for various non-Newtonian flow parameters and geometrical considerations. The development of the axial velocity profile, radial velocity profile, tangential velocity profile and pressure distribution in the entrance region have been analyzed. Comparison of the present results with the results available in literature for various particular cases has been done and found to be in agreement.

Mathematical Subject Classification: 76U05
Keywords: Concentric annuli, Bingham fluid, entrance region flow, finite difference method, rotating wall

Nomenclature

k	consistency index $(Pa.s)$,
m	number of radial increments in the numerical mesh network,
p	pressure (Pa),
p_0	initial pressure (Pa),
P	dimensionless pressure, $(p-p_0)/(\rho u_0^2)$,
r	radial coordinate (m),
z	axial coordinate (m),
θ	tangential coordinate (rad),
$R = r/R_2$	dimensionless coordinate in the radial direction,
$Z = 2z(1-N)/(R_2 Re)$	dimensionless coordinate in the axial direction,
R_1	radius of the inner cylinder (m),
R_2	radius of the outer cylinder (m),
$B = \tau_0 R_2/(k u_0)$	Bingham number,
$Re = 2\rho(R_2 - R_1)u_0/k$	Reynolds number,

T_a	Taylor number
$N = R_1/R_2$	dimensionless aspect ratio of the annulus,
u	velocity components in z direction (m/s),
v	velocity components in r direction (m/s),
w	velocity components in θ direction (m/s),
u_0	uniform inlet velocity (m/s),
$U = u/u_0$	dimensionless velocity component in z direction,
$V = \rho v R_2/\mu_r$	dimensionless velocity component in r direction,
$W = w/(\omega R_1)$	dimensionless velocity component in θ direction,
ρ	density of the fluid (kg/m^3),
μ	apparent viscosity of the model $(Pa.s)$,
τ_0	yield stress (Pa),
ω	regular angular velocity (rad/s),
ΔR	dimensionless mesh size in the radial direction,
ΔZ	dimensionless mesh size in the axial direction.

1. Introduction

The problem of entrance region flow in concentric annuli with rotating inner wall for non-Newtonian fluids is of practical importance in engineering applications such as the design of cooling systems for electric machines, compact rotary heat exchangers and combustion chambers, axial-flow turbo machinery and polymer processing industries. In the nuclear reactor field, laminar flow conditions occur when the coolant flow rates are reduced during periods of low power operation. Many important industrial fluids are non-Newtonian in their flow characteristics and are referred to as rheological fluids. These include blood, various suspensions such as coal–water or coal-oil slurries, glues, inks, foods, polymer solutions, paints and many others. The fluid considered here is the Bingham model, which is of the 'time-independent yield stress' fluid category.

The problem of entrance region flow of non-Newtonian fluids in an annular cylinders has been studied by various authors. Mishra et al. [1] studied the flow of the Bingham plastic fluids in the concentric annulus and obtained results for boundary layer thickness, centre core velocity, pressure distribution. Batra and Bigyani Das [2] developed the stress-strain relation for the Casson fluid in the annular space between two coaxial rotating cylinders where the inner cylinder is at rest and outer cylinder is rotating. Maia and Gasparetto [3] applied a finite difference method for the Power-law fluid in the annuli and found differences in the entrance geometries. Sayed-Ahmed and Hazem [4] applied a finite difference method to study the laminar flow of a Power-Law fluid in the concentric annuli with rotating inner wall. Recently, Kandasamy and Srinivasa Rao [5] investigated entrance region flow in concentric annuli with a rotating inner wall for Herschel-Bulkley Fluids. The constitutive equation for Bingham fluid is given by Bird et al. [6]

$$\tau_{ij} = \left(\mu + \frac{\tau_0}{\varepsilon}\right) \varepsilon_{ij} \qquad (\tau \geq \tau_0) \tag{1.1}$$

where

$$\tau = \sqrt{\frac{1}{2}\tau_{ij}\tau_{ij}} \quad \textit{and} \quad \varepsilon = \sqrt{\frac{1}{2}\varepsilon_{ij}\varepsilon_{ij}}$$

where τ_0 is the yield stress, τ_{ij} and ε_{ij} are the stress tensor and the rate-of-strain tensor, respectively. and μ is the viscosity of the fluid.

Moreover, Kandasamy [7] investigated the entrance region flow heat transfer in concentric annuli for a Bingham fluid and presents the velocity distributions, temperature and pressure in the entrance region. Round and Yu [8] analyzed the developing flows of Herschel-Bulkley fluids through concentric annuli. Flow of Casson fluid in a narrow tube with a side branch was investigated by Misra and Ghosh [9]. Flow of Casson fluid in a pipe filled with a homogeneous porous medium has been considered by Dash et al. [10]. Ahmed and Attia [11] investigated Magneto hydrodynamic flow and heat transfer of a non-Newtonian fluid in an eccentric annulus. An analytical solution for the entrance region blood flow in a concentric annuli was obtained by Batra and Jena [12] assuming blood to obey Casson model.

Further, Manglik and Fang [13] numerically investigated the flow of non-Newtonian fluids through annuli. Nouar et al. [14] reported the results of numerical analysis of the thermal convection for Herschel-Bulkley fluids. Poole and Chhabra [15] reported the results of a systematic numerical investigation of developing laminar pipe flow of yield stress fluids. Entropy generation in Non-Newtonian fluids due to heat and mass transfer in the entrance region of ducts was investigated by Galanis and Rashidi [16]. Rhashidi et al. [17] studied the investigation of heat transfer in a porous annulus with pulsating pressure gradient by the homotopy analysis method. Recently, Rekha and Kandasamy [18] investigated the entrance region flow of Bingham fluid in an annular cylinder.

In the present work, the problem of entrance region flow of Bingham fluid in concentric annuli has been investigated. The analysis has been carried out under the assumption that the inner cylinder is rotating and the outer cylinder is at rest. With Prandtl's boundary layer assumptions, the equation of conservation of mass and momentum are discretized and solved using linearized implicit finite difference technique. The system of linear algebraic equations thus obtained has been solved by the Gauss-Jordan method. The development of axial velocity profile, radial velocity profile, tangential velocity profile and pressure distribution in the entrance region have been determined for different values of non-Newtonian flow characteristics and geometrical parameters. The effects of these on the velocity profiles and pressure distribution are discussed.

2. Formulation of the problem

The geometry of the problem is shown in Figure 1. The Bingham fluid enters the horizontal concentric annuli with inner and outer radii R_1 and R_2, respectively, from a large chamber with a uniform flat velocity profile u_0 along the axial direction z and with an initial pressure p_0. The inner cylinder rotates with an angular velocity ω and the outer cylinder is at rest. The flow is steady, laminar, incompressible, axisymmetric

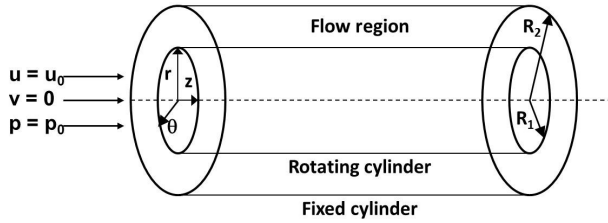

Figure 1. Geometry of the Problem

and of constant physical properties. We consider a cylindrical polar coordinate system with the origin at the inlet section on the central axis of the annulus, the z-axis along the axial direction and the radial direction r perpendicular to the z-axis. Under the above assumptions with the usual Prandtl's boundary layer assumptions [19], the governing equations in a polar coordinate system (r, θ, z) for a Bingham fluid in the entrance region are:

$$\text{Continuity equation}: \frac{\partial(rv)}{\partial r} + \frac{\partial(ru)}{\partial z} = 0 \tag{2.1}$$

$$r - \text{momentum equation}: \frac{w^2}{r} = \frac{1}{\rho}\frac{\partial p}{\partial r} \tag{2.2}$$

$$\theta - \text{momentum equation}: v\frac{\partial w}{\partial r} + u\frac{\partial w}{\partial z} + \frac{vw}{r} = \frac{1}{\rho r^2}\frac{\partial}{\partial r}\left(r^2\left[\tau_0 + kr\frac{\partial}{\partial r}(\frac{w}{r})\right]\right) \tag{2.3}$$

$$z - \text{momentum equation}: v\frac{\partial u}{\partial r} + u\frac{\partial u}{\partial z} = -\frac{1}{\rho}\frac{\partial p}{\partial z} + \frac{1}{\rho r}\frac{\partial}{\partial r}\left(r\left[\tau_0 + k\frac{\partial u}{\partial r}\right]\right) \tag{2.4}$$

where u, v, w are the velocity components in the directions z, r, θ, respectively, ρ is the density of the fluid, k is the consistency index and p is the pressure.

The boundary conditions of the problem are given by

$$\begin{aligned} \text{for } z &\geq 0 \text{ and } r = R_1, \;\; v = u = 0 \text{ and } w = \omega R_1\,, \\ \text{for } z &\geq 0 \text{ and } r = R_2, \;\; v = u = w = 0\,, \\ \text{for } z &= 0 \text{ and } R_1 < r < R_2, \;\; u = u_0\,, \\ \text{at } z &= 0, \;\; p = p_0\,. \end{aligned} \tag{2.5}$$

Using the boundary conditions (2.5), the continuity equation (2.1) can be expressed in the following integral form:

$$2\int_{R_1}^{R_2} ru\,\mathrm{d}r = (R_2^2 - R_1^2)u_0 \tag{2.6}$$

It is worth introducing the following dimensionless variables and parameters:

$$R = \frac{r}{R_2}, \quad U = \frac{u}{u_0}, \quad V = \frac{\rho v R_2}{\mu_r},$$
$$W = \frac{w}{\omega R_1}, \quad N = \frac{R_1}{R_2}, \quad P = \frac{p - p_0}{\rho u_0^2}, \quad Z = \frac{2z(1-N)}{R_2 Re},$$
$$B = \frac{\tau_0 R_2}{k u_0}, \quad Re = \frac{2\rho(R_2 - R_1)u_0}{k}, \quad \mu_r = k\left(\frac{\omega R_1}{R_2}\right), \quad T_a = \frac{2\omega^2\rho^2 R_1^2 (R_2 - R_1)^3}{\mu_r^2 (R_1 + R_2)}.$$

Here B is the Bingham number, Re is the Reynolds number, T_a is the Taylor number, μ_r is known as reference viscosity and N is the aspect ratio of the annulus.

Equations (2.1) to (2.4) and (2.6) in the dimensionless form are given by

$$\frac{\partial V}{\partial R} + \frac{V}{R} + \frac{\partial U}{\partial Z} = 0 \tag{2.7}$$
$$\frac{W^2}{R} = \frac{Re^2(1-N)}{2(1+N)T_a}\frac{\partial P}{\partial R} \tag{2.8}$$
$$V\frac{\partial W}{\partial R} + U\frac{\partial W}{\partial Z} + \frac{VW}{R} = \frac{\partial^2 W}{\partial R^2} + \frac{1}{R}\frac{\partial W}{\partial R} - \frac{W}{R^2} + \frac{2B}{R} \tag{2.9}$$
$$V\frac{\partial U}{\partial R} + U\frac{\partial U}{\partial Z} = -\frac{\partial P}{\partial Z} + \frac{1}{R}.\frac{\partial U}{\partial R} + \frac{\partial^2 U}{\partial R^2} + \frac{B}{R} \tag{2.10}$$

and

$$2\int_N^1 RU \, \mathrm{d}R = (1 - N^2) \tag{2.11}$$

The boundary conditions (2.5) in the dimensionless form are:

$$\begin{aligned} \text{for } Z &\geq 0 \text{ and } R = N, \quad V = U = 0 \text{ and } W = 1\,, \\ \text{for } Z &\geq 0 \text{ and } R = 1, \quad V = U = W = 0\,, \\ \text{for } Z &= 0 \text{ and } N < R < 1, \quad U = 1\,, \\ \text{at } Z &= 0, \quad P = 0\,. \end{aligned} \tag{2.12}$$

3. Numerical Solution

The numerical analysis and the method of solution adopted here can be considered as an indirect extension of the work of Coney and El-Shaarawi [20]. Considering the mesh network of Figure 2, the following difference representations are made. Here ΔR and ΔZ represent the grid size along the radial and axial directions, respectively.

$$V_{i+1,j+1} = V_{i,j+1}\left(\frac{N + i\Delta R}{N + (i+1)\Delta R}\right) - \\ - \frac{\Delta R}{4\Delta Z}\left(\frac{2N + (2i+1)\Delta R}{N + (i+1)\Delta R}\right)(U_{i+1,j+1} + U_{i,j+1} - U_{i+1,j} - U_{i,j}) \tag{3.1}$$

$$\frac{W_{i,j+1}^2}{N + i\Delta R} = \frac{(1-N)Re^2}{2T_a(1+N)}\frac{P_{i,j+1} - P_{i-1,j+1}}{\Delta R} \tag{3.2}$$

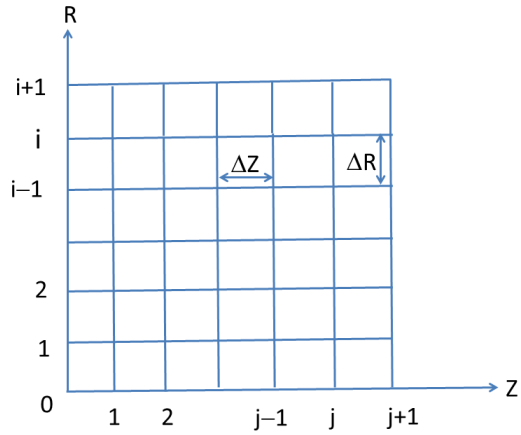

Figure 2. Grid formation for finite difference representations

$$Vi,j\left[\frac{W_{i+1,j+1}+W_{i+1,j}-W_{i-1,j}-W_{i-1,j+1}}{4\Delta R}\right]+Ui,j\left[\frac{W_{i,j+1}-W_{i,j}}{\Delta Z}\right]+\frac{V_{i,j}W_{i,j}}{N+i\Delta R}=$$
$$=\frac{W_{i+1,j+1}+W_{i+1,j}-2W_{i,j+1}-2W_{i,j}+W_{i-1,j}+W_{i-1,j+1}}{2(\Delta R)^2}+$$
$$+\frac{W_{i+1,j+1}+W_{i+1,j}-W_{i-1,j}-W_{i-1,j+1}}{(N+i\Delta R)4\Delta R}-\frac{W_{ij}}{(N+i\Delta R)^2}+\frac{2B}{N+i\Delta R} \quad (3.3)$$

$$Vi,j\left[\frac{U_{i+1,j+1}-U_{i-1,j+1}}{2\Delta R}\right]+Ui,j\left[\frac{U_{i,j+1}-U_{i,j}}{\Delta Z}\right]=$$
$$=-\frac{P_{i,j+1}-P_{i,j}}{\Delta Z}+\frac{U_{i+1,j+1}-U_{i-1,j+1}}{(N+i\Delta R)2\Delta R}+\frac{U_{i+1,j+1}-2U_{i,j+1}+U_{i-1,j+1}}{(\Delta R)^2}+\frac{B}{N+i\Delta R} \quad (3.4)$$

where $i=0$ at $R=N$ and $i=m$ at $R=1$.

The application of the trapezoidal rule to equation (2.11) yields

$$\frac{\Delta R}{2}(NU_{0,j}+U_{m,j})+\Delta R\sum_{i=1}^{m-1}U_{i,j}(N+i\Delta R)=\left(\frac{1-N^2}{2}\right)$$

The boundary condition (2.12) gives $U_{0,j}=U_{m,j}=0$ and then the above equation reduces to

$$\Delta R\sum_{i=1}^{m-1}U_{i,j}(N+i\Delta R)=\left(\frac{1-N^2}{2}\right) \quad (3.5)$$

The set of difference equations (3.1) to (3.5) have been solved by the iterative procedure. Starting at the column $j=0$ (annulus entrance) and applying equation (3.3)

for $1 \leq i \leq m-1$, we get a system of linear algebraic equations. This system has been solved by using the Gauss-Jordan method to obtain the values of the velocity component W in the second column $j = 1$. Then applying equations (3.2) and (3.4) for $1 \leq i \leq m-1$ and equation (3.5), we get a system of linear equations. Again solving this system by Gauss-Jordan method, we obtain the values of the velocity component U and the pressure P in the second column $j = 1$. Finally, the values of the velocity component V in the second column $j = 1$ are obtained from equation (3.1) by Gauss-Jordan method using the known values of U. Repeating this procedure, we can advance, column by column, along the axial direction of the annulus until the flow becomes axially and tangentially fully developed.

4. Results and Discussion

Numerical calculations have been performed for all admissible values of Bingham number B, aspect ratio N and various parameters as shown in Table 1. Here, the velocity profiles and pressure distribution along the radial direction during the rotation of the inner wall of the annuli are shown in Figures 3–26.

Table 1. List of various parameters used

Various values of parameters				
Aspect Ratio N	Radial position R	Axial position Z	Rt	Bingham number B
0.3	0.1	0.02, 0.03	0, 20	0, 10, 20, 30
0.5	0.1	0.02, 0.03	0, 20	0, 10, 20, 30
0.8	0.05	0.02, 0.03	0, 20	0, 10, 20, 30

Figures 3 to 8 show the development of the tangential velocity profile component W for $N = 0.3, 0.5, 0.8$ at axial positions of $Z = 0.02, 0.03$ and for different values of Bingham numbers B. Here, the parameter Rt, which is the ratio of Reynolds number to Taylor number, is fixed as 20. The values of tangential velocity decrease from the inner wall to outer wall of the annulus. Also, it is found that with the increase of aspect ratio N, the tangential velocity profile increases. That is, the tangential velocity is higher when the gap of the annuli is small. Further, it is found that with the increase of Bingham number, the tangential velocity profile increases. This means the tangential velocity tends to increase for thick viscous fluids when the inner cylinder is rotating. From the computed results corresponding to various values of Rt, it is observes that the effect of the parameter Rt is negligible for the tangential velocity.

Figures 9 to 14 show the development of the axial velocity profile component U for $N = 0.3, 0.5, 0.8$ at axial positions of $Z = 0.02, 0.03$ and for different values of the Bingham numbers B. The computation was done for various values of the parameter Rt to study the effect of rotation of inner cylinder. The values corresponding to $Rt = 0$ and 20 are depicted in these figures. It is found that the velocity component

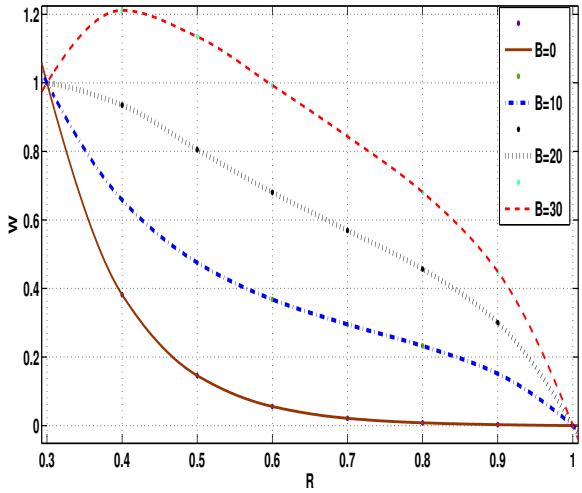

Figure 3. Tangential velocity profile for $N = 0.3$ at $Z = 0.02$

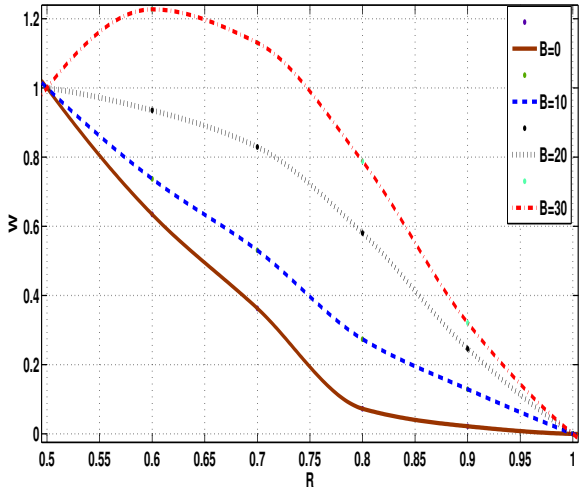

Figure 4. Tangential velocity profile for $N = 0.5$ at $Z = 0.02$

U increases with the increase of Bingham number B as well as aspect ratio N. For both stationary ($Rt = 0$) as well as the rotating inner cylinder ($Rt = 20$), it is observed that the velocity profile takes the parabolic form when Bingham number B reaches zero (Newtonian fluid). However, the rotational effect on the axial velocity

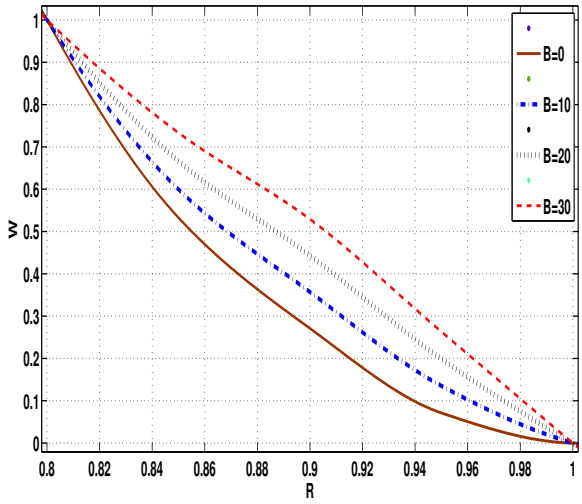

Figure 5. Tangential velocity profile for $N = 0.8$ at $Z = 0.02$

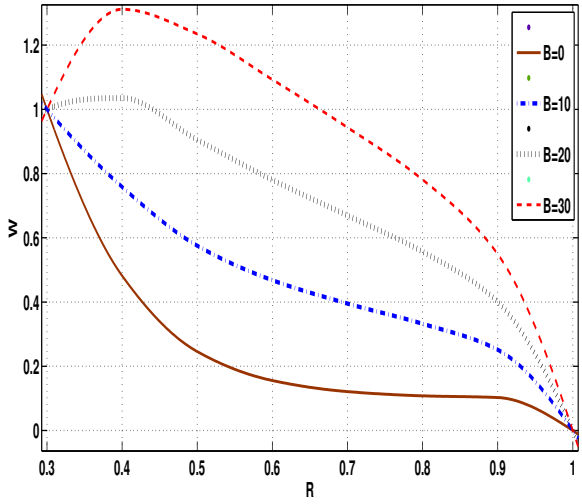

Figure 6. Tangential velocity profile for $N = 0.3$ at $Z = 0.03$

component is very small as per the observed results. Here, our results corresponding to $B = 0$ match with the results of Coney and El-Shaarawi [20] and $Rt = 0$ with various Bingham numbers match with the results of Kandasamy [7].

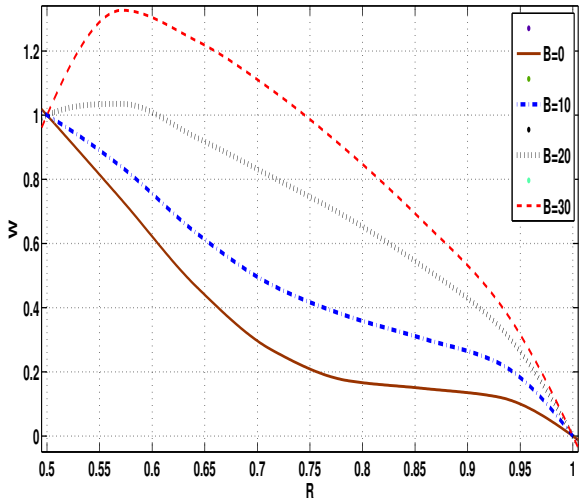

Figure 7. Tangential velocity profile for $N = 0.5$ at $Z = 0.03$

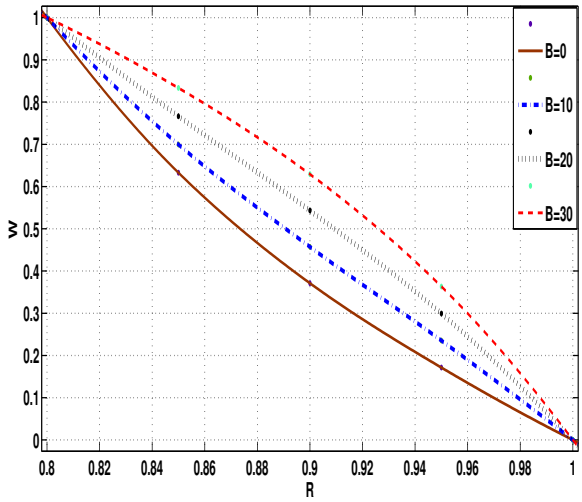

Figure 8. Tangential velocity profile for $N = 0.8$ at $Z = 0.03$

The radial velocity profile component V for $N = 0.3$, 0.5 and 0.8, for different values of Bingham number B at axial positions of $Z = 0.02$, 0.03 are shown in Figures 15 to 20. Again, the values of the parameter Rt are taken as 0 and 20 for computational purposes. The values of radial velocity are negative in the region near the outer wall,

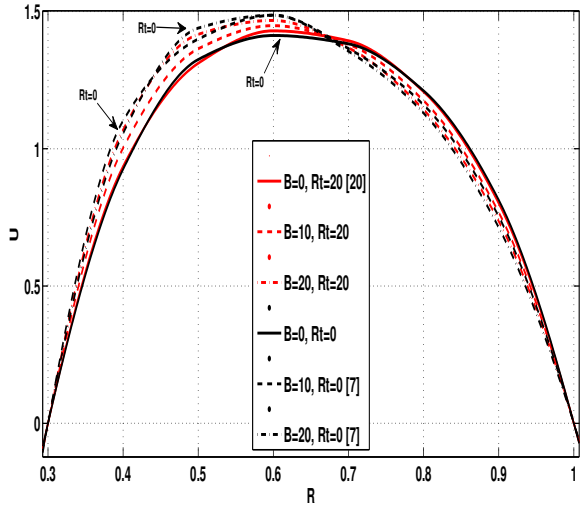

Figure 9. Axial velocity profile for = 0.3 at $Z = 0.02$

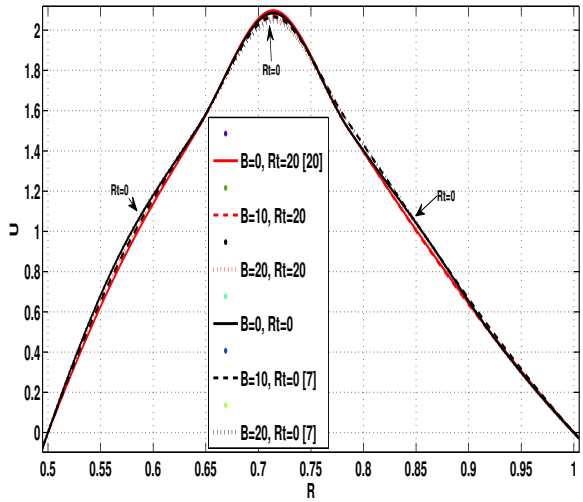

Figure 10. Axial velocity profile for $N = 0.5$ at $Z = 0.02$

since it is in the opposite direction to the radial coordinate R, and it has positive values near the inner wall because it has the same direction of the radial coordinate. The values of the radial velocity decreases with increase of Rt and Bingham number B at any cross section of the axis. The results of particular cases like $Rt = 0$ (without

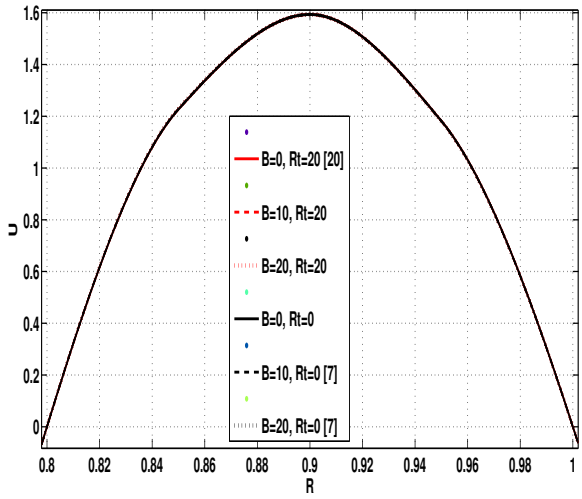

Figure 11. Axial velocity profile for $N = 0.8$ at $Z = 0.02$

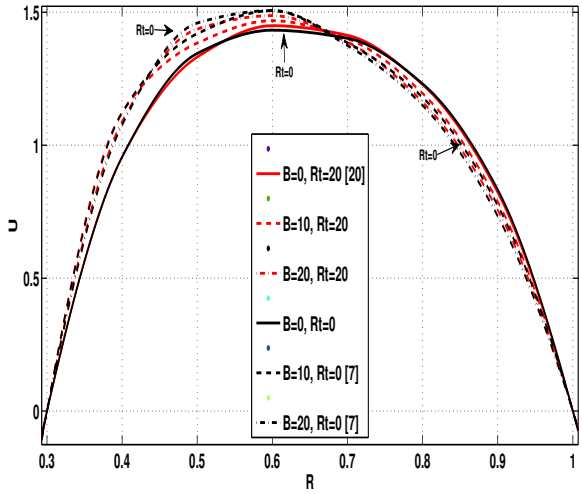

Figure 12. Axial velocity profile for $N = 0.3$ at $Z = 0.03$

rotation) and $B = 0$ (Newtonian fluid) match fully with earlier research work [7, 20], respectively.

Figures 21 to 26 show the distribution of the pressure P along the radial coordinate R for the same chosen values of parameters. It is found that the value of P increases

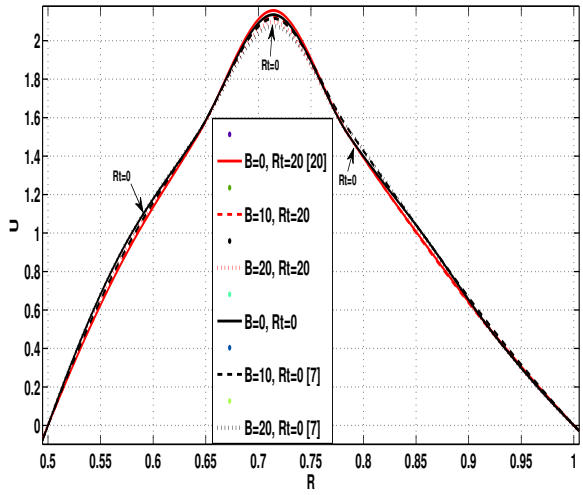

Figure 13. Axial velocity profile for $N = 0.5$ at $Z = 0.03$

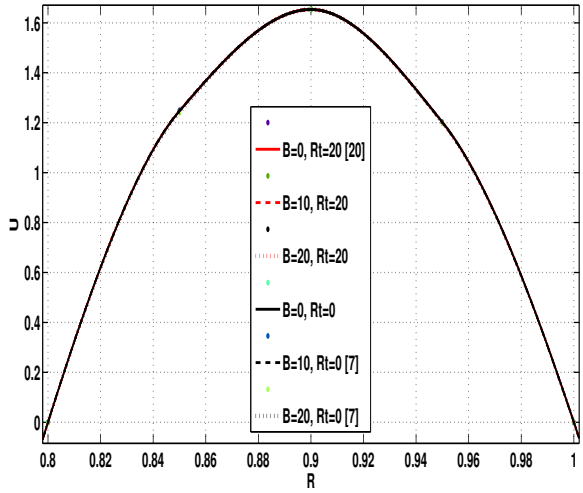

Figure 14. Axial velocity profile for $N = 0.8$ at $Z = 0.03$

from a minimum at the inner wall to a maximum at the outer wall. Further, it is found that with increase of Bingham numbers the pressure values P increase. This is because the pressure will tend to be higher for thick viscous fluids. Moreover, it is observed that the pressure slowly becomes independent of the radial coordinate in the

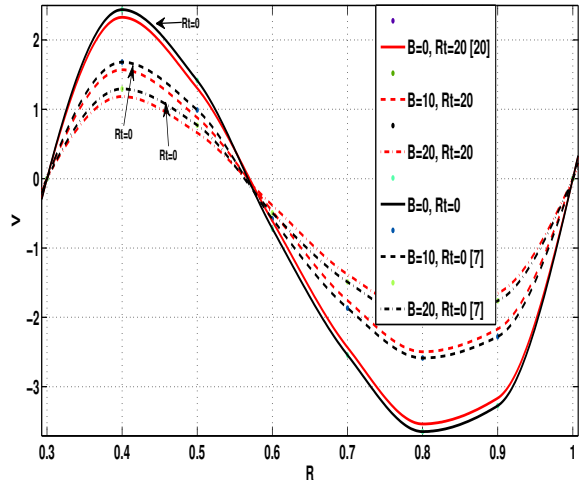

Figure 15. Radial velocity profile for $N = 0.3$ at $Z = 0.02$

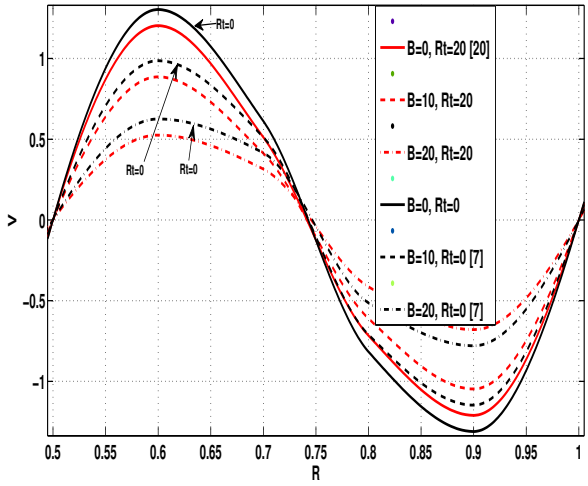

Figure 16. Radial velocity profile for $N = 0.5$ at $Z = 0.02$

region close to the outer wall. The effect of inner wall rotation on the fluid pressure seems to be very low at any cross section. Here also, the results corresponding to $B = 0$ and $Rt = 0$ are in agreement with the earlier results [7, 20], respectively.

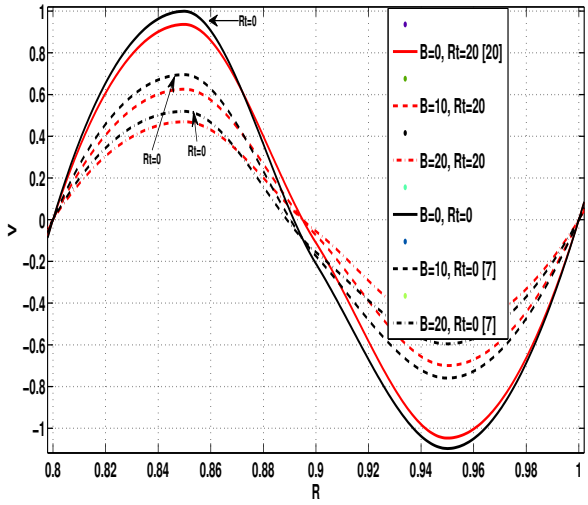

Figure 17. Radial velocity profile for $N = 0.8$ at $Z = 0.02$

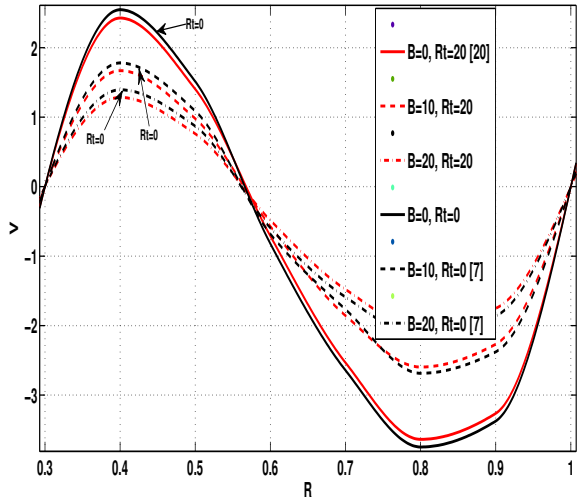

Figure 18. Radial velocity profile for $N = 0.3$ at $Z = 0.03$

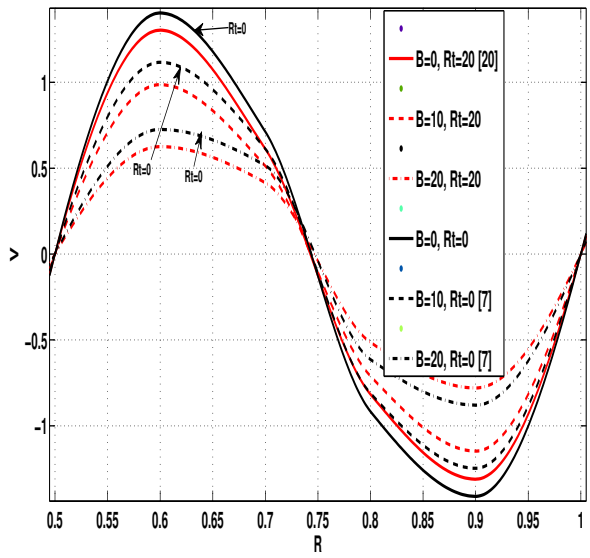

Figure 19. Radial velocity profile for $N = 0.5$ at $Z = 0.03$

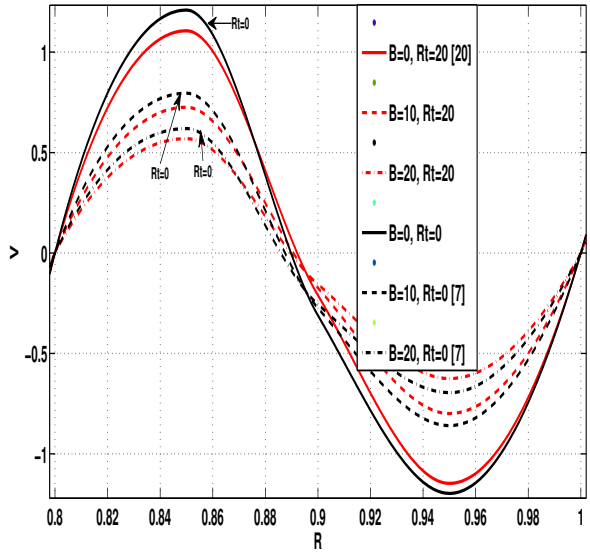

Figure 20. Radial velocity profile for $N = 0.8$ at $Z = 0.03$

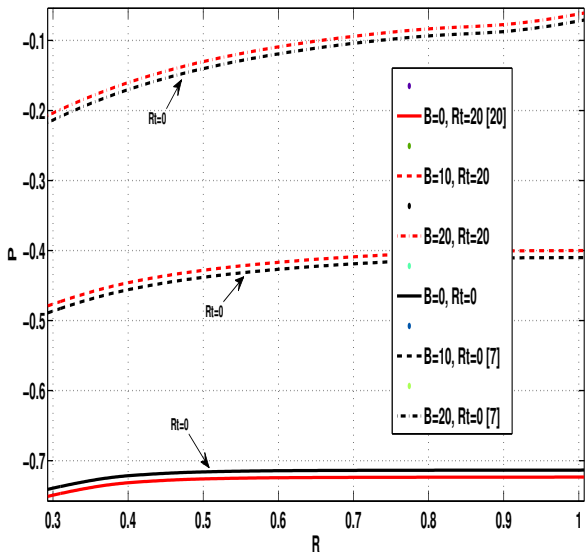

Figure 21. Pressure distribution for $N = 0.3$ at $Z = 0.02$

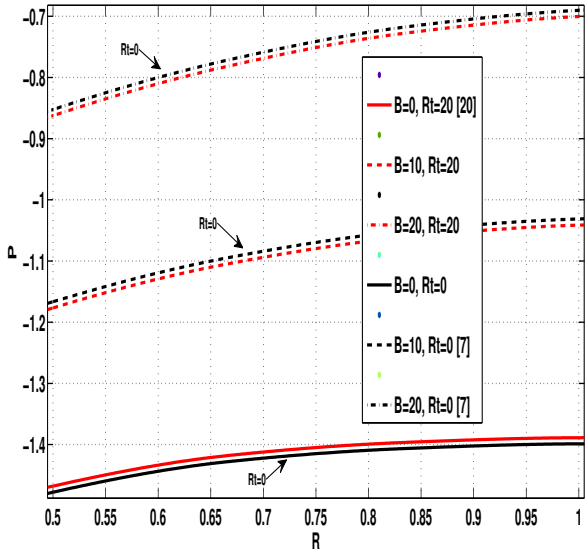

Figure 22. Pressure distribution for $N = 0.5$ at $Z = 0.02$

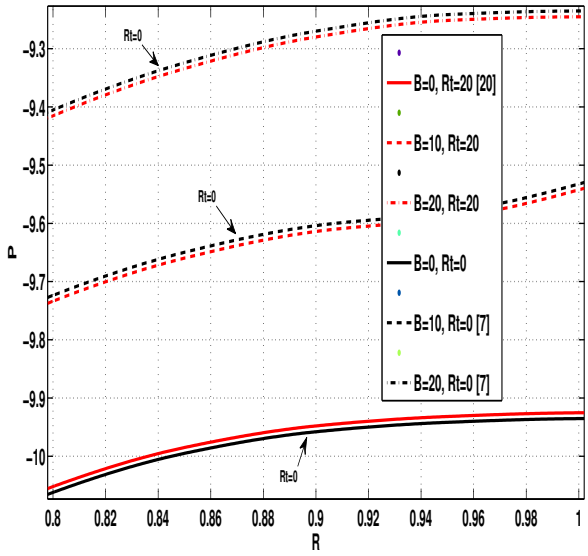

Figure 23. Pressure distribution for $N = 0.8$ at $Z = 0.02$

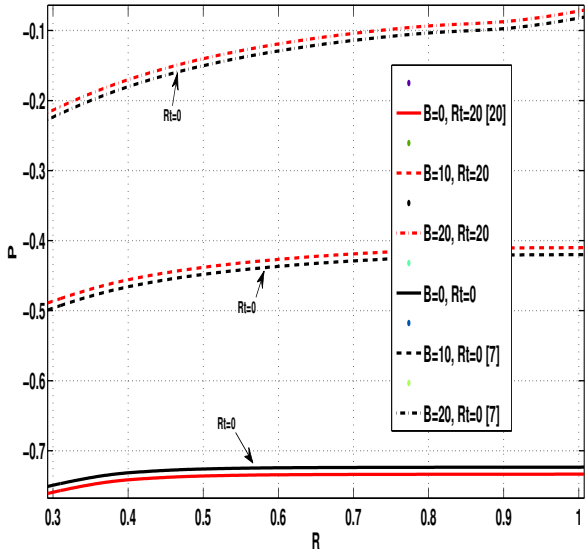

Figure 24. Pressure distribution for $N = 0.3$ at $Z = 0.03$

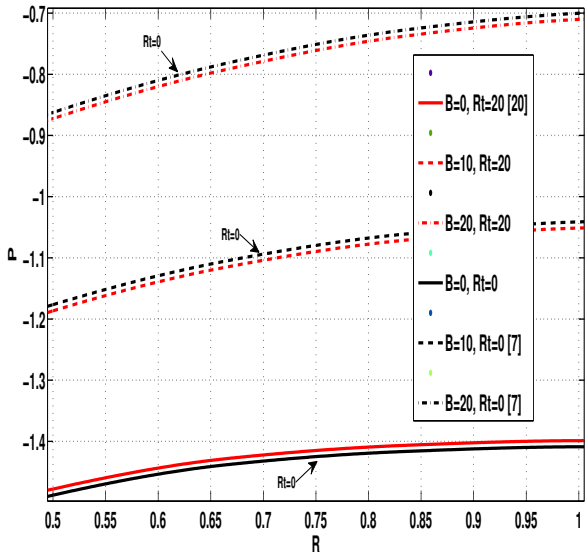

Figure 25. Pressure distribution for $N = 0.5$ at $Z = 0.03$

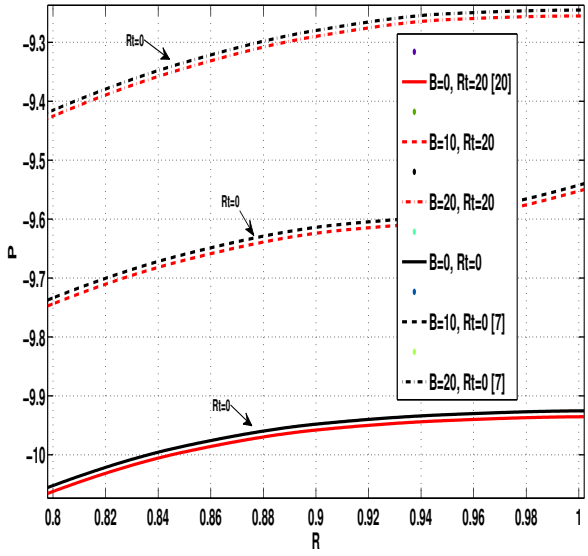

Figure 26. Pressure Distribution for $N = 0.8$ at $Z = 0.03$

5. Conclusion

Numerical results for the entrance region flow in concentric annuli with rotating inner wall for Bingham fluid were presented. The effects of the parameters N, B and Rt on the pressure distribution, the velocity profiles are studied. Numerical calculations were performed for all admissible values of Bingham number B, aspect ratio N and the parameter Rt. The velocity distributions and pressure distribution along radial direction R were presented geometrically. The present results are found to be in agreement with the results corresponding to various particular cases available in literature.

From this study, the following can be concluded.

1. Tangential velocity decreases from the inner wall to the outer wall of the annulus.
2. Increasing the aspect ratio N, the axial velocity component U increases at all values of Bingham numbers B.
3. Radial velocity is found to be dependent only on the axial coordinate.
4. Pressure increases from a minimum at the inner wall to a maximum at the outer wall of the annulus and pressure does not vary much with respect to the radial coordinate in the region near the outer wall.
5. The effect of the inner wall rotation on all these flow characteristics seems to have little significance.

Acknowledgement. The authors would like to express our sincere gratitude to the reviewers and editor for their useful comments and suggestions which have helped the presentation of this work.

References

1. Mishra, I. M., Surendra Kumar and Mishra, P.: Entrance region flow of Bingham plastic fluids in concentric annulus. *Indian Journal of Technology*, **23**, (1985), 81-87.
2. Batra, R. L. and Bigyani, D.: Flow of a Casson fluid between two rotating cylinders. *Fluid Dynamic Research*, **9**, (1992), 133-141.
3. Maia, M. C. A. and Gasparetto, C. A.: A numerical solution for entrance region of non-Newtonian flow in annuli. *Brazilian Journal of Chemical Eng.*, **20**, (2003), 201-211.
4. Sayed-Ahmed, M. E. and Hazem Sharaf-El-Din.: Entrance region flow of a power-law fluid in concentric annuli with rotating inner wall. *International Communications in Heat and Mass Transfer*, **33**, (2006), 654-665.
5. Kandasamy, A. and Srinivasa, R. N.: Entrance region flow in concentric annuli with rotating inner wall for Herschel-Bulkley fluids. *International Journal of Applied and Computational Mathematics*, **1**, (2015), 235-249.
6. Bird, R. D., Dai, G. C. and Yarusso, B. J.: The rheology and flow of viscoplastic materials. *Reviews in Chemical Engineering*, **1**, (1982), 1-70.
7. Kandasamy, A.: Entrance region flow heat transfer in concentric annuli for a Bingham fluid. *In Proceedings of Third Asian-Pacific Conference on Computational Mechanics*, Seoul, Korea, 1996, pp. 1697-1702.

8. Round, G. F. and Yu. S.: Entrance laminar flows of viscoplastic fluids in concentric annuli. *The Canadian Journal of Chemical Engineering*, **71**, (1993), 642-645.

9. Misra, J. C. and Ghosh, S. K.: Flow of a Casson fluid in a narrow tube with a side branch. *International Journal of Engineering science*, **38**, (2000), 2045-2077.

10. Dash, R. K., Mehta, K. N. and Jayaram, G.: Casson fluid flow in a pipe filled with a homogeneous porous medium. *International Journal of Engineering Science*, **34**, (1996), 1145-1156.

11. Ahmed, M. E. S. and Attia, H. A.: Magneto hydrodynamic flow and heat transfer of non-Newtonian fluid in an eccentric annulus. *Canadian Journal of Physics*, **76**, (1998), 391-401.

12. Batra, R. L. and Bigyani Jena: Entrance region flow of blood in concentric annulus. *International Journal of Engineering Science*, **28**, (1990), 407-419.

13. Manglik, R. and Fang, P.: Thermal processing of various non-Newtonian fluids in annular ducts. *International Journal Heat and Mass Transfer*, **45**, (2002), 803-815.

14. Nouar, C., Lebouche, M., Devienne, R. and Riou, C.: Numerical analysis of the thermal convection for Herschel-Bulkley fluids. *International Journal of Heat and Fluid Flow*, **16**, (1995), 223-232.

15. Poole, R. J. and Chhabra, R. P.: Development length requirements for fully developed Laminar pipe flow of yield stress fluids. *Journal of Fluids Engineering*, **132**, (2010), 34501-34504.

16. Galanis, N. and Rashidi, M. M.: Entropy generation in non-Newtonian fluids due to heat and mass transfer in the entrance region of ducts. *Heat Mass Transfer*, **48**, (2012), 1647-1662.

17. Rashidi, M. M., Rajvanshi, S. C., Kavyani, N., Keimanesh, M., Pop, I. and Saini, B. S.: Investigation of heat transfer in a porous annulus with pulsating pressure gradient by homotopy analysis method. *Arabian Journal for Science and Engineering*, **39**, (2014), 5113-5128.

18. Rekha G. Pai and Kandasamy, A.: Entrance region flow of Bingham fluid in an annular cylinder. *International Journal of Applied Engineering Research*, **5**, (2014), 7083-7101.

19. Schlichting, H. and Gersten, K.: *Boundary Layer Theory.* 8th ed., Springer, 2000.

20. Coney, J. E. R. and El-Shaarawi, M. A. I.: A contribution to the numerical solution of developing laminar flow in the entrance region of concentric annuli with rotating inner walls. *Journal of Fluids Engineering*, **96**, (1974), 333-340.

Journal of Computational and Applied Mechanics, Vol. 11., No. 2., (2016), pp. 159–178
DOI: 10.32973/jcam.2016.011

THE BEHAVIOR OF MHD FLOW AND HEAT TRANSFER IN THE PRESENCE OF HEAT SOURCE AND CHEMICAL REACTION OVER A FLAT PLATE

Matthew Oluwafemi Lawal
Department of Mathematics
Adeyemi College of Education, Ondo, Nigeria.
lawalmo@aceondo.edu.ng

Suraju Olusegun Ajadi
Department of Mathematics
Obafemi Awolowo University, Ile-Ife, Nigeria.
sajadi@oauife.edu.ng

[Received: March 23, 2016, Accepted: August 10, 2016]

Abstract. This article is on a study of the behavior of MHD flow and heat transfer in the presence of heat source and chemical reaction over a flat plate. The steady two dimensional partial differential governing equations are transformed using standard dimensionless variables resulting in a coupled nonlinear ordinary differential equation with some embedded parameters. The Homotopy Perturbation Method (HPM) is employed to solve the system of dimensionless equations and the approximate analytical solutions obtained are further analyzed using MAPLE 17 symbolic platform. It is observed that the flow velocity within the boundary layer decreases with increasing magnetic field. Further parametric analysis shows that the temperature increases with increasing Hartmann number while it decreases with increasing Prandtl number. Further observation reveals that temperature profile increases rapidly with increasing heat source and chemical reaction parameters while the concentration profile decreases with increasing heat source and chemical reaction parameters. Graphical demonstrations of these solutions shed more lights on the behavior of the system.

Mathematical Subject Classification: 05C38, 15A15
Keywords: chemical reaction, heat source, HPM, MHD boundary layer, flat plate.

1. Nomenclature

a	[1/s]	stretching rate,
B_o	[-]	applied uniform transverse magnetic field strength, (magnetic induction)
C	[mol/m^3]	dimensional species concentration of the fluid,
C_p	[J/(kg K)]	specific heat capacity at constant pressure,
C_w	[mol/m^3]	species concentration of the fluid along the sheet wall,
C_∞	[mol/m^3]	species concentration of the fluid far away from the sheet wall,
D	[m^2/s]	effective diffusive coefficient or mass diffusion coefficient,

F	[-]	fuel,
M	[-]	Hartmann number,
P	[N/m^2]	pressure,
Pr	[-]	Prandtl number,
Q	[J]	internal heat generation term,
Q_o	[J]	dimensional heat absorption or generation coefficient,
Re	[-]	Reynolds number,
Sc	[-]	Schmidt number,
T	[^oC or K]	dimensional temperature of the fluid,
T_w	[^oC or K]	temperature of the sheet wall,
T_∞	[^oC or K]	dimensional or free stream temperature of the fluid far away from the sheet wall,
U_e	[m/s]	velocity distribution in the boundary layer for external stream,
u, v	[m/s]	velocity components in the directions x and y,
$\hat{u}, \hat{v}$	[-]	dimensionless velocity components in the directions x and y,
x	[m]	axial or vertical coordinate also used as characteristic length,
y	[m]	transverse/horizontal coordinate or non- dimensional distance to the surface.

Greek Symbols

α	[m^2/s]	thermal diffusivity,
θ	[-]	dimensionless temperature,
κ	[kgm/^{o}Cs^3]	constant thermal conductivity,
λ	[-]	heat source/sink parameter,
μ	[kg/ms]	dynamic viscosity,
ν	[m^2/s]	kinematic fluid viscosity,
ρ	[kg/m^3]	fluid density,
σ	[ohm^{-1}m^{-1}]	electrical conductivity of fluid,
τ	[-]	chemical reaction parameter,
ϕ	[-]	dimensionless concentration.

Subscripts and Superscripts

j	[-]	streamwise pressure gradient parameter,
n	[-]	order of reaction,
w	[-]	condition at the wall.

2. Introduction

The study of heat and mass transfer between a moving surface and a fluid dates back to the 1960s when Sakiadis [1, 2] published his first article and pioneering work on boundary layer flow on a continuous moving surface. This area of fluid dynamics has continued to receive attention of many researchers due to its wide applications in many engineering and geophysical applications such as geothermal reservoirs, drying of porous solids, thermal insulation, enhanced oil recovery, packed-bed catalytic reactors, cooling of nuclear reactors and underground energy transport [3, 4, 5]. Ravikumar [6] investigated the heat and mass transfer effect on MHD flow of viscous fluid

through non-homogeneous porous medium in the presence of temperature dependent heat source. The equations governing the flow are solved by a simple perturbation technique and numerical evaluation of the analytical result is reported. As expected, increasing the magnetic parameter reduces the primary profiles and the secondary velocity profiles.

Kandasamy *et al.* [7] studied the effects of chemical reaction, heat and mass transfer on boundary layer flow over a wedge with heat radiation in the presence of suction or injection using the Runge-Kutta Gill method. The result shows that in the presence of heat radiation the velocity and temperature of the fluid decreases and concentration of the fluid increases with increase in chemical reaction parameter. Furthermore, the velocity profiles show that the velocity increases near the plate and thereafter remains uniform. In both cases of suction and injection, it was seen that skin friction increases as chemical reaction increases. Devi and Kandasamy [8] studied the effects of heat and mass transfer on nonlinear boundary layer flow over a wedge with suction or injection. An approximate numerical solution is obtained using the Gill method. The result obtained shows that the flow field is influenced appreciably by the magnetic field and suction or injection at the wall of the wedge.

Muthucumaraswamy [9] investigated the effects of heat and mass transfer on a continuously moving isothermal vertical surface with uniform suction taking into account the homogeneous chemical reaction of first order. A theoretical solution of the problem is obtained in terms of exponential functions. It is observed that the velocity increases during the generative reaction and decreases in the destructive reaction while the concentration increase in the presence of the generative reaction. Sharma [10] discussed in detail the effect of variable thermal conductivity and heat source and sink on MHD flow near a stagnation point on a linearly stretching sheet. The numerical solution shows that the rate of heat transfer at the sheet increases due to the increase in the thermal conductivity parameter, while it decreases due to increase in stretching parameter in the absence of magnetic field and volumetric rate of heat source/sink parameter.

Devi *et al.* [11] analyzed a steady MHD boundary layer flow due to an exponentially stretching sheet with radiation taking into account heat source/sink. By using a fourth order Runge-Kutta method along with shooting technique, they obtained a numerical solution which shows that the momentum boundary layer thickness decreases while both thermal and concentration boundary layer thicknesses increase with an increase in the magnetic field intensity and the radiation reduces the temperature. Gangadhar and Bhaskar [12] analyzed the problem of chemically reacting MHD boundary layer flow of heat and mass transfer over a moving vertical plate in a porous medium with suction. The heat source/sink effects in thermal convection are significant where high temperature differences exist between the surface (e.g. space craft body) and the ambient fluid.

Yih [13] presented an analysis of the forced convection boundary layer flow over a wedge with uniform suction/blowing. The non-similar equations are solved using an implicit finite difference method. It was found that both suction and blowing lead to

a decrease in the values of the local skin friction coefficient and the Nusselt number. Watanabe [14] investigated the behavior of the boundary layer over a wedge with suction or injection in forced flow. The boundary layer equations along a wedge are transformed from partial differential equations into the ordinary differential equations and the non-similar solution are obtained by means of the difference method. The solutions of the resulting equations are expressed in the form of integral equations which are in turn solved by iterative numerical quadratures. Watanabe [14] also reported that "increasing the suction/injection parameter results in wider velocity distribution and narrower temperature distribution, while decreasing the pressure gradient parameter broadens both distributions".

Bhattacharyya [15] analyzed the effect of heat source/sink on MHD flow and heat transfer over a shrinking sheet with mass suction. Employing the finite difference method using quasilinearization technique, it was found that velocity inside the boundary layer increases with increase of wall mass suction and magnetic field and accordingly the thickness of the momentum boundary layer decreases. The temperature decreases with Hartmann number, Prandtl number and heat sink parameter and the temperature increases with heat source parameter. Furthermore, for a strong heat source, heat absorption at the sheet occurs.

Ajadi [16] studied the isothermal flow of a dusty viscous incompressible conducting fluid between two types of motion in the boundary – oscillatory and non-oscillatory, under the influence of gravitational force. Within the framework of some physically realistic approximations and suitable boundary conditions, closed form solutions were obtained. It was observed that the velocity profile of the fluid decreases with increasing time and the particles respond faster to changes in the magnetic field and gravity than in the fluid. Also the skin friction decreases with increasing magnetic field. Dulal *et al*. [17] analyzed the influence of temperature-dependent viscosity and thermal radiation on MHD forced convection over a non-isothermal wedge. A transformed set of non-similar equations was obtained and solved by the Runge-Kutta-Fehlberg Scheme with shooting technique. The velocity and local skin friction coefficient increase with pressure gradient and magnetic field. The temperature profile increases with increasing time-dependent viscosity parameter for liquids while the temperature is higher in the case of gas viscosity parameter is positive, than for liquid viscosity parameter is negative for all values of thermal radiation parameter.

Baoheng [18] presented approximate analytical solution to Falkner-Skan wedge flow with a permeable wall of uniform suction. Comparisons of results from the Homotopy Analysis Method are made with the numerical method by 4th-order Runge-Kutta method combined with Newton-Raphson technique which established validity of the results. It is observed that the velocity profile increases with increasing suction parameter and decreases with increasing pressure gradient parameter.

This present work is undertaken to study the behavior of velocity, temperature and concentration profiles in the presence of a heat source and chemical reaction using the Homotopy Perturbation Method (HPM). The approximate analytical solutions obtained are further analyzed using MAPLE 17 symbolic package. Analysis involving

other important parameters such as Schmidt number, Prandtl number and Hartmann is carried out.

3. Formulation of the Problem

Let us consider a steady, the non-isothermal, unsteady, two-dimensional flow of an electrically conducting fluid with a reaction source based on the one-step exothermic reaction mechanism of the form:

$$F + O \longrightarrow Product + Energy,$$

where F is the fuel and O is the oxidizer. The boundary layer is assumed flat, while the reaction source is placed in the viscous region as shown in Figure 1.

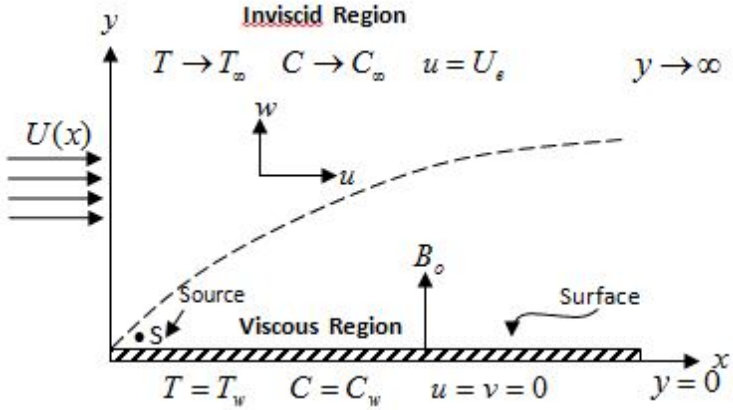

Figure 1. Schematic diagram of the flow

The governing equations of the MHD boundary layer flow in the presence of uniform transverse magnetic field in the viscous region are

$$\frac{\partial u}{\partial x} + \frac{\partial v}{\partial y} = 0, \tag{3.1}$$

$$u\frac{\partial u}{\partial x} + v\frac{\partial u}{\partial y} = \nu\frac{\partial^2 u}{\partial y^2} - \frac{\sigma B_0^2}{\rho}u - \frac{1}{\rho}\frac{\partial P}{\partial x}, \tag{3.2}$$

$$u\frac{\partial T}{\partial x} + v\frac{\partial T}{\partial y} = \frac{\kappa}{\rho C_p}\frac{\partial^2 T}{\partial y^2} + \frac{Q_o}{\rho C_p}(T - T_\infty) + \frac{Q_o}{\rho C_p}C^n e^{-\frac{E}{RT}}, \tag{3.3}$$

$$u\frac{\partial C}{\partial x} + v\frac{\partial C}{\partial y} = \frac{D}{\rho C_p}\frac{\partial^2 C}{\partial y^2} + \delta C^n e^{-\frac{E}{RT}}. \tag{3.4}$$

The boundary conditions for the velocity components, temperature and concentration are given by:

$$u = 0, \quad v = -v_w, \quad C = C_w, \quad T = T_w \qquad \text{at} \quad y = 0, \tag{3.5}$$

$$u = U_e = ax^m, \qquad C \to C_\infty, \quad T \to T_\infty \qquad \text{as} \quad y \to \infty. \tag{3.6}$$

where, u, v, U_e, $v_w > 0$ are the x-component of velocity, y-component of velocity, free stream velocity and prescribed distribution of wall mass suction through the porous plate, respectively.

Introducing the stream function ψ, the velocity components u and v can be written as:

$$u = \frac{\partial \psi}{\partial y} \qquad \text{and} \qquad v = -\frac{\partial \psi}{\partial x}. \tag{3.7}$$

We now introduce the following dimensionless variables:

$$\psi = \sqrt{\nu a} x^{\frac{m+1}{2}} f(\eta), \qquad \eta = \frac{y}{x}\sqrt{Re} = \sqrt{\frac{a}{\nu}} y x^{\frac{m-1}{2}},$$
$$U_e = ax^m, \qquad \theta = \frac{T - T_\infty}{T_w - T_\infty}, \qquad \phi = \frac{C - C_\infty}{C_w - C_\infty}. \tag{3.8}$$

The transformed momentum equation (3.2) becomes

$$f''' + \frac{m+1}{2} f f'' + m[1 - (f')^2] - M^2 f' = 0, \tag{3.9}$$

$$f(0) = S, f'(0) = 0, f'(\infty) = 1. \tag{3.10}$$

The energy equation (3.3) reduces to

$$\theta'' + Pr\left(\frac{m+1}{2} f\theta' + \lambda\theta + \tau\phi e^\theta\right) = 0, \tag{3.11}$$

$$\theta(0) = 1, \theta(\infty) = 0, \tag{3.12}$$

and the specie equation (3.4) gives

$$\phi'' + Sc\left(\frac{m+1}{2} f\phi' - \tau Re \phi e^\theta\right) = 0, \tag{3.13}$$

$$\phi(0) = 1, \phi(\infty) = 0, \tag{3.14}$$

where primes denote the differentiation with respect to η and
$M = (\frac{\sigma B_0^2}{\rho a})^{\frac{1}{2}}$, $Re = \frac{xU_e}{\nu} = \frac{ax^{m+1}}{\nu}$, $Pr = \frac{\mu C_p}{\kappa}$, $Sc = \frac{\nu}{D}$, $\lambda = \frac{Q_o}{\rho C_p a}$,$\tau = \frac{\delta\nu}{U^2}$
and $S = \frac{v_w}{(a\nu)^{1/2}} > 0$ is the mass suction parameter.

4. Mathematical Procedure and Solution

The Homotopy Perturbation Method (HPM) is based on the concept of topology, which has been discovered to be an effective and efficient tool for solving non-linear equations [19-21]. To illustrate Homotopy Perturbation Method, we consider the nonlinear equation:

$$A(u) - f(r) = 0, \ r \in \Omega, \tag{4.1}$$

with the boundary conditions:

$$B\left(u, \frac{du}{dn}\right) = 0, \ r \in \Gamma, \tag{4.2}$$

where A is a general differential operator, B is a boundary operator, $f(r)$ is a known analytic function, and Γ is the boundary of domain Ω. The operator A are generally divided into two parts; L and N, where, L and N are linear and nonlinear parts of A respectively. Therefore, equation (4.1) may be written as

$$L(u) + N(u) - f(r) = 0. \tag{4.3}$$

We construct a Homotopy $v(r,p) : \Omega \times [0,1] \to \Re$

$$H(v,p) = [L(v) - L(u_0)] + pL(u_0) + p[N(u) - f(r)] = 0, \tag{4.4}$$

or

$$H(v,p) = [L(v) - L(u_0)] + p[A(u) - f(r)] = 0. \tag{4.5}$$

Where, $p \,\epsilon\, [0,1]$ is called the homotopy parameter and u_0 is an initial approximation of equation (4.3). At the two extremes $p = 0$ and $p = 1$, we have

$$H(v,0) = [L(v) - L(u_0)] = 0 \qquad \text{and} \qquad H(v,1) = [A(u) - f(r)]. \tag{4.6}$$

In the interval $0 < p < 1$, the homotopy $H(v,p)$ deforms from $L(v) - L(u_0)$ to $A(u) - f(r)$. Thus, the solution of equtions (3.9), (3.11) and (3.13)may be expressed as

$$v = v_0 + v_1 p + v_2 p^2 + v_3 p^3 + v_4 p^4 + ... \tag{4.7}$$

Eventually, at $p = 1$, the system takes the original form of the equation and the final stage of deformation gives the desired solution. Thus taking limits

$$u = \lim_{p \to 1} v = v_0 + v_1 + v_2 + v_3 + v_4 + ... \tag{4.8}$$

We start by applying the Homotopy Perturbation Method to equations (3.9) to (3.14) and we define the homotopy as

$$f''' - f_0''' + pf_0''' + p(\frac{m+1}{2} ff'' + m[1 - (f')^2] - M^2 f') = 0, \tag{4.9}$$

$$\theta'' - \theta_0'' + p\theta_0'' + p[Pr\left(\frac{m+1}{2} f\theta' + \lambda\theta + \tau\phi e^{\theta}\right)] = 0, \tag{4.10}$$

$$\phi'' - \phi_0'' + p\phi_0'' + p[Sc\left(\frac{m+1}{2} f\phi' - \tau Re\phi e^{\theta}\right)] = 0. \tag{4.11}$$

Suppose that the solutions of f, θ and ϕ take the form

$$f(\eta) = f_0(\eta) + f_1(\eta)p + f_2(\eta)p^2 + f_3(\eta)p^3 + f_4(\eta)p^4 + ..., \tag{4.12}$$

$$\theta(\eta) = \theta_0(\eta) + \theta_1(\eta)p + \theta_2(\eta)p^2 + \theta_3(\eta)p^3 + \theta_4(\eta)p^4 + ..., \tag{4.13}$$

$$\phi(\eta) = \phi_0(\eta) + \phi_1(\eta)p + \phi_2(\eta)p^2 + \phi_3(\eta)p^3 + \phi_4(\eta)p^4 + ..., \tag{4.14}$$

substituting equation (4.12) into equation (4.9) and picking terms in order of p, we have

$$p^0 : \quad f_0(\eta) - f_0(\eta) = 0, \tag{4.15}$$

$$p^1 : \quad f_1''' + f_0''' + \frac{m+1}{2} f_0 f_0'' + m[1 - (f_0')^2] - M^2 f_0') = 0, \tag{4.16}$$

$$p^2 : \quad f_2''' + \frac{m+1}{2}(f_0 f_1'' + f_1 f_0'') - m(2f_0' f_1') - M^2 f_1') = 0, \tag{4.17}$$

$$f_0(0) = 0, f_0'(0) = 0, f_0'(\infty) = 0.$$

From the momentum equation and the boundary conditions, we take our initial guess to be

$$f_0(\eta) = \eta - (1 - e^{\eta}). \tag{4.18}$$

Solving equation (4.16) we get

$$f_1''' = e^{\eta} - \frac{m+1}{2}(\eta - (1-e^{\eta}))e^{\eta} + m[1-(1-e^{\eta})^2] + M^2(\eta - (1-e^{\eta})) = 0, \tag{4.19}$$

$$f_1 = -\frac{1}{16}e^{-2\eta}m + \frac{1}{2}e^{-\eta}m + 3me^{\eta} + \frac{1}{16}e^{-2\eta} + \frac{1}{2}e^{-\eta}\eta + M^2e^{-\eta} + \frac{1}{6}M^2\eta^3 + \frac{1}{2}D_1\eta^2 + D_2\eta + D_3. \tag{4.20}$$

Using the boundary condition, we have

$$f_1 = -\frac{1}{16}e^{-2\eta}m + \frac{1}{2}e^{-\eta}m + 3me^{\eta} + \frac{1}{16}e^{-2\eta} + \frac{1}{2}e^{-\eta}\eta + M^2e^{-\eta} + \frac{1}{6}M^2\eta^3 + \frac{1}{2}(\frac{1}{4}M^2e^{-4} - \frac{9}{4}M^2 - \frac{1}{32}e^{-8}m + \frac{9}{8}e^{-4}m + \frac{1}{32}e^{-8} + \frac{3}{8}e^{-4} + \frac{3}{32} - \frac{19}{32}m)\eta^2 + (M^2 + \frac{19}{8}m - \frac{3}{8})\eta - M^2 - \frac{47}{16}m - \frac{1}{16}. \tag{4.21}$$

From equation (4.17)

$$f_2''' = -\frac{m+1}{2}(f_0f_1'' + f_1f_0'') + m(2f_0'f_1') + M^2f_1'). \tag{4.22}$$

The solutions of f_2, f_3 and f_4 have been obtained by integration using MAPLE 17 symbolic package. Hence, the fourth order approximation is given by

$$f = f_0 + f_1 + f_2 + f_3 + f_4 + ... \tag{4.23}$$

Similarly, substituting equations (4.12) and (4.13) into equation (4.10) and picking terms in order of p, we have

$$p^0: \quad \theta_0''(\eta) - \theta_0''(\eta) = 0, \tag{4.24}$$

$$p^1: \quad \theta_1'' + \theta_0'' + Pr\left(\frac{m+1}{2}f_0\theta_0' + \lambda\theta_0 + \tau\theta_0e^{\theta_0}\right) = 0, \tag{4.25}$$

$$p^2: \quad \theta_2'' + Pr\left(\frac{m+1}{2}(f_0\theta_1' + f_1\theta_0') + \lambda\theta_1 + \tau\phi_1e^{\theta_0}\right) = 0, \tag{4.26}$$

$$\theta_0(0) = 1, \theta_0(\infty) = 0.$$

Similarly, from the boundary conditions we take our initial guess to be

$$\theta_0(\eta) = e^{\eta}. \tag{4.27}$$

Solving equation (4.25)

$$\theta_1'' = -\theta_0'' - Pr\left(\frac{m+1}{2}f_0\theta_0' - \lambda\theta_0 - \tau\theta_0e^{\theta_0}\right). \tag{4.28}$$

Similarly, substituting (4.18) and (4.27), then by integration, we obtain

$$\theta_1 = -\frac{1}{2}Pr\eta m e^{-\eta} - \frac{1}{2}Prme^{-\eta} - \frac{1}{2}Pr\eta e^{-\eta} - \frac{1}{2}Pre^{-\eta} - \lambda e^{-\eta} - \tau e^{-\eta} - \frac{1}{8}Pr\eta m e^{-2\eta} - e^{-\eta} - \frac{1}{8}Pr\eta e^{-2\eta} - \frac{1}{4}e^{-2\eta}\tau + E_1\eta + E_2. \quad (4.29)$$

Using the boundary conditions we have

$$\theta_1 = -\frac{1}{2}Pr\eta m e^{-\eta} - \frac{1}{2}Prme^{-\eta} - \frac{1}{2}Pr\eta e^{-\eta} - \frac{1}{2}Pre^{-\eta} - \lambda e^{-\eta} - \tau e^{-\eta} - \frac{1}{8}Pr\eta m e^{-2\eta} - e^{-\eta} - \frac{1}{8}Pr\eta e^{-2\eta} - \frac{1}{4}e^{-2\eta}\tau + (\frac{5}{8}Prme^{-4} + \frac{1}{32}me^{-8}Pr + \frac{5}{8}e^{-4}Pr + \frac{1}{4}\lambda e^{-4} + \frac{1}{4}\tau e^{-4} + \frac{1}{32}e^{-8}Pr + \frac{1}{16}\tau e^{-8} + \frac{1}{4}e^{-4} - \frac{1}{4} - \frac{5}{32}Prm - \frac{5}{32}Pr - \frac{1}{4}\lambda - \frac{5}{16}\tau)\eta + \frac{5}{8}Prm + \frac{5}{8}Pr + \lambda + \frac{5}{4}\tau + 1. \quad (4.30)$$

From equation (4.26)

$$\theta_2'' = -Pr\left(\frac{m+1}{2}(f_0\theta_1' + f_1\theta_0') + \lambda\theta_1 + \tau\phi_1 e^{\theta_0}\right). \quad (4.31)$$

Similarly, the solutions of θ_2, θ_3 and θ_4 are obtained but have not been written here for space economy. The fourth order approximation is given by

$$\theta = \theta_0 + \theta_1 + \theta_2 + \theta_3 + \theta_4 + ... \quad (4.32)$$

Similarly, substituting (4.12)-(4.14) in (4.11) and picking terms in order of p, we have

$$p^0: \quad \phi_0''(\eta) - \phi_0''(\eta) = 0, \quad (4.33)$$

$$p^1: \quad \phi_1'' + \phi_0'' + \left(\frac{m+1}{2}Scf_0\phi_0' - \tau ScRe\phi_0 e^{\theta_0}\right) = 0, \quad (4.34)$$

$$p^2: \quad \phi_2'' + \left(\frac{m+1}{2}Sc(f_0\theta_1' + f_1\theta_0') - \tau ScRe\phi_1 e^{\theta_0}\right) = 0, \quad (4.35)$$

$$\phi(0) = 1, \phi(\infty) = 0.$$

Similarly, from the boundary conditions we take our initial guess to be

$$\phi_0(\eta) = e^{\eta}. \quad (4.36)$$

Similarly, solutions of ϕ_1, ϕ_2, ϕ_3 and ϕ_4 are obtained but have not been written here for space economy. The fourth order approximation is given by

$$\phi = \phi_0 + \phi_1 + \phi_2 + \phi_3 + \phi_4 + ... \quad (4.37)$$

5. Results and discussion.

In our computation, the following values have been selected, Prandtl number (Pr) is taken to be 0.72 which corresponds to air and the values of Schmidt number (Sc) is chosen as 0.62 and 0.78 representing diffusing chemical species of H_2O and NH_3, respectively at $25\,^oC$ and 1 atm, while $m = 0.1, M = 0.2, \lambda = 0.01, Re = 1$ and $\tau = 0.2$, unless stated otherwise.

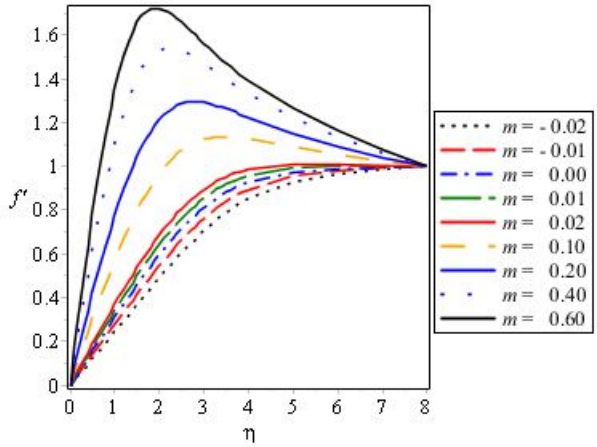

Figure 2. Graphs of f' vs η for some m

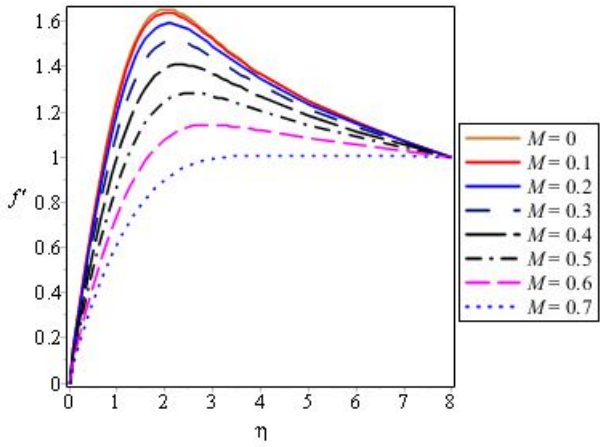

Figure 3. Graphs of f' vs η for some M

Graphical results for the velocity profiles are displayed in Figures 2 and 3 for the influence of m and M, respectively.

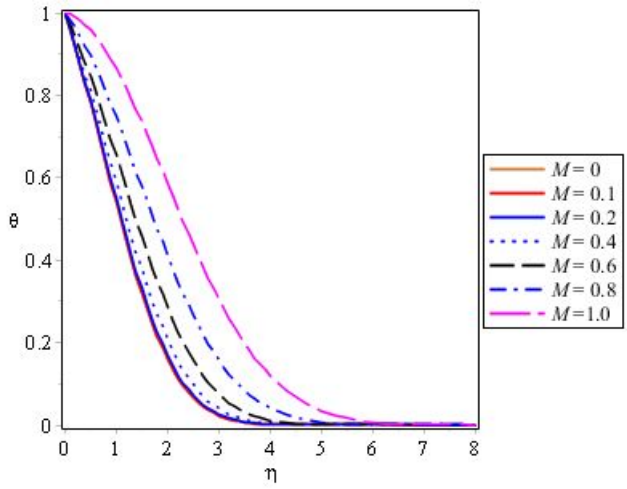

Figure 4. Graphs of θ vs η for some M

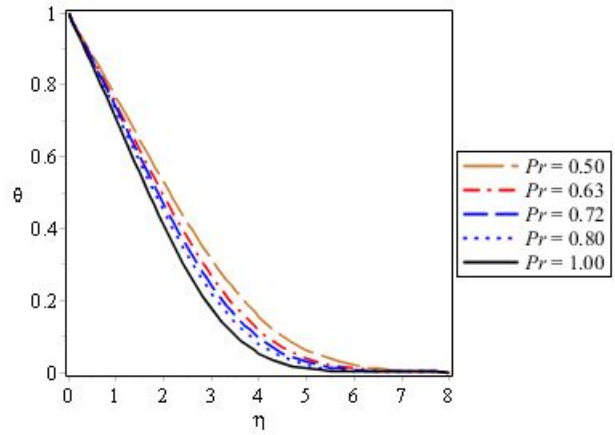

Figure 5. Graphs of θ vs η for some Pr without chemical reaction

It is observed in Figure 2 that the velocity profiles for $m > 0$ is higher than $m < 0$, noting that the velocity profiles is convex for $m > 0$. This is because for a positive value of m, pressure gradient is negative and for a negative value of m, pressure gradient is positive $\left(-\frac{1}{\rho}\frac{\partial P}{\partial x} = U_e\frac{dU_e}{dx} = m\right)$. A negative pressure gradient occurs as a result of pressure decreases in the direction of fluid flow across the boundary layer. Thus the fluid within the boundary layer has enough momentum to overcome the resistance which is trying to push it backward and the flow accelerates. For a positive pressure gradient the pressure increases in the direction of flow, the fluid within the

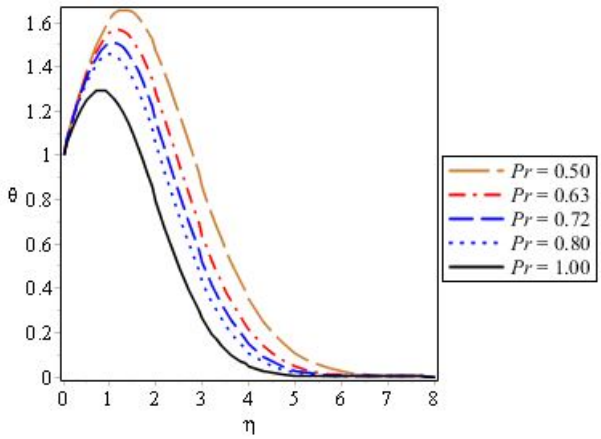

Figure 6. Graphs of θ vs η for some Pr with chemical reaction

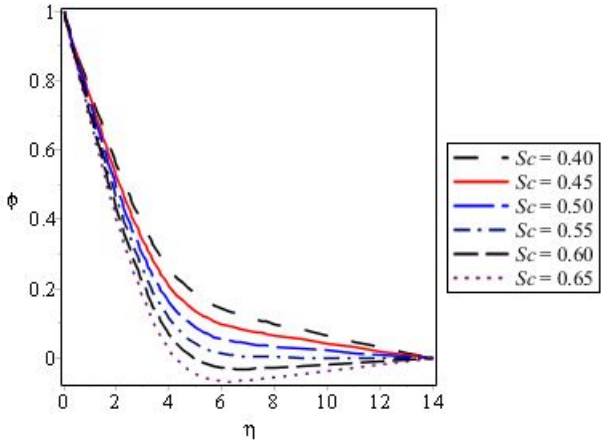

Figure 7. Graphs of ϕ vs η for some Sc at $M = 0.5$

boundary layer has little momentum to overcome this resistance which could make the flow retarded and possibly lead to flow reversal.

The impacts of the Hartmann number M on the velocity and temperature profiles are very significant from a practical point of view. In Figures 3 and 4, the variations in velocity field and temperature distribution for several values of M are presented. The dimensionless velocity $f'(\eta)$ decreases with increasing values of M. This is because the application of transverse magnetic field will result in a resistive force (Lorentz force) similar to drag force which tends to resist the fluid flow thus reducing its velocity, as established by [6] and [8]. On the other hand, Figure 4 shows that the temperature

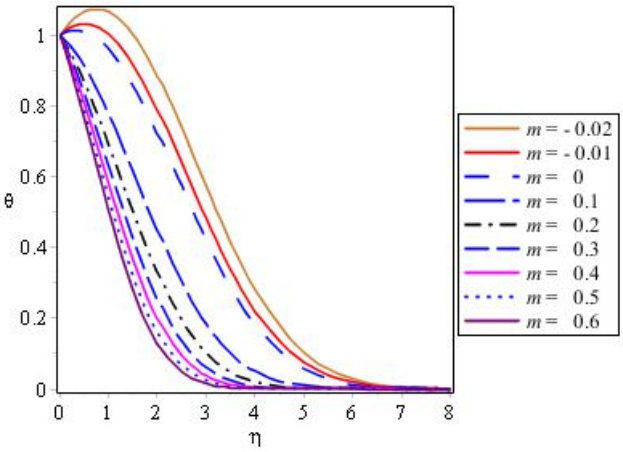

Figure 8. Graphs of θ vs η for some m

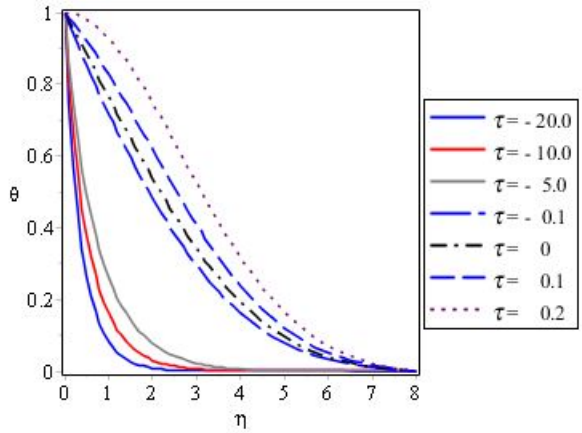

Figure 9. Graphs of θ vs η for some τ

profiles $\theta(\eta)$ increases with increase in M due to the same reason. Similar behavior is observed in Figure 10 for concentration profiles $\phi(\eta)$.

The effect of Prandtl number on the temperature profile in the absence of chemical reaction is shown in Figure 5. It is observed that an increase in the Prandtl number (Pr) decreases the temperature profile. This is justified in that higher values of Prandtl number are equivalent to decrease in the thermal conductivity of the fluid and therefore heat flow is reduced. Hence, there is a reduction in temperature. Figure 6 shows the similar temperature profile pattern with increasing Prandtl number as

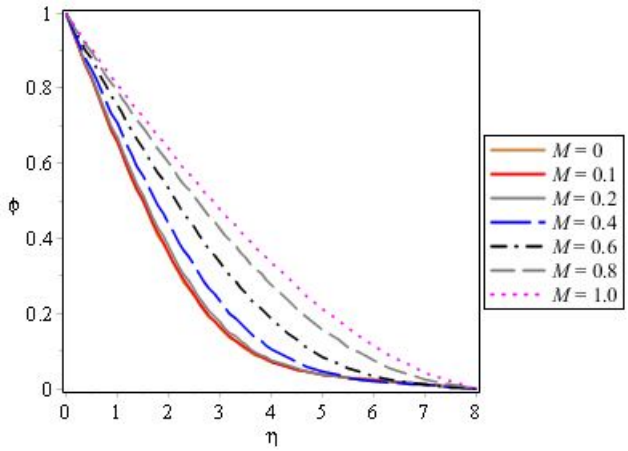

Figure 10. Graphs of ϕ vs η for some M

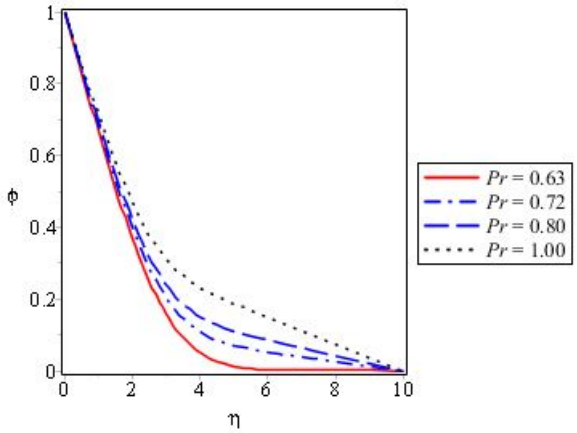

Figure 11. Graphs of ϕ vs η for some Pr

seen in [6], except for the temperature peaks in the interval $0 < \eta < 1.5$, which may be regarded as the reaction zone – a point where the reactant is completely consumed.

Figure 7 shows the effect of Schmidt number on the concentration profile. It is observed that higher Schmidt number reduces the concentration profile. Figure 8 shows that an increase in pressure gradient (m) decreases the temperature profile, which confirms that negative pressure gradient implies accelerated flow, leading to easy convection of heat and hence decrease in temperature.

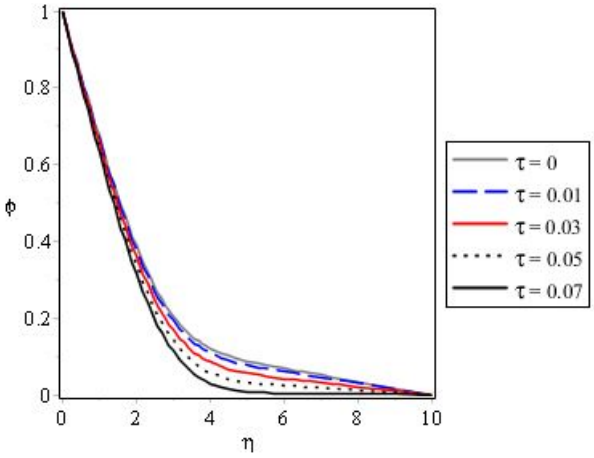

Figure 12. Graphs of ϕ vs η for some τ

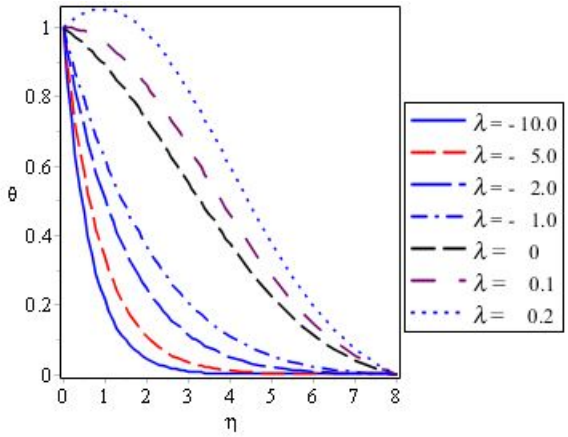

Figure 13. Graphs of θ vs η for some λ

From Figures 9 and 12, it is clear that increasing the chemical reaction term increases the temperature profile while it decreases concentration profile, respectively which is in agreement with the result of Kandasamy [7]. This is because an exothermic reaction involves the release of heat to the surroundings while depletion of the reactant is in process. Figures 7 and 11 show that concentration profile decreases and increases with Schmidt number (Sc) and Prandtl number (Pr) respectively. This is because a large Schmidt number occurs as a result of decrease in mass diffusivity, which reduces concentration across the boundary layer and in general reduces concentration of reactant within the boundary layer.

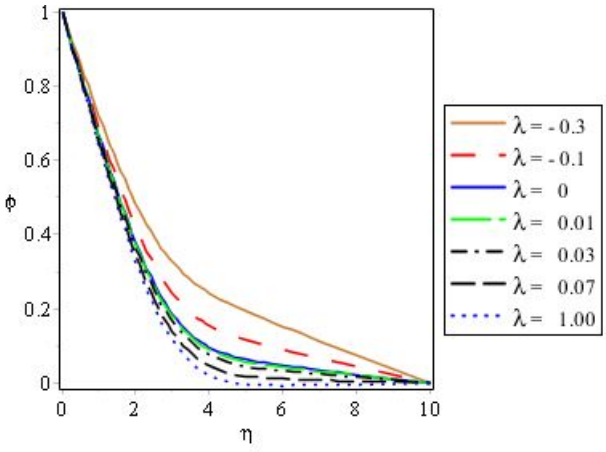

Figure 14. Graphs of ϕ vs η for some λ

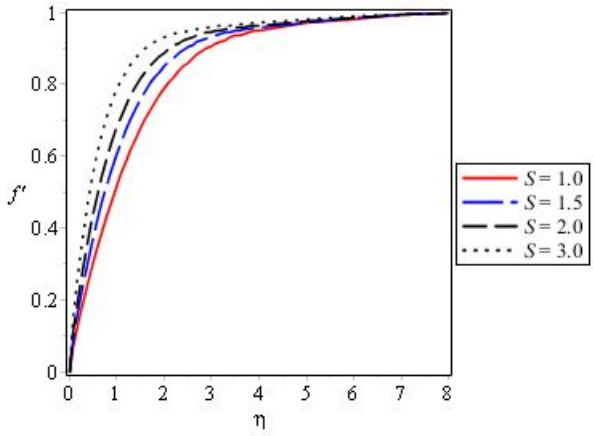

Figure 15. Suction effects on velocity profile

In Figure 11, Prandtl number (Pr) has a negligible effect on concentration $\phi(\eta)$. Figures 13 and 14 show the variation of heat source parameter on temperature and concentration, respectively. It is quite interesting to note that a relatively high heat source term results in a very high temperature at the reaction zone, while it decreases the concentration profile. The velocity profiles for various values of suction parameter S are depicted by Figure 15. It is noted that the velocity profiles increase as applied suction increases and this makes the momentum boundary layer thinner.

From Figure 16 it is seen that the wall suction affects the temperature distribution: increase in suction decreases the temperature, meaning that the thermal boundary

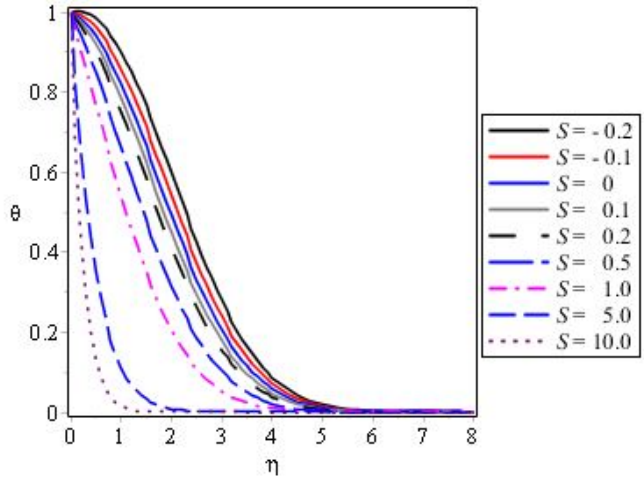

Figure 16. Suction effects on temperature profile

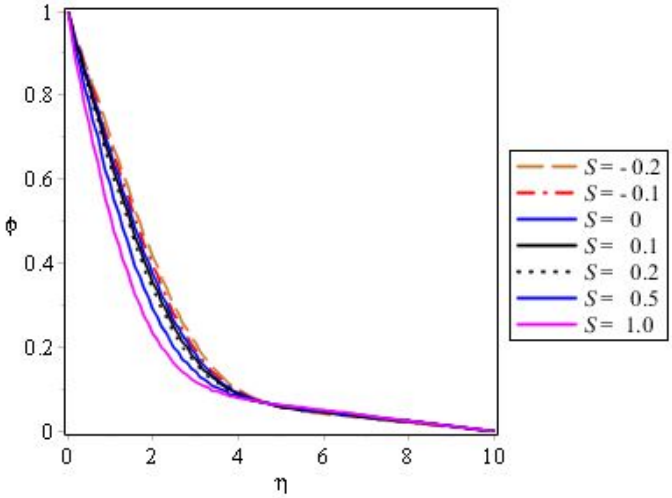

Figure 17. Suction effects on concentration profile

layer thickness reduces. Also, Figure 17, shows the suction effects on concentration profile.

The behavior of the local skin friction coefficient$(-f''(0))$, Nusselt number$(\theta'(0))$ and Shearwood number$(-\phi'(0))$ with respect to the embedded parameters in the system were also carried out as shown in Table 1.

Table 1. Computation showing $f''(0)$, $\theta'(0)$ and $\phi'(0)$

m	M	Pr	Sc	τ	λ	-$f''(0)$	$\theta'(0)$	-$\phi'(0)$
0.2	0.1	0.2	0.2	0.1	0.1	0.638110901	-0.025503349	0.2440132260
0.2	0.1	0.2	0.2	0.1	0.3	0.638110901	1.030907124	0.2440132260
0.2	0.1	0.2	0.2	0.2	0.1	0.638110901	2.835536353	0.8162211665
0.2	0.1	0.2	0.2	0.3	0.1	0.638110901	3.431586291	0.9354311542
0.2	0.1	0.2	0.3	0.1	0.1	0.638110901	-0.025503349	0.2916972210
0.2	0.1	0.2	0.4	0.1	0.1	0.638110901	0.125412432	0.1254124320
0.2	0.1	0.3	0.2	0.1	0.1	0.638110901	0.125412432	0.1254124320
0.2	0.1	0.4	0.2	0.1	0.1	0.638110901	0.188537086	0.1885370865
0.2	0.2	0.2	0.2	0.1	0.1	0.644682861	0.125412432	0.1254124320
0.2	0.3	0.2	0.2	0.1	0.1	2.206428834	0.125412432	0.1254124320
0.3	0.3	0.2	0.2	0.1	0.1	0.735052197	0.127516587	0.1275165872

From the table it can be seen that the skin friction and the Nusselt number increase with increasing pressure gradient m while the Shearwood number decreases. The heat source parameter has no significant effect on local skin friction coefficient and Shearwood number but increases Nusselt number. Also the local skin friction coefficient is not affected or influenced by the chemical reaction parameter, Prandtl number or Schmidt number; Nusselt number increases with increasing chemical reaction parameter, Prandtl number and Schmidt number; Sherwood number increases with increasing chemical reaction parameter and Prandtl number but decreases with increasing Schmidt number. Furthermore the Nusselt and Sherwood numbers are not influenced in any way by Hartmann number M but the skin friction coefficient increases with increasing M. This is because Hartmann number M represents the relative influence of the magnetohydrodynamic drag force (Lorentz body force) and the momentum force on the flow.

6. Conclusion

This present study investigated the behavior of MHD flow and heat transfer in the presence of heat source and chemical reaction over a stretching sheet. The governing continuity, momentum, energy and concentration equations of the flow are non-dimensionalized by introducing some standard dimensionless variables. The resulting equations were solved by employing Homotopy Perturbation Method (HPM). The approximate analytical solutions obtained are further analyzed using MAPLE 17 symbolic package. Analyses involving some important parameters such as Schmidt number, Prandtl number, Hartmann number, pressure gradient, chemical reaction and heat source parameters were carried out. The results are summarized as follows

- The temperature increases while concentration decreases with increasing heat source parameter.
- The concentration profile reduces with increasing Schmidt number .
- The magnetic field and Prandtl number enhance the temperature profile.
- Increasing suction parameter increases velocity but decreases temperature.

- The skin friction coefficient is not affected or influenced by chemical reaction parameter, Prandtl number or Schmidt number; the Nusselt number increases with increasing chemical reaction parameter, Prandtl number, Schmidt number; the Sherwood number increases with increasing chemical reaction parameter and Prandtl number but decreases with increasing Schmidt number.

Acknowledgement. This work has been supported in part by the Nigerian Tertiary Education Trust Fund (TETfund). Acknowledgment also goes to the Central European University Fellowship Programme, Budapest, where the work was initiated during the visit of the second author as a Research Fellow. Authors acknowledge with gratitude the constructive comments and suggestions of the reviewers which improved the quality of the paper.

References

1. Sakiadis, B. C.: Boundary-layer behaviour on continous solid surface. I. Boundary-layer equations for two-dinmensional and axisymmettic flow. *AIChE Journal*, **7**, (1961), 26–28.
2. Sakiadis, B. C.: Boundary-layer behaviour on continous solid surface. II. Boundary-layer equations for two-dinmensional and axisymmettic flow. *AIChE Journal*, **7**, (1961), 221–225.
3. Pijush K. Kundu and Ira M. Cohen: *Fluid Mechanics*. Fourth edition, Elsevier, The Boulevard, Langford lane Kidlington, Oxford, UK, 2008.
4. Wang, C. Y.: Liquid film on an unsteady stretching sheet. *Quarterly of Applied Mathematics*, **48**(4), (1990), 601–610.
5. Fang, T. and Zhang, J.: Flow between two strehable disks - An Exact solution of the Navier-Stokes equation. *International Communication in Heat and Mass Transfer*, **35**, (2008), 892–895.
6. Ravikumar, V., Kaju M. C. and Raju G. S. S.: Heat and mass transfer effects on MHD flow of viscous fluid through non-homogeneous porous medium in presence of temperature dependent heat source. *International Journal of Contemporary Mathematical Sciences*, **7**(32), (2012), 1597–1604.
7. Kandasamy, R., Abd, W. B., Raj, M. and Khamis, A. B.: Effects of chemical reaction, heat and mass transfer on boundary layer flow over a porous wedge with radiation in the presence of suction or injection. *Theoretical and Applied Mechanics, Belgrade.* **33**(2), (2006), 123–148.
8. Devi, A. S. P. and Kandasamy, R.: Effects of heat and mass transfer on MHD laminar boundary layer flow over a wedge with suction or injection. *Journal of Energy Heat and Mass Transfer*, **2**, (2001), 167.
9. Muthucumaraswamy, R.: Effect of a chemical reaction on a moving isothermal vertical surface with suction. *Acta Ciencia Indica*, **155**, (2002) 65–70.
10. Sharma, P. R. and Singh, G.: Effects of variable thermal conductivity and heat source/sink on MHD flow near a stagnation point on a linearly stretching sheet. *Journal of Applied Fluid Mechanics*, **2**, (2008), 13–21.
11. Devi, R. L. V. R., Poornima, T., Reddy, N. B. and Venkataramana, S.: Radiation and mass transfer effects on MHD boundary layer flow due to an exponentially stretching

sheet with heat source. *International Journal of Engineering and Innovative Technology*, **3**(8), (2014), 33–38.

12. Gangadhar, K. and Bhaskar, R. N.: Chemically reacting MHD boundary layer flow of heat and mass transfer over a moving vertical plate in a porous medium with suction. *Journal of Applied Fluid Mechanics*, **6**(1), (2013), 107–114.
13. Yih, K. A.: Uniform suction/blowing effect on force convection about wedge. *Acta Mechanica*, **128**, (1998), 173-181.
14. Watanabe, T.: Thermal boundary layer over a wedge with suction or injection in force flow. *Acta Mechanica*, **83**, (1990), 119-126.
15. Bhattacharyya, K.: Effects of heat source/sink on MHD flow and heat transfer over a shrinking sheet with mass suction. *Chemical Engineering Research Bulletin*, **15**, (2011), 12–17.
16. Ajadi, S. O.: A note on the unsteady flow of dusty viscous fluid between two parallel plates. *Journal of Applied Mathematics and Computing*, **18**(1), (2005), 393–403.
17. Dulal, P. and Hiranmoy, M.: Influence of temperature-dependent viscosity and thermal radiation on MHD forced convection over a no-isothermal wedge. *Applied Mathematics and Combustion*, **212**, (2009), 194–208.
18. Baoheng, Y.: Approximate Analytical Solution to the Falkner-Skan wedge flow with the permeable wall of uniform suction. *Commun Nonlinear Sci Numer Simulat*, **14**, (2009), 3320–3326.
19. Ajadi, S. O. and Zuilino, M.: Approximate analytical solutions of reaction-diffusion equations with exponential source term; Homotopy perturbation method. *Applied Mathematics letters*, **24**, (2011), 1634–1639.
20. Ajadi, S. O.: Approximate analytical solution for critical parameters in a thermal explosion problem. *Applied Mathematics and combustion*, **218**, (2011), 2005–2010.
21. Taghipour, R.: Application of Homotopy perturbation method on some linear and nonlinear parabolic equations. *International Journal of Recent Research and Applied Studies*, **6**(1), (2011), 55–59.

Journal of Computational and Applied Mechanics, Vol. 11., No. 2., (2016), pp. 179–196
DOI: 10.32973/jcam.2016.012

ACOUSTIC SOURCE TERM FORMULATIONS IN THE CAVITY TONE

Péter Tamás Nagy
Department of Hydrodynamic Systems, Budapest University of Technology and Economics
Budapest, H-1111, Hungary
pnagy@hds.bme.hu

Andreas Hüppe
Institute of Mechanics and Mechatronics, Vienna University of Technology
Vienna, A-1060, Austria
andreas.hueppe@tuwien.ac.at

Manfred Kaltenbacher
Institute of Mechanics and Mechatronics, Vienna University of Technology
Vienna, A-1060, Austria
manfred.kaltenbacher@tuwien.ac.at

György Paál
Department of Hydrodynamic Systems, Budapest University of Technology and Economics
Budapest, H-1111, Hungary
paal@hds.bme.hu

[Received: March 8, 2016, Accepted: August 22, 2016]

Abstract. The cavity tone at low speed is simulated by a hybrid aeroacoustic approach. Thereby, a rectangular, open cavity with a length-to-depth ratio 2 is investigated at a Mach number of about 0.05. We compared various source formulations (velocity, pressure, divergence of Lighthill tensor, Lamb vector) to each other. The simulations were carried out by ANSYS CFX and the in-house code CFS++. The results indicate that velocity based formulations provide better results.

Mathematical Subject Classification: 35E99
Keywords: cavity tone, CAA, CFD, source term, low Mach number, implicit damping in CFX

1. Introduction

In this paper cavity tone is investigated, which is one of the fundamental aeroacoustic flow configurations (Figure 1). The "cavity" is a rectangular cutout in a surface, typically a plane. If there is flow over the cavity, a shear layer is formed, which can lose its stability. The instability wave propagates from the leading edge to the downstream (trailing) edge, while the amplitude of the wave continuously increases; thus,

a feedback mechanism develops between the leading and trailing edge. The pressure fluctuation at the trailing edge perturbs the shear layer at the leading edge, where the previously mentioned instability waves are generated. This feedback mechanism leads to oscillations that are sometimes even audible. Apart from the generated sound, this phenomenon usually leads to unwanted mechanical vibrations and also to increased drag force.

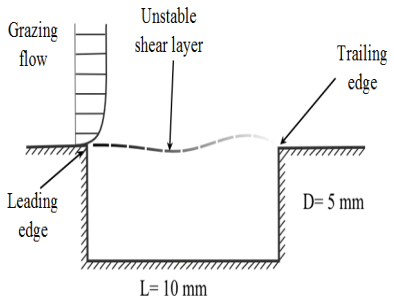

Figure 1. The investigated configuration of cavity-tone

The first studies on cavity noise concerned aeronautic applications in the 1950-1960s [1]. The motivation of research was that the oscillations appeared in the weapon bays of military aircraft. This oscillation can excite the vibrational modes of the aircraft structure, which can quickly lead to structural fatigue issues inside the aircraft [2] and can significantly increase the drag force, too. The speed of the flow was high subsonic to supersonic in these cases. The need to investigate configurations at lower velocities appeared in the 1970s mainly because aircraft wheel wells were seen to be an important source of aerodynamic noise during the landing and take-off of airplanes [3, 4]. In the meantime many other technical applications have been discovered: door gaps and sunroofs in automobiles, closed side branches in gas pipelines, slotted flumes, slotted wall wind and water tunnels, bellows-type pipe geometries [5], canal locks, harbor entries and gaps between wagons or the pantograph of trains [6].

In this paper a fundamental open cavity with length-to-depth ratio of 2 is investigated at a flow speed of about 0.05 Ma (Mach-number, defined as the ratio of far field velocity of the flow and the speed of sound). At such a low Mach number the disparity of scales of the acoustic and the flow field is significant. The grid of the flow simulation must be fine enough to resolve the boundary layer and small vortices to provide sufficiently accurate results. Usually the desired grid resolution for acoustic computation can be much coarser because the acoustic wavelength is much larger than the vortices or even the cavity. In addition, there are several orders of magnitude differences in the aerodynamic and acoustic variables. E.g. a 1 m/s velocity fluctuation is not extreme in flows, while the amplitude of the acoustic velocity fluctuation at a particle velocity level of 80 dB is only 0.5 mm/s. The human hearing threshold at 1 kHz is around 0 dB sound pressure level, corresponding to 20 μPa

in air, which is again several orders of magnitude smaller than an average pressure fluctuation in aerodynamics (10–100 Pa). These orders of magnitude differences between the variables increase the numerical noise, which can spoil the whole acoustic simulation [7]. To reduce these errors it is typical to separate the acoustic and the aerodynamic flow fields. The common name for these approaches is hybrid Computational AeroAcoustics (CAA). If the two fields are separated, the crucial point of the computation is to determine the coupling between them. The idea is to derive equations for the acoustic field (model the acoustic field) and then to define source terms, which are based on the independently solved flow field. The optimal formulation of these equations and source terms is still under research. In this paper various source terms are investigated for the acoustic wave equation. Some of them are valid only for incompressible fluid. The compressibility in our cavity configuration does not play an important role, allowing us to carry out incompressible flow simulations and to use coupling formulations that are valid only for incompressible flow. At the same time a compressible flow simulation was also carried out to verify the previous statement and to investigate the effect of compressibility to the sources.

In Section 2 the governing equations of fluid dynamics are presented briefly and based on them the various formulations of the source terms are introduced. In Section 3 the CFD simulations are described and their acoustic source fields are compared to each other. In Section 4 the acoustic simulations are presented. Finally, in Section 5 we make some concluding remarks.

2. Source term formulation

2.1. **The acoustic wave equation with general sources.** The basic equations, which describe both the flow and acoustic field, are the conservation equations of mass, momentum and energy

$$\frac{\partial \rho}{\partial t} + \nabla \cdot (\rho \underline{\mathrm{u}}) = 0, \tag{2.1}$$

$$\frac{\partial (\rho \underline{\mathrm{u}})}{\partial t} + \nabla \cdot (\rho \underline{\mathrm{u}} \otimes \underline{\mathrm{u}}) = \nabla \cdot \underline{\underline{\mathrm{T}}}, \tag{2.2}$$

$$\frac{\partial \rho e}{\partial t} + \nabla \cdot (\rho e \underline{\mathrm{u}}) = \nabla \cdot (-p \underline{\mathrm{u}} + \underline{\underline{\tau}} \underline{\mathrm{u}}) + \nabla \cdot (\lambda \nabla T), \tag{2.3}$$

where ρ is the density, t is the time, ∇ is the "nabla" operator, $\underline{\mathrm{u}}$ is the velocity vector, $\underline{\underline{\mathrm{T}}}$ is the stress tensor, e is the total energy, p is the pressure, $\underline{\underline{\tau}}$ is the viscous stress tensor, T is the temperature. The following expressions hold if the fluid is Newtonian (equation (2.4)) and an ideal gas is assumed (equation (2.5))

$$\underline{\underline{\mathrm{T}}} = -\left(p + \frac{2}{3}\mu \nabla \cdot \underline{u}\right) \underline{\underline{\mathrm{I}}} + \mu \left(\nabla \otimes \underline{\mathrm{u}} + (\nabla \otimes \underline{\mathrm{u}})^T\right), \tag{2.4}$$

$$e = \frac{p}{\rho(\gamma - 1)} + \frac{u^2}{2}, \tag{2.5}$$

where μ is the dynamic viscosity, $\underline{\underline{\mathrm{I}}}$ is the identity tensor. Now let us split the variables into mean (time averaged) and fluctuating components as

$$f(t,x) = \bar{f}(x) + f^{'}(t,x)\,, \tag{2.6}$$

and neglect the viscous and non-linear terms. Then the following expression can be obtained

$$\frac{1}{c_0^2}\frac{\partial p^{'}}{\partial t} + \nabla \cdot \rho \underline{\mathrm{u}}^{'} = \Phi_{cont}, \tag{2.7}$$

$$\frac{\partial \rho \underline{\mathrm{u}}^{'}}{\partial t} + \nabla p^{'} = \underline{\Phi}_{mom}. \tag{2.8}$$

where Φ_{cont} and $\underline{\Phi}_{mom}$ are general sources for the equations and c_0 is the speed of sound.

Let us take the time derivative of (2.7) and the divergence of (2.8), and assume the fluctuating variables to be purely acoustic, denoted by superscript "a" (see [8] for details). Then the velocity can be eliminated and we get the well-known wave equation for the acoustic pressure with the sources (S) on the right-hand side

$$\frac{1}{c_0^2}\frac{\partial^2 p^a}{\partial t^2} - \Delta p^a = \underbrace{\frac{\partial}{\partial t}\Phi_{cont} - \nabla \cdot \underline{\Phi}_{mom}}_{\mathrm{S}}\,. \tag{2.9}$$

2.2. **The Lighthill analogy.** The first, most famous and still widely used analogy is the one proposed by Lighthill in 1951 [9]. The basic idea of Lighthill was that the terms, neglected during the derivation (linearization) of the wave equation, act as sources for the acoustic equation, i. e.

$$\mathrm{S} = \nabla \cdot \underline{\Phi}_{mom} = \nabla \cdot \nabla \cdot \underline{\underline{\mathrm{T}}}_{LH}. \tag{2.10}$$

The original form of the Lighthill-tensor is

$$\underline{\underline{\mathrm{T}}}_{LH} = \rho \underline{\mathrm{u}} \otimes \underline{\mathrm{u}} + p^{'}\underline{\underline{\mathrm{I}}} - \underline{\underline{\tau}} - \mathrm{c}_0^2\,(\rho - \rho_0)\,\underline{\underline{\mathrm{I}}}. \tag{2.11}$$

where ρ_0 is the ambient density. Lighthill assumed that if the viscous terms are small (the Reynolds-number is high), the process is close to isentropic and the main sources of sound are vortices, then the tensor can be approximated by

$$\underline{\underline{\mathrm{T}}}_{LH} \approx \rho \underline{\mathrm{u}} \otimes \underline{\mathrm{u}}. \tag{2.12}$$

In what follows, we shall also employ the above simplification.

2.3. **Approximation of the Lighthill analogy.** The following approximations of the Lighthill tensor can be found in [8].

2.3.1. *The Lamb vector.* Let us decompose the velocity field according to Helmholtz into an irrotational and a solenoidal vector field. If we assume that the Lighthill source term is based on the incompressible velocity the following relation holds

$$\mathrm{S} = \nabla \cdot \nabla \cdot \left(\rho \underline{\mathrm{u}}^{ic} \otimes \underline{\mathrm{u}}^{ic}\right) = \nabla \cdot \left(\rho \underline{\omega} \times \underline{\mathrm{u}}^{ic}\right) + \nabla \cdot \nabla \left(\frac{1}{2} \rho \underline{\mathrm{u}}^{ic} \cdot \underline{\mathrm{u}}^{ic}\right), \tag{2.13}$$

where u^{ic} is the solenoidal part of the velocity after Helmholtz decomposition.

2.3.2. *The Laplacian of the pressure.* The Lighthill tensor can be approximated by the incompressible pressure in the following way. Let us neglect the viscous terms in equation (2.2) and take its divergence, which leads to

$$\nabla \cdot \left(\frac{\partial \left(\rho \underline{\mathrm{u}}\right)}{\partial t}\right) + \nabla \cdot \nabla \cdot \left(\rho \underline{\mathrm{u}} \otimes \underline{\mathrm{u}}\right) = -\Delta p. \tag{2.14}$$

In an incompressible fluid the first term on the left-hand side is zero because of the incompressible continuity equation and the symmetry property of the spatial and temporal derivatives. The second term on the left-hand side is the approximation of the previously mentioned Lighthill tensor,

$$\nabla \cdot \nabla \cdot \underline{\underline{\mathrm{T}}}_{LH} \approx \nabla \cdot \nabla \cdot \left(\rho \underline{\mathrm{u}} \otimes \underline{\mathrm{u}}\right) \approx -\Delta p. \tag{2.15}$$

This relation is valid only, if the viscous terms are negligible, i.e. the Reynolds-number is high.

2.3.3. *The time derivative of the pressure.* The following source term formulation and a detailed, exact derivation of it can be found in [7], we give here only a short, rudimentary derivation. If a quiescent medium is assumed,equation (2.7) is still valid for fluctuating variables. First, let us split the fluctuating pressure into acoustic and incompressible pressure. Then, we take the time derivative and rearrange the incompressible pressure to the right-hand side. This term can be conceived as the source term for the continuity equation,

$$\Phi_{cont} = -\frac{1}{c_0^2} \frac{\partial p^{ic}}{\partial t}. \tag{2.16}$$

If we substitute into equation (2.9), the source term can be calculated as

$$S = \frac{\partial \Phi_{cont}}{\partial t} = -\frac{1}{c_0^2} \frac{\partial^2 p^{ic}}{\partial t^2}. \tag{2.17}$$

3. CFD simulations and acoustic load

3.1. **The CFD simulation domain.** In the first step 2D CFD simulations were performed using ANSYS CFX. The cavity dimensions were the following: the length of the cavity was $\mathrm{L} = 10$ mm; the depth of the cavity was $D = 5$ mm. The simulation domain was defined to be a length of $2L$ before the cavity, a length of $3L$ after the cavity and 3L above the cavity. A sponge layer around the simulation domain was

necessary in the compressible simulation to avoid reflection at the boundaries. The thickness of this layer was $4.5L$ in both horizontal and vertical directions. The mesh was generated by ANSYS ICEM. The finest mesh resolved the cavity by 166x106 cells. The monitor point was placed $0.07D$ below the corner on the rear cavity wall, which is the most favorable place (experimentally measurable, smaller residuals, larger pressure signal) for the investigation (see [1, 10]).

Table 1. The main parameters of the CFD simulations

Name	Value
Mach number	0.05
Far-field velocity	17.306 m/s
Length of cavity	10 $[mm]$
Depth of cavity	5 $[mm]$
Boundary layer thickness at leading edge	1.22 $[mm]$
Kinematic viscosity	1.545 $\times 10^{-5}$ $[m^2/s]$
Reynolds number (Re_L)	$\sim$ 11200
Density	1.185 $[kg/m^3]$
Reference temperature	25 $[°C]$
Flow model	Laminar flow was assumed

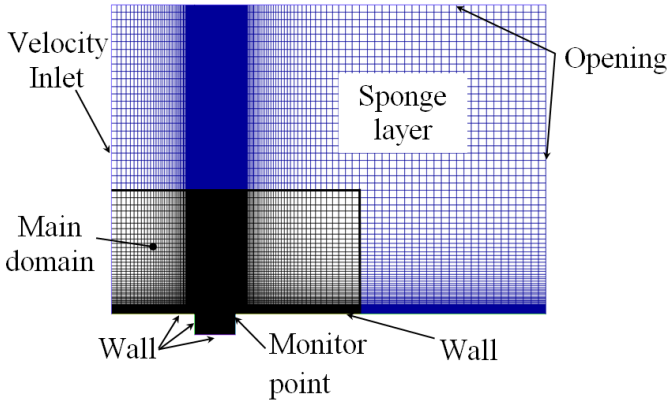

Figure 2. The CFD domain

The CFD domain with the applied boundary conditions can be seen in Figure 2. The velocity inlet boundary condition (BC) was a prescribed velocity profile. This velocity profile was calculated by an in-house MatLab code that generates the Blasius profile. This code provides the prescribed value of boundary layer thickness at the

leading edge. It was 1.22 mm in these simulations. The walls at the bottom were modeled as adiabatic "no-slip walls". At the outlet and the top of the domain the so-called "opening" boundary condition was used [11], which prescribes the relative pressure (0 Pa) and the flow direction (normal to the boundary). However, if the pressure is rigorously constant in a compressible simulation, the acoustic waves are reflected from the boundary. The solution to avoid such a problem will be discussed in the next subsection. The advection scheme was set to "High Resolution" (second order scheme) while second order backward Euler transient scheme was applied. Two constant timestep sizes were applied: $1e^{-6}$ s and $2.5e^{-7}$ s, meaning the rms Courant-Friedrich-Levy number were around 0.53 and 0.14, respectively. Between the two results no significant difference was obtained. During the solution the convergence criteria for the iteration was that the root mean square of the residuals had to be smaller than 10^{-5}.

Table 2. Mesh parameters of the CFD simulations

Case	Resolution of cavity	Smallest element edge length	Number of elements
Coarse	141x71	20 μm	$\sim$ 104000
Medium	151x91	7 μm	$\sim$ 133000
Fine	166x106	3.5 μm	$\sim$ 174000

The mesh investigations in the classical CFD sense were already carried out by Farkas et al. in [12] and [10] on the same configuration. The meshes were investigated in this work too, because the resolution of the CFD grid is usually not sufficient for acoustic coupling. Mesh refinement was applied only close to the trailing edge (the main acoustic source), which differs from the usual uniform method, because in the aerodynamic sense the mesh was already appropriate. The comparison was made based on the original Lighthill source term formulation only and the main parameters of the investigated meshes can be found in Table 1. The observations are the following: the difference in the results between the coarse and medium mesh is significant. The main acoustic source is not well resolved on the coarse grid. Further improvement is hardly noticeable between the medium and the fine mesh. Based on these results, the medium mesh is selected for further simulations.

3.2. **Reflection avoidance in compressible CFD simulations.** In CFX there is a beta option to turn on acoustic non-reflectivity at the boundaries but it works well only if the sound waves hit the boundary in the normal direction. (Non-reflective boundary conditions are implemented in most commercial codes based on the 1D wave equation [13].) If the perturbation velocity has also a tangential component at the boundaries, the non-reflective boundary condition can cause instabilities or reflect the acoustic waves [10]. Other passive possibilities to avoid reflections are to artificially increase the viscosity close to the boundaries or to stretch the grid there. These options are infeasible because of presence of the wall behind the cavity. Further possibilities are the active damping methods: implicit damping, explicit damping, artificial

convection and perfectly matched layer. With the exception of implicit damping these methods cannot be implemented in a commercial code like CFX. The explicit technique needs a writing access to the state vectors, which is prohibited in CFX, while the artificial convection and the perfectly matched layer method require changing the governing equations significantly, which is again not feasible in commercial software. Furthermore the perfectly matched layers technique is not developed for the Navier-Stokes equations, according to authors' knowledge. In our case the implicit damping method was implemented in CFX for the continuity equation. It can be achieved by the addition of the following source terms to the governing equations

$$S_C = -\sigma_1 \left(p - p_{mean}\right), \tag{3.1}$$

where S_C is the source terms of continuity equation, σ_1 is the amplitude function of the damping, p is the relative pressure, p_{mean} is the prescribed value at any given grid point, in our case it was 0 Pa.

In the next step σ_1 has to be specified and based on [14] we apply

$$\sigma_1 = \hat{\sigma}\left(\frac{x - x_0}{H_s - x_0}\right)^{\beta} \tag{3.2}$$

where $\hat{\sigma}$ depends only on non-geometrical variables and the other term provides the geometrical shape function, x is the running coordinate, x_0 is the location of the beginning of the sponge layer, H_s is the location of the end of the sponge layer, β is the shape parameter. β was chosen between 2 and 2.5 in [13], while in other papers it was 3 [15]. Here it was chosen to be 2, a similar formula can be used in the y (or in 3D simulation in the z) direction.

A new expression was derived for $\hat{\sigma}$ because no suggestion was found in literature to choose it. Let us write the equation of state of the ideal gas

$$\rho = \frac{p_{abs}}{\gamma R T}, \tag{3.3}$$

where ρ is the density, p_{abs} is the absolute pressure, γ is the specific heat ratio and R is the gas constant. Now we split the variables into mean and perturbation part while assuming constant temperature. It is trivial that the fluctuations of the relative and absolute pressure are the same because of constant difference.

$$(\bar{\rho} + \rho^{'}) = \frac{(\overline{p_{abs}} + p^{'})}{\gamma R T}. \tag{3.4}$$

The mean variables must satisfy the equation of state, thus they can be subtracted, which leads to

$$\rho^{'} = \frac{p^{'}}{\gamma R T}. \tag{3.5}$$

The mass flow rate per unit volume can be approximated as

$$\hat{\sigma} \propto \frac{\rho^{'}}{\Delta t}. \tag{3.6}$$

where Δt is the time needed for pressure fluctuation to propagate through one cell, i.e.

$$\Delta t = \frac{\Delta x}{v_{prop}}. \tag{3.7}$$

Here, Δx is the cell size in the direction of the propagation, v_{prop} is the propagation velocity of the pressure disturbance, which can be of various physical origin in a complex flow. The propagation velocity of the acoustic waves is the speed of sound but in the flow other pressure fluctuations exist: for example the instability waves along the shear layer or the propagating vortices after the cavity. The speed of these fluctuations is obviously much less than the acoustic speed so that v_{prop} must be chosen carefully. Finally, equations (3.5)-(3.7) lead to following expression:

$$\hat{\sigma} \propto \frac{p^{'}}{\gamma RT}\frac{v_{prop}}{\Delta x} = \frac{p^{'}}{c_0^2}\frac{v_{prop}}{\Delta x} = \frac{p^{'}}{c_0}\frac{Ma_{prop}}{\Delta x}\,, \tag{3.8}$$

where Ma_{prop} is the Mach number based on the propagation velocity. If $\hat{\sigma}$ is greater than the right-hand side of (3.8), the sponge layer is overdamped, causing stability problems. During the time the pressure fluctuation passes the cell, its value can have opposite sign and the magnitude can be larger than its value when it entered the cell. In the simulations, the following expression was used, based on (3.8)

$$\hat{\sigma} = C_1(Ma_{prop})\frac{p^{'}}{c_0}\frac{1}{\Delta x}\,, \tag{3.9}$$

where C_1 was the constant with which the sponge layer can be tuned. Its allowable maximal value is 1 in the case of pure acoustic waves (above the cavity), and it has to be decreased if other types of pressure fluctuations are present in the sponge layer (after the cavity).

3.3. **The results of CFD simulations.** Fast Fourier Transformation (FFT) was carried out on the pressure signals at the monitor point in the incompressible and the compressible simulations and the results can be seen in Figure 3. The peaks are practically the same. The fundamental frequency is 1522 Hz with the amplitude of 26.4 Pa (122.4 dB) in the incompressible simulation, while in the compressible simulation the fundamental frequency is 1530Hz and the amplitude was 26.9 Pa (122.6 dB). Although the pressure signal in the compressible simulation was a bit noisier, there was technically no difference between the two simulations. The compressibility of the fluid thus can be neglected, as expected.

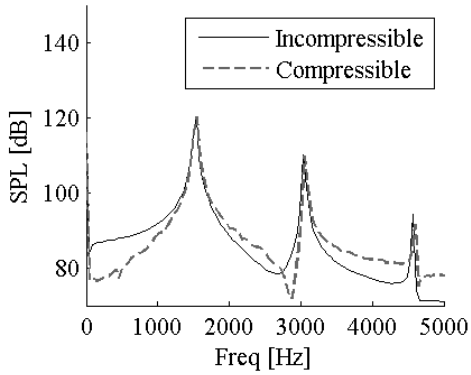

Figure 3. The FFT of the pressure signal at the monitor point

3.4. **The comparison of various source term formulations.** In the next step the sources were calculated for the acoustic simulation, based on the CFD results. The sources introduced in Section 2 are compared with each other. In the first investigation the source field based on the Lighthill tensor was compared to the Laplacian of the pressure in the incompressible case because the previously introduced pressure based formulations are valid only for incompressible flow simulations. The time signal compared inside the cavity can be seen in Figure 4. The monitoring point was placed in the shear layer at equal distances far from the edges of the cavity. To be precise, the monitoring point is at $x = L/2$, $y = 0$, where the origin is the leading edge and the x direction is the main flow direction.

In Figure 4 it can be clearly seen that the Laplacian of the pressure approximates well the second derivative of the Lighthill tensor but the signal was noisier in the case of the pressure-based-formulation. The reason for this phenomenon can be that the pressure values themselves suffer from higher numerical error, which is further magnified during the calculation of second spatial derivatives. It is difficult to interpret the results because of the lack of knowledge about how CFX calculates the pressure.

In the next step an FFT is performed on the various sources (Figure 5). Here, the spatial distributions (the shapes) of the sources were compared. The Laplacian of the pressure was excluded from the comparison because no significant difference could be observed between Laplacian of the pressure and the double divergence of the Lighthill tensor. Only a small difference was recognized in the compressible computations very close to the edge. The results of the comparison are summarized in Table 2 for the incompressible simulations. First, the effect of the mean value (F_{Mean}) of the acoustic load is investigated at a probe location close to the trailing edge in all cases. The zero frequency component was compared to the fundamental mode component (F_{1st}). It is probable that this value highly depends on the probe location but the tendencies can be roughly estimated based on the monitoring point. This ratio was high in the case of velocity-based source terms (Lighthill tensor, Lamb vector) and was low in

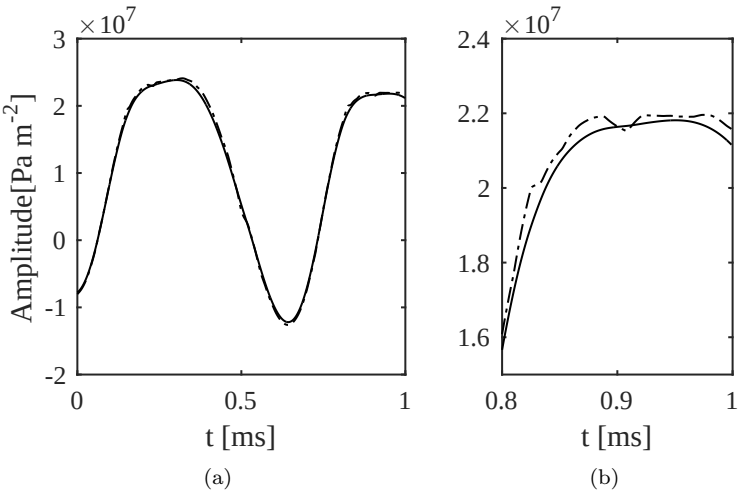

Figure 4. Comparison of the sources calculated based on the Lighthill-tensor (continuous line) and the Laplacian of the pressure (dashed line) in the middle of the shear layer

the case, when the source was calculated based on the time derivative of the pressure. The high mean value is non-acoustical (only the fluctuating part is considered to be acoustic) and should be eliminated by the application of filtering. In the next step the spatial distribution of the source field is investigated. Let us define the nominal size (A) of the acoustic source as the area, in which the acoustic source strength is larger than 1% of the maximum acoustic source strength. This investigation was performed for various ratios of 5%, 10%, 20% and for all cases the tendencies were the same. The nominal size of the acoustic load was the smallest in the case of the Lighthill tensor. In the case of Lamb vector formulation the source was larger both in size (A) (∼30 times) and magnitude (S_{max}, the maximal load) (∼2 times). This does not mean unambiguously that the usage of Lamb vector produces higher acoustic pressure in the far field, because the phase relationships also influence the final results. This observation could mean that the resolution of the source could be better in the case of Lamb vector formulation and it could be used more effectively on a coarser grid as well. In the case of time derivative of the pressure formulation the size of the acoustic source was much larger (3-4 orders of magnitude), while its magnitude was much smaller. Furthermore, it can be stated that the spatial distribution of the sources looked very similar in the compressible and incompressible simulations.

4. Acoustic simulation

4.1. **The acoustic simulation domain.** The significant advantage of the hybrid approach is that the acoustic simulation domain can be larger than the CFD domain.

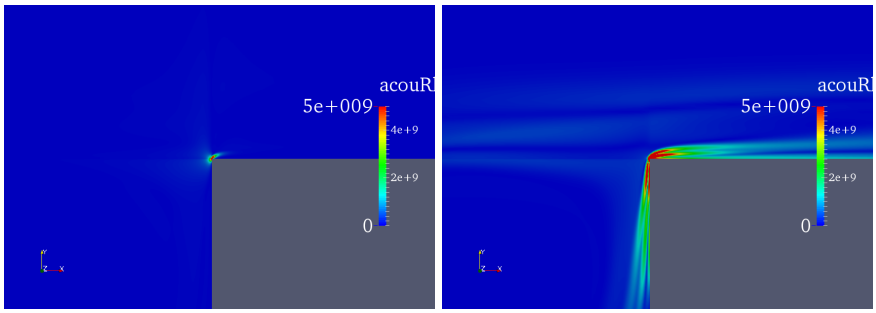

(a) (b)

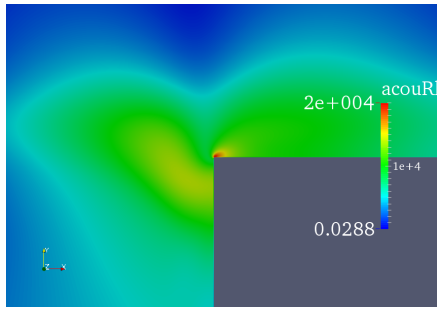

(c)

Figure 5. Spatial distribution of the acoustic source (Pa/m2) at the fundamental frequency. (a) divergence of the Lighthill tensor, (b) Lamb vector, (c) Second time derivative of the pressure

Table 3. Comparison of source terms defined in the incompressible flow field

Name	$\frac{F_{Mean}}{F_{1st}}$	A $[m^2]$	$S_{max}[Pa/m^2]$
Lighthill	~66 %	2.519e-8	5.6e10
Lamb	~133%	6.116e-7	1.5e11
Time derivative	<1 %	8.072e-4	2.1e4

The acoustic domain contains three parts in our case. The first one is a small source region where the sound is generated. Here, the acoustic sources were calculated based on the flow simulation data and interpolated to the acoustic source grid. In this case the two meshes (the CFD and acoustic mesh) were identical. The next part is the propagation region, where the acoustic waves propagate without any amplification or damping. Within this region, the right-hand side of the acoustic wave equation is zero. This region was defined as 1 m before, after and above the cavity. The grid size

here was much coarser (5 mm) and that is why an interpolation technique described in [16] was used at the border of two regions. The outermost part is the absorption region. This region was a thin layer at the border of simulation domain, where the waves were strongly damped to avoid reflections. Here the so-called perfectly matched layer was defined. Further information about the technique and implementation can be found in [17].

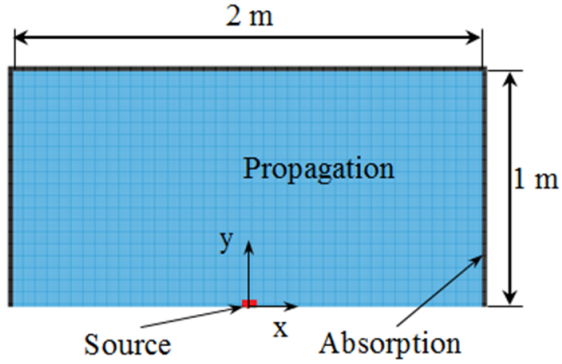

Figure 6. Parts of acoustic simulation domains: the source region, propagation and absorption region; and microphone positions

4.2. **The results of the acoustic simulation domain.** The acoustic simulations were carried out by CFS++, which is an in-house code at Vienna University of Technology to solve partial differential equations by the finite element method. First, the simulations based on the incompressible acoustic source formulations were carried out. A typical acoustic field of the simulation, which was calculated based on the Lighthill tensor, can be seen in Figure 7. The directivity pattern can be clearly associated to a dipole. At the same time the results provided by the second time derivative of the pressure show an absolutely different radiation pattern, as displayed in Figure 8.

Howe investigated extensively the cavity tone with the same length-depth ratio at low Mach numbers [18]. He calculated the acoustic field by Green functions. According to his result, the monopole characteristics of the sound appear only at higher frequencies and not at the fundamental frequency (which dominates in the time domain), if the Mach number is low. In Figure 9 the directivity patterns were plotted for different Strouhal numbers.

The monopole part of the sound source plays a significant role only if $\mathrm{St} \gtrsim 20$ and $\mathrm{Ma} = 0.01$, as well as for $\mathrm{St} \gtrsim 2$ and $\mathrm{Ma} = 0.1$ according to Howe. Pure dipole pattern was observed also in [19], where the sound field was calculated based on experimental data. The directivity pattern can indicate the validity of the source term formulations. FFT was performed in all cases on the whole acoustic pressure field (Figure 10). Good qualitative agreement can be seen with the results of Howe (Figure 9) in Figure 10.

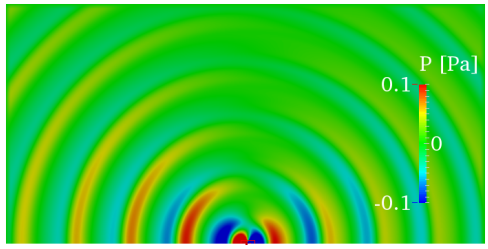

Figure 7. The instantaneous acoustic pressure field based on Lighthill analogy (incompressible)

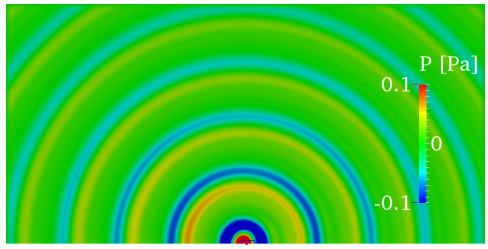

Figure 8. The instantaneous acoustic pressure field based on second time derivative of the pressure (incompressible)

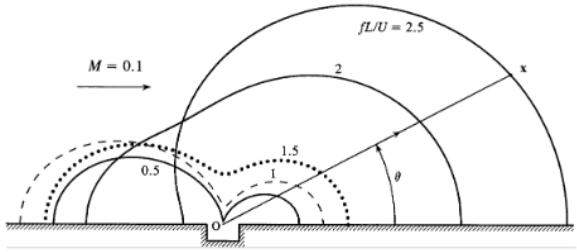

Figure 9. Directivity patterns at Ma=0.1 and St=0.5, 1, 1.5, 2,2.5 [18]

In Figure 11, the directivity is evaluated on a circle, with a radius $r = 0.4$ m around the trailing edge. It can be seen that the velocity-based analogies ("Lighthill tensor", "Lamb vector") reproduce a dipole radiation better than the pressure-based ones. In the cases when the sources are based on the Laplacian of the pressure or the second time derivative of the pressure, the directivity patterns were unrealistic if

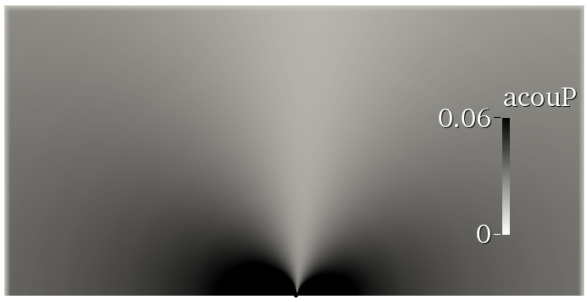

Figure 10. The FFT of the acoustic pressure field at the fundamental frequency based on Lighthill-analogy (incompressible).

we accept the correctness of the dipole pattern. The worst result was provided by the second time derivative of the pressure. In this case the sound pressure was low in upstream and downstream directions, while it was too strong above the cavity. In the case of Laplacian of the pressure, the results show the weak dipole characteristics superposed on monopole sound characteristics. Here, the amplitudes of the waves were in the correct range in both the upstream and downstream directions. The magnitudes differ slightly between its velocity-based results but this difference was negligible compared to previous cases.

The same investigation was performed on results based on sources calculated from the compressible flow simulation. The acoustic field is very similar to the incompressible cases except for the simulation based on the second time derivative of the pressure. Here a high-frequency noise appeared in the simulation. The radiation pattern looks like a dipole, while in the incompressible case it is a monopole. However, it has to be noted that the formulation is only valid for incompressible flows. It is noticeable that there are no visible differences in the source terms based on compressible and incompressible simulations (not shown here). After performing FFT on the results, the directivity patterns were also evaluated along the same circle as before.

In Figure 12, it can be seen that the results were similar to those for the incompressible cases. The main difference appeared in the pressure-based cases, which are not valid for compressible flow simulation. Here, the calculations based on the Laplacian of the pressure overpredict the sound pressure, as expected, because only the incompressible part of pressure fluctuation induces the acoustic field. At the same time the directivity pattern became more realistic in both pressure-based cases. The reason for this is unclear; maybe the different pressure computation techniques cause this huge difference, especially in the case of the time derivative of the pressure. The pressure signals at various microphone positions obtained for compressible and incompressible simulations were compared. In the case of the velocity-based formulations the differences were negligible, which was expected as these analogies are valid both in compressible and incompressible flows.

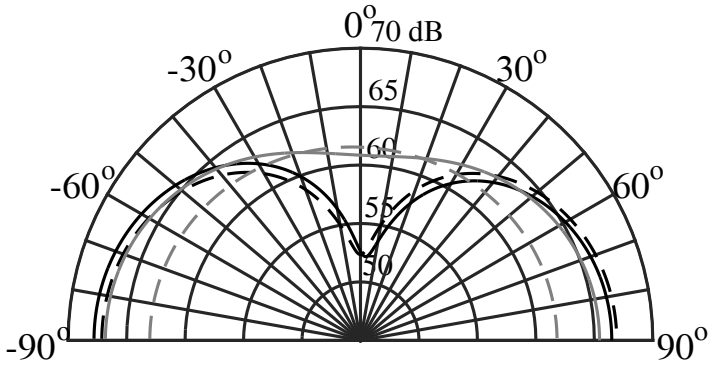

Figure 11. The directivity of the sound field at the fundamental frequency, sources are calculated based on incompressible data (black, cont.- Lighthill; black dashed - Lamb; grey, cont. - Laplacian of the pressure; grey, dashed - second time derivative of the pressure)

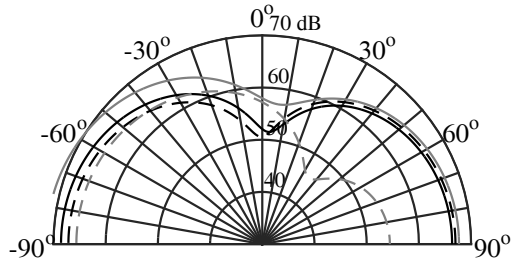

Figure 12. The directivity of the sound field at the fundamental frequency, sources are calculated based on compressible data (notation are the same as in Figure 11.)

5. Conclusions

In this paper various acoustic source term formulations were compared in the case of a rectangular cavity. Based on the results the following conclusions can be drawn. The velocity-based analogies provide better results than the pressure-based analogies

with respect to the directivity patterns. The Laplacian of the pressure calculation method provides good results in upstream and downstream directions but strongly overestimates the acoustic pressure over the cavity. At the same time, no significant difference was noticed close to the trailing edge during the source term investigation in Section 2 between the second divergence of the Lighthill tensor and the Laplacian of the pressure. The second time derivative of the pressure predicts only the sound pressure in the right order of magnitude. The directivity of the sound field is wrong and the method highly overestimates the sound pressure level at the higher harmonics. It must be mentioned that the mesh study was performed only for the Lighthill analogy-based formulation. The authors are sure that such a big difference cannot be caused by a poor resolution of the acoustic sources in the case of pressure-based sources. The acoustic sources were also calculated for the compressible medium. Here, only the velocity-based analogies are valid, which was confirmed by the results, in spite of the fact that the compressibility does not play a significant role. To summarize the results, the analogy based on the Lamb vector seems to be the best. It provided the finest spatial resolution of the source along the velocity-based analogies on a same mesh, while it provides similar results to the original analogy based on Lighthill tensor. The only drawback is that the mean value was high but this can be avoided by filtering.

References

1. Healy, G. J.: Measurements and analysis of aircraft far-field aerodynamic noise. *NASA, Contractor Rep. 2377*, 1974.
2. Rowley, C. W. and Williams, D. R.: Dynamics and control of high-Reynolds-number flow over open cavities. *Annual Review of Fluid Mechanics*, **38**, (2006), 251–276.
3. Yu, Y. H.: Measurements of sound radiation from cavities at subsonic speeds. *Journal of Aircraft*, **14**, (1977), 838–843.
4. Heller, H. H. and Dobrzynski, W. M.: Sound radiation by aircraft wheel well/landing gear configurations. *Journal of Aircraft*, **14**, (1977), 768–774.
5. Farkas, B., Paál, G., and Szabó, K. G.: Descriptive analysis of a mode transition of the flow over an open cavity. *Physics of Fluids*, **24**, (2012), Paper Number 027102.
6. Gloerfelt, X.: *'Cavity noise'. Chap. 0, VKI Lectures: Aerodynamic noise from wall-bounded flows.* Von Karman Institute, France, 2009.
7. Hüppe, A.: *Spectral Finite Elements for Acoustic Field Computation.* Shaker Verlag GmbH, Aachen, 2014.
8. Kaltenbacher, M.: *Numerical Simulation of Mechanic Sensors and Actuators: Finite Elements for Multiphysics.* 3rd edn., Springer, Berlin, 2015.
9. Lighthill, M. J.: On sound generated aerodynamically I. General thory. *Proceedings of the Royal Society of London*, **211**, (1951), 564–587.
10. Farkas, B. and Paál, G.: Numerical study on the flow over a simplified vehicle door gap - an old benchmark problem is revisited.
11. *ANSYS CFX Reference Guide Release 14.5.* U.S.A., 2012.

12. Farkas, B. and Paál, G.: *Computational investigation on the oscillation frequencies of the shear layer ove an open cavity.* Conference on Modelling Fluid Flow. The 14th International Conference on Fluid Flow Technologies, Budapest, Hungary, 2009.

13. Schönrock, O.: Numerical prediction of flow induced noise in free jets of high mach numbers. *Thesis of Doctor of Engineering Sciences*, University of Stuttgart, 2009.

14. Richards, S., Zhang, X., Chen, X., and Nelson, P.: The evaluation of non-reflecting boundary conditions for duct acoustic computation. *Journal of Sound and Vibration*, **270**(3), (2004), 539–557.

15. Ashcroft, G., Takeda, K., and Zhang, X.: A numerical investigation of the noise radiated by a turbulent flow over a cavity. *Journal of Sound and Vibration*, **265**(1), (2003), 43–60.

16. Triebenbacher, S., Kaltenbacher, M., Flemisch, B., and Wohlmuth, B.: Applications of the mortar finite element method in vibroacoustics and flow induced noise computations. *Acta Acustica united with Acustica*, **18**, (2010), 536–553.

17. Kaltenbacher, B., Kaltenbacher, M., and Sim, I.: A modified and stable version of a perfectly matched layer technique for the 3D second order wave equation in time domain with an application to aeroacoustics. *Journal of Computational Physics*, **235**, (2013), 407–422.

18. Howe, M. S.: *Wall-cavity aeroacoustics at low Mach number.* Tech. Rep. AM 04-001, Boston University, College of Engineering, 2004, URL `http://www.dtic.mil/dtic/tr/fulltext/u2/a419580.pdf`.

19. Koschatzky, V., Westerweel, J., and Boersma, B. J.: Comparison of two acoustic analogies applied to experimental piv data for cavity sound emission estimation. *16th AIAA/CEAS Aeroacoustic Conference*, 2010.

Journal of Computational and Applied Mechanics, Vol. 11., No. 2., (2016), pp. 197–209
DOI: 10.32973/jcam.2016.013

EFFECT OF FORCED CONVECTION HEAT TRANSFER OVER SIDE-BY-SIDE SQUARE CYLINDERS IN A STEADY CONFINED FLOW REGIME

Aniruddha Sanyal
Department of Chemical Engineering
Indian Institute of Technology Roorkee
Roorkee 247667, Uttarakhand, India
saniruddhaan@gmail.com

Amit Dhiman
Department of Chemical Engineering
Indian Institute of Technology Roorkee
Roorkee 247667, Uttarakhand, India
dhimuamit@rediffmail.com, amitdfch@iitr.ac.in

[Received: April 16, 2016, Accepted: August 12, 2016]

Abstract. A two-dimensional numerical study has been conducted to analyze forced convective confined flow and heat transfer from a pair of side-by-side square cylinders with a transverse gap ratio (defined as the ratio of the distance between the obstacles to the size of an obstacle) of 1.5. The flow is steady Newtonian in a viscous dominant flow field, investigated at Reynolds numbers (Re) ranging from 10 to 40 for Prandtl numbers (Pr) = 0.7 and 50. The present results are found to be in the excellent agreement with the literature, with a maximum deviation of 1.5%. It is observed from the streamlines that the wake formation increases with Re. The onset of flow separation was observed at $Re = 7$ and further a correlation connecting wake length with Re is stated.

Mathematical Subject Classification: 05C38, 15A15
Keywords: Drag coefficient, Nusselt number, side-by-side configuration, square bluff bodies, wake length

1. Nomenclature

β	[-]	ratio of the side of one square cylinder to the channel height (called here blockage ratio),
ρ	[kg/m^3]	fluid density,
μ	[Pa s]	viscosity of the fluid,
τ	[Pa]	shear stress,
C_D	[-]	drag coefficient,
C_p	[-]	pressure coefficient,
F_D	[N/m]	drag force per unit length of the obstacle,
H	[m]	transverse height of the domain,

L_r	[-]	recirculation length per unit length of the obstacle,
Nu	[-]	average Nusselt number,
Pr	[-]	Prandtl number,
Re	[-]	Reynolds number,
S	[m^2]	surface area,
T	[-]	temperature,
U_{max}	[m/s]	maximum velocity at the inlet,
V	[-]	dimensionless velocity,
X	[-]	distance between the obstacle boundary and inlet or outlet per unit size of the obstacle,
c_p	[J/kg K]	specific heat capacity of the fluid,
d	[m]	side length of a square cylinder,
h	[W/m^2 K]	heat transfer coefficient,
k	[W/m K]	thermal conductivity of the fluid,
n	[-]	direction vector normal to the plane,
p	[-]	pressure,
s	[m]	gap between the two square cylinders,
t	[-]	time,
x, y	[-]	position of flow parameters in the domain.

Subscripts and superscripts

d	downstream,
u	upstream,
S	control surface,
x	direction of vectors along horizontal axis,
y	direction of vectors along vertical axis.

2. Introduction

Ever since the inception of study for fluid flow and heat transfer past a bluff body in a confined domain, decades have passed for research mainly on an experimental basis, which has incurred huge cost. As a result several attempts have been made to analyze this process through numerical modeling and simulation. Modern numerical methodologies like finite volume method (FVM), lattice Boltzmann method (LBM), optical density method, etc. have profound applications in decoding the sets of complicated partial differential equations which define the flow and heat transfer processes. This field has heavy application in process heat transfer equipment, structural dynamics and mechanical, chemical and other related engineering applications.

When two or more bluff bodies are placed in proximity, the intricacy in predicting momentum and heat transfer around it is aggravated and interference effects are severe. As a result, the flow and thermal patterns differ from those of a single circular cylinder.

Valencia and Paredes [1] performed a numerical study to examine the flow and heat transport characteristics in a plane channel with two square cylinders (or square bars) placed side-by-side to the impending flow for a transverse gap ratio (s/d) ranging from

0 to 5 for Reynolds number Re varying from 25 to 125 at a constant blockage ratio β of 12.5%. The mathematical outcomes divulge the complicated formation of the flow. The flow remains steady at $Re = 200$; whereas, periodicity or unsteadiness is observed as the Re is further increased. Peng [2] studied the fluid flow past two side-by-side square bluff bodies with a constant gap ratio of 2 in an unconfined domain by both mathematical simulation as well as investigational flow-visualization methods at $Re = 100$. Bi-stable flows were observed, with both in-phase and anti-phase synchronized patterns, as a result of adjusting the initial conditions. Agrawal et al. [3] examined the flow over two side-by-side square cylinders using the LBM, identified regimes with both synchronized and scattered vortex formation, and determined the type of vortex shed from the square cylinder in either regime for a uniform flow field at the upstream. Numerical outcomes for two gap ratios of 0.7 and 2.5 for the fixed $Re = 73$ and blockage of 5.55% had been reported. Later, Rao et al. [4] carried out an extension work of Agrawal et al. [3] and performed a quantitative study of the flow over two side-by-side square bluff bodies, for transverse gap ratio varying from 1 to 2.7 and Re varying from 73 to 200 at the blockage of 5.55%. They revealed that for a transverse gap ratio lesser than 1.5, the flow demonstrates a flip-flop behavior known as chaotic; however, for s/d greater than 1.5, the flow tends to synchronize, known as quasi-periodic and for $s/d > 4$ synchronized flow was observed. The transition between chaotic and quasi-periodic regimes occurs at $s/d = 1.5$. Durga Prasad and Dhiman [5] analyzed the steady and unsteady laminar flow and heat transfer in a confined domain for a pair of side-by-side square cylinders for $Re = 10$ to 100 at $Pr = 0.7$ to 50 with the gap ratio from 1.5 to 10 in a transverse domain height of $18d$ [3, 4]. It was shown that the overall drag coefficient decreases with increasing Re and Pr for all values of gap ratios. The enhancement in average Nusselt number was found more than 76% for the range of settings covered. They also found the occurrences of in-phase and anti-phase flow past the square cylinders at various Re. They also found that beyond a gap ratio of 2.5 the steadiness in flow was observed till $Re < 60$ which was limited to $Re = 50$ for a smaller gap ratio.

Furthermore, sufficient information is now available in the literature on the flow around two side-by-side square cylinders in the turbulent regime. For instance, Wong et al. [6], Kolar et al. [7] and Alam et al. [8] executed experimental investigation of the wake formation around a pair of side-by-side square cylinders. Harichandan and Roy [9] displayed the strong dependence of flow characteristics on the transverse gap ratio and Re, with the former being more dominant than the latter.

Mizushima and Akinaga [10] studied wake interactions in the flow past a row of square bars by both numerical replication and experimental determination on the postulation that the flow is two-dimensional ($2D$), incompressible. Kumar et al. [11] reported the presence of synchronous, quasi-periodic, and chaotic flow regimes for s/d ranging from 0.3 to 12 for nine square cylinders in side-by-side arrangement at $Re = 80$. Along the same line, Sewatkar et al. [12] determined the effects of transverse gap ratio and Re on the flow around a row of cylinders for Re ranging from 30 to 140 and s/d 1 to 4. Chatterjee et al. [13] executed numerical simulation for the flow

around a row of five square bluff bodies kept at a side-by-side display for transverse gap ratios of 1.2, 2, 3, and 4 at $Re = 150$.

Thus, from the foregoing argument, one can summarize that no work is available on the onset of flow separation and the wake length at varying s/d in the confined flow around two side-by-side square cylinders in a cross flowing domain. Because the multiple bluff obstacles create a complex flow and thermal structures even at low Reynolds numbers, and owing to the engineering relevance in various applications (compact heat exchangers, plate type heat exchangers, etc.); the analysis of flow and thermal prototype is necessary. A close look at momentum and heat transfer processes in a highly viscous force dominated steady laminar flow regime ($10 = Re = 40$) inside a confined domain has been attempted. It is also seen that very few papers have mentioned the occurrence of a recirculation zone quantitatively. Hence, an attempt has been made to study recirculation length from the flow field and domain parameters $Re = 10$ to 40, $Pr = 0.7$, 50 and $s/d = 1.5$.

3. Mathematical formulation and solution methodology

Any flow problem involves sets of partial differential equations which need to be solved using some numerical techniques. The sequence of approaching the solution methodology involves initial statement of the problem followed by mention of the governing equations coupled with its boundary conditions. Further, generation of an optimal grid is solved here using ANSYS FLUENT. The basics regarding these topics are well explained in Chabra and Richardson [14].

3.1. **Problem statement.** The following problem has been assumed to be a simplified case of the flow of a fluid past a pair of square cylinders in a $2D$ domain.

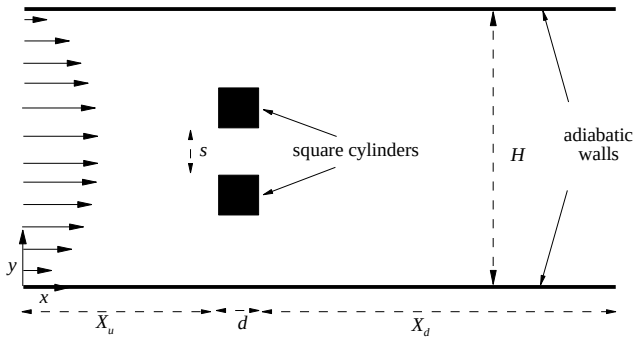

Figure 1. Schematic diagram for fluid flowing past side-by-side square cylinders

Here, the square cylinders are assumed to be infinitely long and perpendicular to the main flow. The variation of physical process parameters along this direction is zero till Re about 150. Following Durga Prasad and Dhiman [5], the domain has been set in a standardized format, where the upstream distance from the square cylinders, X_u is set at 8.5 and downstream distance, X_d as 16.5. The side length of the square cylinder, d is set as unity. The transverse gap ratio, s/d, is taken as 1.5.

Figure 1 aptly depicts the aforesaid problem statement. The $2D$ approximation is well established in a highly viscous force dominant flow field along with a small thermal gradient which is significant enough to catch the change in flow and thermal patterns due to flow around a pair of side-by-side square cylinders with good numerical accuracy.

3.2. **Governing equations.** For a $2D$ convective laminar flow, the corresponding dimensionless equations are:

Continuity equation for incompressible fluid flow

$$\frac{\partial V_x}{\partial x} + \frac{\partial V_y}{\partial y} = 0\,. \tag{1}$$

Momentum equations neglecting the body forces

$$\frac{\partial V_x}{\partial t} + \frac{\partial V_x V_x}{\partial x} + \frac{\partial V_y V_x}{\partial y} = -\frac{\partial p}{\partial x} + \frac{\partial 1}{Re}\left(\frac{\partial^2 V_x}{\partial x^2} + \frac{\partial^2 V_x}{\partial y^2}\right)\,, \tag{2}$$

$$\frac{\partial V_y}{\partial t} + \frac{\partial V_x V_y}{\partial x} + \frac{\partial V_y V_y}{\partial y} = -\frac{\partial p}{\partial y} + \frac{\partial 1}{Re}\left(\frac{\partial^2 V_y}{\partial x^2} + \frac{\partial^2 V_y}{\partial y^2}\right)\,. \tag{3}$$

Energy equation neglecting viscous dissipation and considering a pure forced convection heat transfer process

$$\frac{\partial T}{\partial t} + \frac{\partial V_x T}{\partial x} + \frac{\partial V_y T}{\partial y} = \frac{\partial 1}{Re\,Pr}\left(\frac{\partial^2 T}{\partial x^2} + \frac{\partial^2 T}{\partial y^2}\right)\,. \tag{4}$$

Further

$$Re = \rho U_{\max} d/\mu \quad \text{and} \quad Pr = c_p \mu / k\,. \tag{5}$$

3.3. **Boundary conditions.** At inlet: for a parabolic velocity inlet:

$$\begin{aligned} &V_x = 1 - (|1 - 2\beta y|)^2 \;\; (\text{for } \; 0 \le y \le H/d, \;\; \beta = d/H),\\ &v_x = 0, \qquad T = 0\,. \end{aligned} \tag{6}$$

On the surface of the square cylinders, the standard no-slip and constant wall temperature conditions are used:

$$V_x = 0, \qquad V_y = 0, \qquad T = 1\,. \tag{7}$$

On the upper and lower boundaries, the standard no-slip and adiabatic conditions are used:

$$V_x = 0, \qquad V_y = 0, \qquad \frac{\partial T}{\partial y} = 0\,. \tag{8}$$

At the exit boundary

$$\frac{\partial \phi}{\partial x} = 0 \tag{9}$$

where ϕ is a dependent variable, V_x, V_y or T.

The output parameters are summarized as follows:
Total drag coefficient, as explained by Patnana et al. [15] for the flow around a circular cylinder, in a horizontal cross flowing domain is as follows:

$$C_D = \frac{F_D}{\frac{1}{2}\rho U_{\max}^2 d} = \int_S C_p \, n_x \, \mathrm{d}S + \frac{2}{Re} \int_S \tau n_x \mathrm{d}S \tag{10}$$

Average Nusselt number:

$$Nu = \frac{hd}{k} \, . \tag{11}$$

3.4. **Grid generation and solution technique.** Figures 2a and 2b display the overall grid structure and close view of the grid structure around the square bluff bodies, respectively. The grid, using quadrilateral cells, generated for this problem is non-staggered in nature. It is generated using the commercial grid generation tool ANSYS Workbench. A finer grid size is maintained near the square cylinders to capture the changes that occur in the flow around the square cylinders. The smallest grid spacing is kept around the square cylinders and confined walls is of $0.008d$, and the coarsest one is $0.5d$ which can be seen at the inlet or outlet part of the flowing domain. The number of grid points placed on each surface of the square cylinders are 100, following Durga Prasad and Dhiman [5]. The meshing procedure in the zone connecting the square cylinders and the confined walls is done in a manner which can take into account the wall effects in flow process.

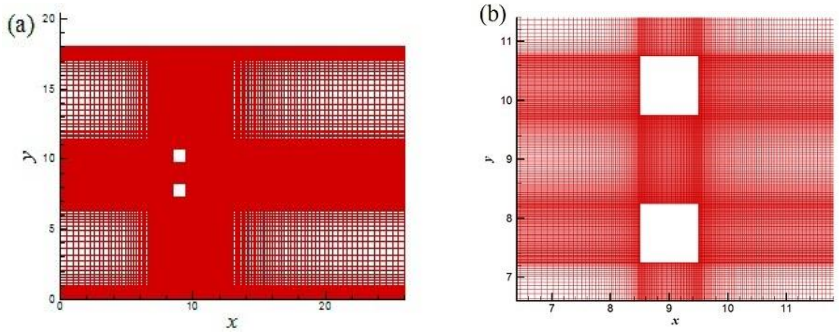

Figure 2. (a) The overall grid structure and (b) close view of the grid structure around the square bluff bodies

Following several books [16, 17], SIMPLE algorithm is used to avoid pressure velocity decoupling and because it offers good convergence for the type of problem under consideration. The absolute convergence criteria is set at 10^{-15} for flow parameters and 10^{-20} for thermal parameters. Discretization of the convective terms in the momentum and energy equations is done using QUICK, a third-order upwind scheme.

4. Results and discussion

4.1. **Validation.** The validation of the results obtained applying the above numerical method was carried out against those of Durga Prasad and Dhiman [5] for the Re ranging from 10 to 40 at $Pr = 0.7$ (resembling air) and 50 (resembling organic polymer liquids) for a constant transverse gap ratio of 1.5. Tables 1 and 2 show that the values of drag coefficient and Nusselt number stay well within 0.1% and 3.2%, respectively.

Table 1. Validation of C_D with [5] in a steady laminar flow regime

Re ($s/d = 1.5$)	C_D from Durga Prasad and Dhiman [5]	C_D from current simulation	% deviation
10	3.6034	3.6039	0.02
20	2.6151	2.6153	0.01
30	2.2001	2.1998	0.01
40	1.9646	1.9628	0.09

Table 2. Validation of Nusselt number with [5] in a steady laminar flow regime

Re ($s/d = 1.5$)	Nu from Durga Prasad and Dhiman [5]	Nu from current simulation	% deviation
$Pr = 0.7$			
10	1.4856	1.4918	0.42
20	2.0726	2.0913	0.90
30	2.4446	2.4713	1.09
40	2.7402	2.7749	1.26
$Pr = 50$			
10	6.0861	6.1320	0.75
20	8.4173	8.5673	1.78
30	10.2586	10.4862	2.22
40	11.6463	12.0215	3.20

It was seen that the drag coefficient remained the same for both square cylinders because of the fact that the effect of gravity and the variation of the fluid's density with temperature have been neglected in this problem. The C_D values reported above are those of the upper square cylinder in the flow domain. It is also to be noted that the average Nusselt number for both upper and lower square cylinders remains constant owing to similar reasons.

4.2. **Fluid flow patterns.** Figure 3 shows the streamlines at $s/d = 1.5$ for $Re = 20$ and 40. The flow is found to be steady in this flow range and at the same time an anti-phase pattern (wake structures generated from both square cylinders are equal

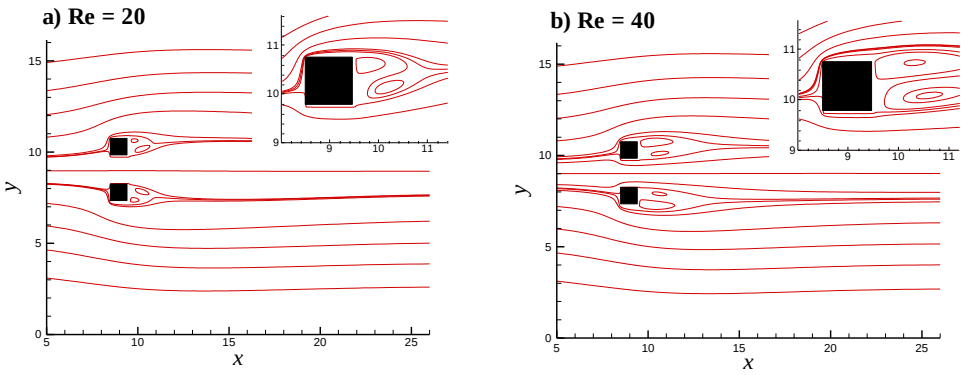

Figure 3. (a-b) Streamlines along with the magnified views of upper square cylinder for a transverse gap ratio of 1.5

and oppositely directed in a given plane) is seen. This pattern gradually glorifies as Re is increased from 20 to 40, which clearly depicts the approaching unsteadiness in the downstream.

A close look at the magnified image of the streamline contours reveals the formation of wakes at the rear part of the square bluff bodies, which widen with increasing Re. Further, it is to be noted that there is no possibility of reverse flow in the domain. These streamlines also show a marginal interference of stream functions due to the presence of two square bluff bodies. The transverse gap ratio falls under that needed to produce a quasi-periodic flow regime in accordance with results from previous studies [11].

4.3. **Thermal patterns.** Figure 4 shows the isotherm contours of the fluid flowing past the pair of side-by-side square bluff bodies at $Re = 20$ and 40 for the $Pr = 0.7$ and 50. Following Merkin [18], who stated that during the flow process, cooling a cylinder brings about separation near the stagnation point, this is also evident in this case by the clusters of isotherms accumulating in front of the frontal surface of the square bluff bodies. Despite the fact that the domain and flow structures are different from Merkin [18], the concept of high heat transfer in the front part of the obstacle stays intact irrespective of domain. In terms of magnitude factor, the results will always vary with configurations. The observation of the above pattern remains the same in all the cases in the direction of flow. This eventually leads to an increased Nusselt number (heat transfer rate) at the front surfaces compared to that of other surfaces. In fact one can also conclude that the heat transfer is maximum in the front surface followed by an intermediate degree on surfaces parallel to the flow and the rear face has the lowest heat transfer rate. The isotherms also seem to be steady and symmetric along the centerline with almost no interaction at $Pr = 50$, but the interaction prevails at $Pr = 0.7$. This factor can be explained from the concept of boundary layer

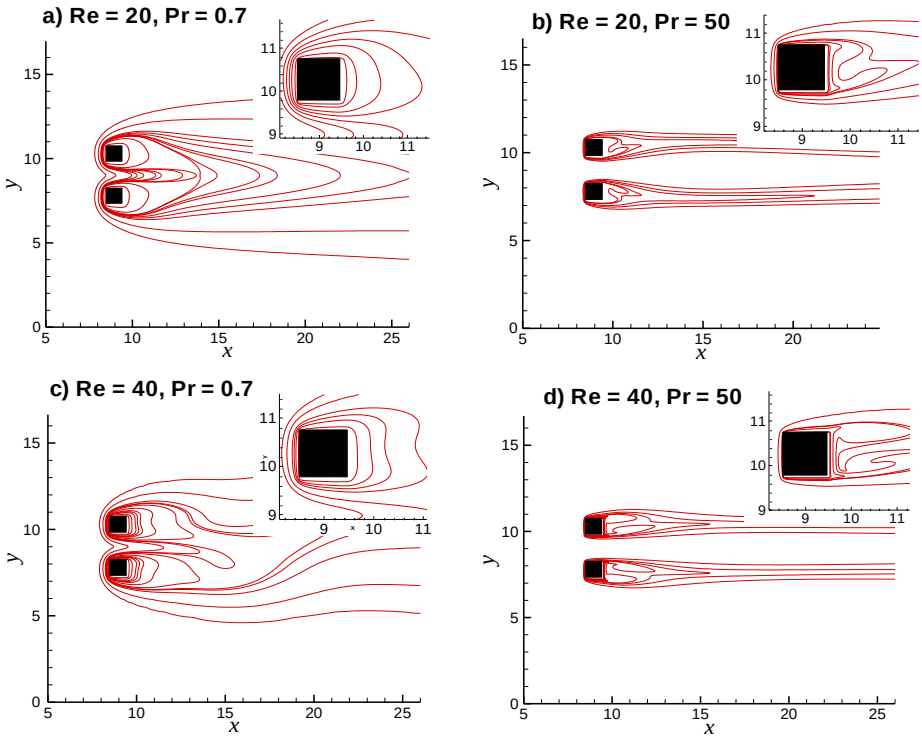

Figure 4. Isotherms along with the magnified views of upper square cylinder for a transverse gap ratio of 1.5

theory, where $Pr = 0.7$ indicates that the hydrodynamic boundary layer is smaller than the thermal boundary layer, which means that the layers tend to move outward which in turn leads to interaction of isotherms due to the presence of the two square cylinders. But at $Pr = 50$, the thermal boundary layer is smaller than that of its hydrodynamic counterpart, as a result, the isotherms tend to die down at a close distance in the downstream from the rear surface of the square cylinders.

The magnified views of the isothermal contours also demonstrates that the wakes formed at $Re = 20$ gradually increase in size at $Re = 40$. These figures also explain clustering of isotherms near the rear surfaces of the square cylinders, which increases with increasing Reynolds and Prandtl numbers.

4.4. **Recirculation length.** This is the distance from the rear surface of the obstacle to the point of attachment for the near closed streamline on the axis of symmetry. Figure 5 shows that the recirculation length varies linearly with increasing Re (Table 3). It increases with Re and the results fit linearly with a mere 0.001% deviation.

Table 3. Variation of recirculation length with Reynolds number

Re	Lr
10	0.4276
20	1.0039
30	1.6146
40	2.2406

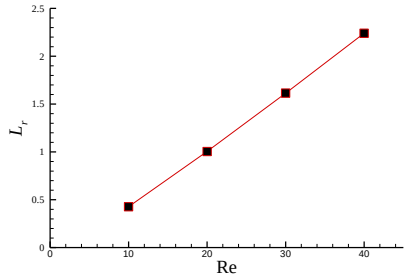

Figure 5. Variation of recirculation length with Reynolds number

The following simple correlation is established for the calculation of wake length (L_r), for the intermediate values of physical parameters in the steady confined regime:

$$L_r = 0.06Re - 0.19 \qquad \text{for} 10 \leq Re \leq 40 \tag{12}$$

This linearity in recirculation length versus Re plot has also been observed by Sharma et al. [19] for a single square cylinder.

Further, the variation in recirculation length with the change in transverse gap ratio was studied with s/d varying from 0.7 to 10 for $Re = 40$. The recirculation length is expected to be quite pronounced as compared to the lesser Re values, and at the same time to maintain the steadiness in the flow. The trends observed from Table 4 show that the recirculation length increases initially with increase in s/d to a maximum value beyond which the value decreases with the increase in s/d. Small gap ratio involves chaotic interactions of wake generated from both square cylinders, thereby reducing the wake length but as the transverse gap ratio increases the wake formations are subjected to minimum hindrance from the other body. But with further increase in s/d, a decrease in wake length is observed, which accounts for a hindrance evolving out of the confined walls.

Table 4. Variation of recirculation length with transverse gap ratio (s/d) at $Re = 40$

s/d	L_r (at $Re = 40$)
0.7	1.3083
1.5	2.2406
2.5	2.2035
5.0	2.1983
10.0	1.4395

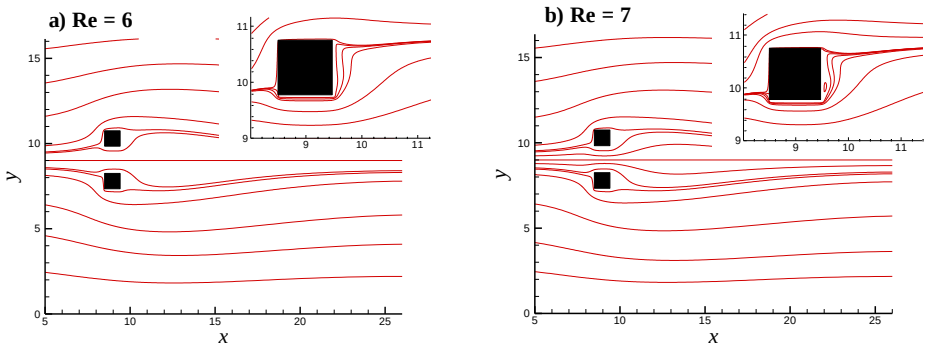

Figure 6. Streamlines along with magnified view of upper square cylinder showing absence of any wake at $Re = 6$ and the onset of wake formation at $Re = 7$

Furthermore, the onset of the flow separation is determined. It has been observed that there is no presence of recirculation wake at Re = 6, whereas recirculation commences at Re = 7 (as shown in Figures 6a and 6b, respectively). Hence, one can infer that a higher the magnitude of viscous dominance in the flow field, the lower or minimal is the recirculation or wake length formed at the rear side of the square cylinders.

5. Conclusions

Summarizing the present study, one can make the observation that the drag coefficient increases with the increase in Re, whereas Nu increases with the increase in both Re and Pr as is evident from the stream function and isothermal contours. It has also been seen that the recirculation length increases linearly with the increase in Re in steady laminar flow regime ($Re = 10$ to 40). This paves a way for further determination of recirculation length for various flow regimes for the flow over a pair of side-by-side square cylinders. One can also correlate the results with that their cylindrical counterpart thereby leading to the appropriate justification of choice of obstacle shape during various industrial operations. The effect of s/d on L_r is determined and the L_r correlation with respect to varying Re has been identified. Finally, the onset of flow separation is determined for the current framework and it occurs at $Re = 7$.

Acknowledgement. We thank editors and reviewers for their valuable comments that greatly improved the manuscript.

References

1. Valencia, A. and Paredes, R.: Laminar flow and heat transfer in confined channel flow past square bars arranged side-by-side. *Heat and Mass Transfer*, **39**, (2003), 721–728.

2. Peng, Y. F.: On the bi-stabilities of vortex shedding flows behind a pair of square solids. *Journal of Chinese Institute Engineers*, **27**, (2004), 385–393.

3. Agrawal, A. Djenidi, L. and Antonia, R. A.: Investigation of flow around a pair of side-by-side square cylinders using the lattice Boltzmann method. *Computers and Fluids*, **35**, (2006), 1093–1107.

4. Rao, Y. Ni, Y. and Liu, C.: Flow effect around two square cylinders arranged side-by-side using lattice Boltzmann method. *International Journal of Modern Physics C*, **19**, (2008), 1683–1694.

5. Durga Prasad, A. V. V. S. and Dhiman, A. K.: CFD analysis of momentum and heat transfer around a pair of square cylinders in side-by-side arrangement. *Heat Transfer Engineering*, **35**, (2014), 398-411.

6. Wong, P. T. Y., Ko, N. W. M. and Chiu, A. Y. W.: Flow characteristics around two parallel adjacent square cylinders of different sizes. *Journal of Wind Engineering and Industrial Aerodynamics*, **54/55**, (1995), 263–275.

7. Kolar, V., Lyn, D. A. and Rodi, W.: Ensemble-averaged measurements in the turbulent near wake of two side-by-side square cylinders. *Journal of Fluid Mechanics*, **346**, (1997), 201–237.

8. Alam, M. M., Zhou, Y. and Wang, X. W.: The wake of two side-by-side square cylinders. *Journal of Fluid Mechanics*, **669**, (2011), 432–471.

9. Harichandan, A. B. and Roy, A.: 2012, Numerical investigation of flow past single and tandem cylindrical bodies in the vicinity of a plane wall. *Journal of Fluids and Structures*, **33**, (2012), 19–43.

10. Mizushima, J. and Akinaga, T.: Vortex shedding from a row of square bars. *Fluid Dynamics Research*, **32**, (2003), 179–191.

11. Kumar, S. R., Sharma, A. and Agrawal, A.: Simulation of flow around a row of square cylinders. *Journal of Fluid Mechanics*, **606**, (2008), 369–397.

12. Sewatkar, C. M., Sharma, A. and Agrawal, A.: On the effect of Reynolds number for flow around a row of square cylinders. *Physics of Fluids*, **21**, (2009), 0836021–08360213.

13. Chatterjee, D., Biswas, G. and Amiroudine, S.: Numerical simulation of flow past row of square cylinders for various separation ratios. *Computers and Fluids*, **39**, (2010), 49–59.

14. Chhabra, R. P. and Richardson, J. F.: Co-current horizontal and vertical upwards flow of gas and non-Newtonian liquid, *Encyclopedia of Fluid Mechanics*, Vol. 3, Edited by N. P. Cheremisinoff, Gulf, Houston (USA), (1986), 563-609.

15. Patnana, V. K., Bharti, R. P. and Chhabra, R. P.: Two-dimensional unsteady flow of power-law fluids over a cylinder. *Chemical Engineering Science*, **64**, (2009), 2978-2999.

16. Muralidharan, K. and Sundararajan, T.: *Computational Fluid Flow and Heat Transfer*. 2nd edition, Narosa publications, 2000.

17. Anderson, J. D. Jr.: *Computational Fluid Dynamics - the Basics with Applications*. 2nd edition, McGraw Hill publication, 2000.

18. Merkin, J. H.: Mixed convection from a horizontal circular cylinder. *International Journal of Heat and Mass Transfer*, **20**, (1977), 73–77.

19. Sharma, N. Dhiman, A. K. and Kumar, S.: Mixed Convection flow and heat transfer across a square cylinder under the influence of aiding buoyancy at low Reynolds numbers. *International Journal of Heat and Mass Transfer*, **55**, (2012), 2601–2614.

Journal of Computational and Applied Mechanics, Vol. 11., No. 2., (2016), pp. 211–225
DOI: 10.32973/jcam.2016.014

NUMERICAL SIMULATION OF TURBULENT TRANSITIONAL FLOW AROUND AN ELASTICALLY SUPPORTED AEROFOIL

Petr Sváček
Czech Technical University in Prague, Faculty of Mechanical Engineering,
Dep. of Technical Mathematics, Karlovo nám. 13, 121 35 Praha 2, Czech Republic
petr.svacek@fs.cvut.cz

[Received: March 31, 2016, Accepted: July 12, 2016]

Abstract. In this paper the numerical simulation of the interaction of fluid flow with a flexibly supported aerofoil is addressed. Particularly, the turbulent flow model with a laminar-turbulence transition is considered. The transitional model is based on the two equation $k-\omega$ turbulence model, where the additional two equations for the intermittency and transitional onset Reynolds number are included. The motion of the computational domain is treated with the aid of the arbitrary Lagrangian-Eulerian method. The attention is paid mainly to the numerical approximation of the complex nonlinear coupled problem. The numerical results are shown for aeroelastic response of the aerofoil.

Mathematical Subject Classification:
Keywords: turbulence models, transition, finite element method, aeroelasticity

1. Introduction

Numerical approximation of fluid-structure interaction (FSI) problems has recently become important in many technical applications in turbomachinery, aerospace engineering, biomechanics. In technical practice particularly the prediction of aeroelastic instability as flutter is important [2]. The aeroelastic instability region is usually treated with the aid of a linearized approach [1]. Such an approach can provide necessary conditions to guarantee safety, but the transient growth induced by external excitation can lead to structural failure even though the system is aeroelastically stable, see [3]. The problem of transient aeroelastic response was addressed in [4], where the combined aeroelastic behaviour and gust response of a flexible aerofoil was explored theoretically. In [5] the FSI problem of gust response of a flexible typical section was investigated in terms of both high- and low-fidelity simulations. The use of accurate aeroelastic simulations is particularly attractive because it reduces the development risk, the number of experiments and the possible design modifications. However, computational efforts associated with high fidelity aeroelastic models currently precludes their direct use in industry [6]. Acceleration of time-accurate high fidelity aeroelastic simulation algorithms has therefore become an active area of research. The most common solution strategy is the so-called partitioned approach,

which de-couples the original FSI problem and uses specialized solvers for each sub-problem (see [7]). The coupling is then enforced at the fluid-solid interface by suitable interface conditions.

The other thing is that for approximation of FSI problem the applied numerical method should be able to treat the moving domain/meshes. The most popular method is the Arbitrary Lagrangian-Eulerian (ALE) method, see [8]. There are several possibilities how to apply the finite element method (FEM) [9]. Usually in order to provide higher order accuracy or stability some additional assumptions on the ALE are required, see [10]. Particularly the so-called geometrical conservation law is important [11].

Moreover, in order to apply the FEM for numerical simulation of incompressible flow problem must overcome several sources of instability. One instability is caused by the incompatibility of the pressure and velocity pairs of finite elements, cf. [12]. The other instability is due to the dominating convection terms, see [13]. There is another less well-studied instability source in the Galerkin discretization method related to a possible poor resolution of pressure, see [14], [15], [16].

The numerical simulation of interactions of flow with vibrating aerofoil was considered in [17]. Nevertheless the FSI problems usually include high Reynolds number flows, where the turbulence effects need to be included [18]. In [19] the interaction of a three degrees of freedom (DOF) airfoil was addressed with the turbulent flow modeled by the Reynolds averaged Navier-Stokes (RANS) equations combined with Spalart-Allmaras or $k-\omega$ turbulence models. The flow was also modelled by the RANS equations combined with the $k-\omega$ turbulence model in the paper [20], where the developed in-house FEM code was applied to the numerical simulation of the aeroelastic interaction of flexibly supported 2-DOF aerofoil with the 2D incompressible viscous turbulent flow subjected to a sudden gust. The developed method was successfully tested comparing the results with the study published in [4], [21], where the aerofoil response to the gust was computed by a commercial CFD program code.

The same FSI problem was studied in [22], where the aeroelastic aerofoil response to the gust computed for the turbulent airflow was compared with the laminar flow. In this case, the appearance of the flow separation can significantly influence the aeroelastic response. The application of the turbulent model on the other hand consider the boundary layer to be turbulent on the whole surface of the aerofoil. In reality the transition from laminar to turbulent flow exists on the surface of the aerofoil. The transition in technical applications can be modeled with the aid of different approaches, see [23], [24]. One class of these models is based on the use of an equation for the intermittency coefficient [25]. For this equation usually empirical correlations need to be involved with application of some non-local operations (as determination of the boundary layer thickness). The use of these operations is usually computationally expensive on non-structured grids. In order to get rid of these non-local operations another approach was proposed in [26] and also [27]. Here, the intermittency equation is coupled to the additional modeled variable and onset criteria are then related to this new local variable.

Although there are numerous publications devoted to the transitional model, there are not as many papers interested in the numerical simulation of FSI problems with transitional model included. In [28] the unsteady transitional flow over an oscillating NACA 0012 aerofoil was numerically investigated, showing that the transition from laminar to turbulent state and relaminarization occur widely in time and in space. In [29] the 2 DOF bending/torsion flutter characteristics of the NLR 7301 section was numerically investigated and the natural transition was modelled. In [30] low amplitude self-sustained pitch oscillations in the transitional Reynolds number regime are studied numerically showing the importance of the laminar separation of the boundary layer near the trailing edge for initiating and sustaining the pitching oscillations. In [31] the effect of freestream turbulence on small-amplitude limit-cycle oscillations of an aerofoil is investigated with the aid of a correlation-based transitional model.

In the present paper Menter's transitional turbulence model is described and applied for numerical simulation of 2D viscous incompressible flow past a flexibly supported aerofoil. First, the mathematical model of the considered problem is described and its numerical approximation is shortly explained. Further, the applicability of the method is shown on a benchmark problem.

2. Mathematical Description

2.1. **Flow model.** The mathematical formulation of the problem consists of the flow model, the structure model and the interface conditions. We consider the two-dimensional time dependent computational domain $\Omega_t \subset \mathbb{R}^2$ with the Lipschitz continuous boundary $\partial\Omega_t$, see Figure 1. The fluid motion in the domain Ω_t is modeled using the Reynolds averaged Navier-Stokes system of equations in Ω_t

$$\frac{\partial u_i}{\partial t} + \frac{\partial (u_i u_j)}{\partial x_j} - \frac{\partial}{\partial x_j}\Big(-p\delta_{ij} + 2\nu_{\text{eff}} S_{ij}\Big) = 0, \qquad \frac{\partial u_i}{\partial x_i} = 0, \tag{2.1}$$

where $\boldsymbol{u} = (u_1, u_2)$ is the mean part of the fluid velocity vector, $S_{ij} = \frac{1}{2}\big(\frac{\partial u_i}{\partial x_j} + \frac{\partial u_j}{\partial x_i}\big)$ are the components of $\boldsymbol{S} = \boldsymbol{S}(\boldsymbol{u})$ the symmetric part of the gradient of $\boldsymbol{u}$, p is the mean part of the kinematic pressure (i.e., the pressure divided by the constant fluid density ρ), $\nu_{\text{eff}} = \nu + \nu_T$, ν is the kinematic viscosity of the fluid (i.e. the viscosity divided by the density ρ), ν_T is a turbulent viscosity (obtained by an additional model), see [18], [32].

The system (2.1) is equipped with an initial condition $\boldsymbol{u}(x,0) = \boldsymbol{u}_0(x)$ for $x \in \Omega_0$ and with boundary conditions prescribed on the mutually disjoint parts Γ_D, Γ_O and Γ_{Wt} of the boundary $\partial\Omega = \Gamma_D \cup \Gamma_O \cup \Gamma_{Wt}$:

$$\begin{aligned} &\text{a)}\quad \boldsymbol{u} = \boldsymbol{u}_D \qquad \text{on } \Gamma_D, \qquad \text{b)}\ \boldsymbol{u} = \boldsymbol{w}_D \qquad \text{on } \Gamma_{Wt}, \\ &\text{c)}\quad -2\nu_{\text{eff}} S_{ij} n_j + p n_i = 0 \qquad \text{on } \Gamma_O, \end{aligned} \tag{2.2}$$

where $\boldsymbol{w}_D$ is the velocity of the boundary Γ_{Wt} and $\boldsymbol{u}_D$ is the prescribed inlet velocity in the form $\boldsymbol{u}_D = (U_\infty, V_g(t))^T$. Here U_∞ is the far field velocity and $V_g(t)$ is the vertical gust velocity.

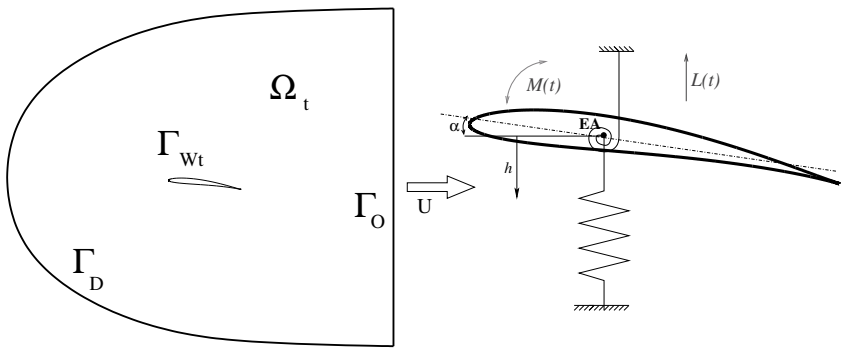

Figure 1. Sketch of the computational domain Ω_t its boundary $\partial\Omega_t$ (left) and the flexibly supported aerofoil model (right)

2.2. **SST turbulence model.** In order to enclose the system (2.1) the turbulent viscosity is modeled with the aid of SST $k-\omega$ turbulence model, see [33]. The transition is treated with the aid of the $\gamma - \overline{Re}_{\theta t}$ model is used, see [26]. The SST turbulence model is a modification of the $k-\omega$ turbulence model for which the turbulent viscosity is given by $\nu_T = \frac{k}{\omega}$ Here, the turbulent kinetic energy $k = k(x,t)$ and the turbulent specific dissipation rate $\omega = \omega(x,t)$ are modeled by

$$\begin{aligned} \frac{\partial k}{\partial t} + \frac{\partial (u_i k)}{\partial x_i} &= \gamma_{\text{eff}} P_k - \beta^* \omega k \overline{\gamma_{\text{eff}}} + \frac{\partial}{\partial x_i}\left(\varepsilon_k \frac{\partial k}{\partial x_i}\right), \\ \frac{\partial \omega}{\partial t} + \frac{\partial (u_i \omega)}{\partial x_i} &= P_\omega - \beta \omega^2 + \frac{\partial}{\partial x_i}\left(\varepsilon_\omega \frac{\partial \omega}{\partial x_i}\right) + C_D, \end{aligned} \tag{2.3}$$

where the production and the destruction terms are modified due in the first equation using the effective intermittency coefficient γ_{eff} and $\overline{\gamma}_{\text{eff}} = \max(\min(\gamma_{\text{eff}}, 1), 0.1)$. Further, the viscosity coefficients are given by $\varepsilon_k = \nu + \sigma_k \nu_T$ and $\varepsilon_\omega = \nu + \sigma_\omega \nu_T$ and the source terms P_k and C_D are defined by

$$P_k = \nu_T S_{ij} S_{ij}, \quad C_D = \frac{\sigma_D}{\omega}\Big(\frac{\partial k}{\partial x_i}\frac{\partial \omega}{\partial x_i}\Big)^+,$$

and $P_\omega = \frac{\alpha_\omega \omega}{k} P_k$. The closure coefficients β, β^*, σ_k, σ_ω, α_ω, σ_D are chosen from [33], see also [34] or [18]. Equations (2.3) are equipped with boundary conditions

$$\begin{aligned} &\text{a)} \quad k = k_\infty, \qquad \omega = \omega_\infty \qquad \text{on } \Gamma_D, \\ &\text{b)} \quad k = 0\ , \qquad \omega = \omega_{\text{wall}} \qquad \text{on } \Gamma_{Wt}, \\ &\text{c)} \quad \frac{\partial k}{\partial \boldsymbol{n}} = 0, \qquad \frac{\partial \omega}{\partial \boldsymbol{n}} = 0, \qquad \text{on } \Gamma_O. \end{aligned} \tag{2.4}$$

2.3. **Transitional model.** The transition from laminar to turbulence regimes is modeled with the aid of Menter's $\gamma - \overline{Re}_{\theta t}$ model, see [26], where the equation for the

intermittency coefficient γ reads

$$\frac{\partial \gamma}{\partial t} + \frac{\partial (u_i \gamma)}{\partial x_i} = P_\gamma - E_\gamma + \frac{\partial}{\partial x_i}\left(\left(\nu + \frac{\nu_T}{\sigma_f}\right)\frac{\partial \gamma}{\partial x_i}\right), \tag{2.5}$$

where $P_\gamma = P_{\gamma,1} - c_{e1}\gamma P_{\gamma,1}$ and $E_\gamma = c_{e2}\gamma E_{\gamma,1} - E_{\gamma,1}$ are the transition source and destruction terms, respectively. Here, we set $P_{\gamma,1} = F_{\text{length}} c_{a1} S\sqrt{\gamma F_{\text{onset}}}$, $E_{\gamma,1} = c_{a2}\Omega\gamma F_{\text{turb}}$. Further, S and Ω are the strain rate and vorticity magnitudes and the transition onset is modeled by $F_{\text{onset}} = (F_{\text{onset2}} - F_{\text{onset3}})^+$, where $F_{\text{onset2}} = \min\left(\max\left(F_{\text{onset1}}, F_{\text{onset1}}^4\right), 2\right)$, $F_{\text{onset1}} = \frac{Re_V}{2.193 Re_{\theta c}}$, $Re_V = \frac{y^2 S}{\nu}$. Further we set $F_{\text{onset3}} = \max\left(1 - \left(\frac{R_T}{2.5}\right)^3, 0\right)$, $R_T = \frac{k}{\nu\omega}$, and $F_{\text{turb}} = e^{-(R_T/4)^4}$, where y denotes the wall distance and $Re_{\theta t}$ is the transition Reynolds number. The following constants for the intermittency equation were used $c_{e1} = 1$, $c_{a1} = 2$, $c_{e2} = 50$, $c_{a2} = 0.06$, $\sigma_f = 1$. Further, $Re_{\theta c}$ is the critical Reynolds number given by an empirical correlation, and another empirical correlation is used for the function F_{length}, which controls the length of the transition region. The correlations are based on newly defined transported unknown $\overline{Re}_{\theta t}$ governed by the ALE form of the equation

$$\frac{\partial \overline{Re}_{\theta t}}{\partial t} + \frac{\partial (u_i \overline{Re}_{\theta t})}{\partial x_i} = P_{\theta t} + \frac{\partial}{\partial x_i}\left(\sigma_{\theta t}\nu_{\text{eff}}\frac{\partial \overline{Re}_{\theta t}}{\partial x_i}\right), \tag{2.6}$$

where the source term $P_{\theta t}$ is given by

$$P_{\theta t} = c_{\theta t}\frac{\rho}{t_\infty}\left(Re_{\theta t} - \overline{Re}_{\theta t}\right)(1 - F_{\theta t}),$$

$c_{\theta t} = 0.03$, $\sigma_{\theta t} = 2$, $t_\infty = 500\nu/U^2$ is the time scale, U is the local magnitude of the velocity $U = \|\boldsymbol{u}\|_2$ and the blending function $F_{\theta t}$ is defined as

$$F_{\theta t} = \min\left(1, \max\left(F_{\text{wake}} e^{-(y/\delta)^4}, 1 - \left(\frac{\gamma - 1/c_{e2}}{1 - 1/c_{e2}}\right)\right)\right),$$

$$\delta = \frac{375\Omega y}{U}\theta,\ \theta = \frac{\overline{Re}_{\theta t}\nu}{U},\ F_{\text{wake}} = e^{-(Re_\omega/10^5)^2},$$

and $Re_\omega = \frac{\omega y^2}{\nu}$. The source term $P_{\theta t}$ on the right hand side of equation (2.6) includes also the Reynolds number $Re_{\theta t}$ given by an empirical correlations.

The transitional model (2.5) and (2.6) is equipped with the boundary conditions

$$\begin{aligned} &\text{a)} \quad \gamma = 1, \qquad \overline{Re}_{\theta t} = \overline{Re}_{\theta t\infty} \qquad \text{on } \Gamma_D, \\ &\text{b)} \quad \frac{\partial \gamma}{\partial \boldsymbol{n}} = 0, \qquad \frac{\partial \overline{Re}_{\theta t}}{\partial \boldsymbol{n}} = 0 \qquad \text{on } \Gamma_{Wt} \cup \Gamma_O \end{aligned}$$

2.4. **Empirical correlations.** In order to enclose the model, the empirical correlations published in [35] are used. First, the length of the transition is controlled by $F_{\text{length}} = F_{\text{length}}(\overline{Re}_{\theta t})$. Further, the transitional onset momentum thickness Reynolds number $Re_{\theta t}$ is correlated to pressure gradient λ_θ and to turbulence intensity Tu. Further, the correlation for $Re_{\theta t}$ and for the critical Reynolds number are specified, see [35] or [24].

2.5. **ALE formulation.** In order to practically treat the motion of the domain Ω_t, the Arbitrary Lagrangian-Eulerian (ALE) method is used, see [8]. The ALE mapping $\mathcal{A} : \Omega_0^{ref} \mapsto \Omega_t$, $\mathcal{A} = \mathcal{A}(\xi, t) = \mathcal{A}_t(\xi)$ defined for all $t \in (0, T)$ and $\xi \in \Omega_0^{ref} = \Omega_0$ is assumed to be smooth and to have smooth bounded Jacobian $\mathcal{J}(x, t)$ Furthermore, by $D^{\mathcal{A}}/Dt$ the ALE derivative is denoted (i.e. the derivative with respect to the reference configuration) and $\boldsymbol{w}_D$ denotes the domain velocity (i.e. velocity of the point $x = \mathcal{A}(\xi, t)$ with a given reference $\xi \in \Omega_0^{ref}$. The ALE derivative is then related to the time derivative by (see also [9])

$$\frac{D^{\mathcal{A}} f}{Dt}(x,t) = \frac{\partial f}{\partial t}(x,t) + \boldsymbol{w}_D(x,t) \cdot \nabla f(x,t). \tag{2.7}$$

In order to approximate the equations on time dependent domains, the time derivative in equations (2.1), (2.3), (2.5) and (2.6) are replaced by the ALE time derivative using the formula (2.7), which also modifies the convection term. In the practical computation this is not complicated and thus for the sake of brevity this description is left out.

2.6. **Structure model.** The flow model is coupled with the structure model representing the flexibly supported aerofoil (see Figure 1). The aerofoil can be vertically displaced by h (downwards positive) and rotated by angle α (clockwise positive). The nonlinear equations of motion then read (see [9])

$$\begin{aligned} m\ddot{h} + S_\alpha\, \ddot{\alpha}\, \cos\alpha - S_\alpha \dot{\alpha}^2 \sin\alpha + k_h h = -L(t), \\ S_\alpha \ddot{h} \cos\alpha + I_\alpha \ddot{\alpha} + k_\alpha \alpha = M(t). \end{aligned} \tag{2.8}$$

where m is the mass of the aerofoil, S_α is the static moment around the elastic axis (EA), and I_α is the inertia moment around EA. The parameters k_h and k_α denote the stiffness coefficients. On the right-hand side the aerodynamical lift force $L(t)$ and aerodynamical torsional moment $M(t)$ are involved, which satisfy

$$L = -l \int_{\Gamma_{Wt}} \sigma_{2j} n_j \, dS, \qquad M = l \int_{\Gamma_{Wt}} \sigma_{ij} n_j r_i^{\mathrm{ort}} \, dS, \tag{2.9}$$

where $\sigma_{ij} = \rho\,[-p\delta_{ij} + 2\nu S_{ij}]$, $r_1^{\mathrm{ort}} = -(x_2 - x_2^{\mathrm{EA}})$, $r_2^{\mathrm{ort}} = x_1 - x_1^{\mathrm{EA}}$, l denotes the considered depth of the aerofoil section, and $x^{\mathrm{EA}}e = (x_1^{\mathrm{EA}}, x_2^{\mathrm{EA}})$ is the position of EA of the aerofoil at the time instant t, see Figure 1.

3. Numerical approximation

In this section, the approximation of the considered mathematical model of transitional turbulent flow is shown. The time discretization is based on the backward difference formula and for the spatial discretization the stabilized FEM is used. Further, the four equations of the transitional model are discretized in time, linearized and stabilized using the streamline upwind/Petrov Galerkin (SUPG) method. Let us moreover mention that in the computations for the $k - \omega$ equations the (nonlinear) crosswind diffusion is also applied in order to suppress non-physical undershoots/overshoots, see [19].

3.1. **Time discretization.** We consider the equidistant partition $t_j = j\Delta t$ of the time interval I with a time step $\Delta t > 0$, and denote the approximations $\boldsymbol{u}^j \approx \boldsymbol{u}(\cdot, t_j)$, $p^j \approx p(\cdot, t_j)$ and similarly $k^j = k(\cdot, t_j)$, $\omega^j = \omega(\cdot, t_j)$, $\gamma^j = \gamma(\cdot, t_j)$, $\overline{Re}_{\theta t}{}^j = \overline{Re}_{\theta t}(\cdot, t_j)$. Moreover, we approximate the domain velocity $\boldsymbol{w}_D$ at time level t_j by $\boldsymbol{w}_D^j$. We shall focus on the description of the discretization at a time instant t_{n+1}, which is kept fixed throughout this section. For the sake of simplicity the subscript t_{n+1} shall be omitted, i.e. $\Omega = \Omega_{t_{n+1}}$. Further, we shall denote by $Q = L^2(\Omega)$ the Lebesgue space, by $\boldsymbol{W} = \boldsymbol{H}^1(\Omega)$ the Sobolev space and by $\boldsymbol{X}$ the space of test functions defined by $\boldsymbol{X} = \{\boldsymbol{z} \in \boldsymbol{W} : \boldsymbol{z} = 0 \text{ on } \Gamma_D \cup \Gamma_{W t_{n+1}}\}$. Then the time derivatives in equations (2.1,2.3,2.5, 2.6) are approximated at the time $t = t_{n+1}$ by the second order backward difference formula, i.e.

$$\frac{\partial \varphi}{\partial t}\Big|_{t_{n+1}} \approx \frac{3\varphi^{n+1} - 4\varphi^n + \varphi^{n-1}}{2\Delta t}. \tag{3.1}$$

Here, let us mention that for ALE approach the ALE derivative needs to be approximated at this place.

3.2. **Spatial discretization of flow model.** The weak formulation of the time discretized Reynolds averaged Navier-Stokes equations is obtained by the multiplication of the equations (2.1) by a test function $\boldsymbol{z} \in \boldsymbol{\mathcal{X}}$, integration over the domain Ω_t, application of the Green's theorem and using approximation (3.1). The (spatial) weak formulation reads: Find $U^{n+1} = (\boldsymbol{u}^{n+1}, p^{n+1}) \in \boldsymbol{W} \times Q$ such that $\boldsymbol{u}$ approximately satisfies the boundary conditions (2.2a,b) and

$$a(U^{n+1}, V) = L(V). \tag{3.2}$$

holds for all $V = (\boldsymbol{z}, q) \in \boldsymbol{\mathcal{X}} \times Q$. The non-linear form $a(\cdot,\cdot)$ and the linear form $L(\cdot)$ are defined for any $U = (\boldsymbol{u}, p) \in \boldsymbol{W} \times Q$ and $V = (\boldsymbol{z}, q) \in \boldsymbol{\mathcal{X}} \times Q$,

$$\begin{aligned} a(U,V) &= \Big(\frac{3\boldsymbol{u}}{2\Delta t} + (\overline{\boldsymbol{w}} \cdot \nabla)\boldsymbol{u}, \boldsymbol{z}\Big)_\Omega + (\nu_{\text{eff}} \boldsymbol{S}(\boldsymbol{u}), \boldsymbol{S}(\boldsymbol{z}))_\Omega + (\nabla \cdot \boldsymbol{u}, q)_\Omega - \Big(p, \nabla \cdot \boldsymbol{z}\Big)_\Omega, \\ L(V) &= \frac{4}{2\Delta t}(\hat{\boldsymbol{u}}^n, \boldsymbol{z})_\Omega - \frac{1}{2\Delta t}\big(\hat{\boldsymbol{u}}^{n-1}, \boldsymbol{z}\big)_\Omega, \end{aligned}$$

where $\tilde{\boldsymbol{u}}^k = \boldsymbol{u}^k \circ \mathcal{A}_{t_k} \circ \mathcal{A}_{t_{n+1}}^{-1}$. In order to approximate the problem (3.2), the spaces $\boldsymbol{X}, \boldsymbol{W}$ and Q are approximated by finite element subspaces $\boldsymbol{X}_\Delta, \boldsymbol{W}_\Delta$ and Q_Δ, respectively.

Here, the Taylor-Hood family of finite elements are used, defined over an admissible triangulation $\mathcal{T}_\Delta$ of the computational domain $\Omega = \Omega_{t_{n+1}}$. In order to stabilize the method the fully stabilized scheme (see [16]) is used, which consists of SUPG and pressure stabilizing/Petrov Galerkin (PSPG) stabilization combined with the div-div stabilization, see [16].

The stabilized discrete problem reads: Find $U = (\boldsymbol{u}_\Delta^{n+1}, p_\Delta^{n+1}) \in \boldsymbol{W}_\Delta \times Q_\Delta$ such that $\boldsymbol{u}^{n+1}$ satisfies approximately the Dirichlet boundary conditions (2.2,a,b) and

$$a(U; U, V) + \mathcal{L}(U, V) + \mathcal{P}(U, V) = L(V) + \mathcal{F}(V),$$

holds for all $V = (\boldsymbol{z}, q) \in \boldsymbol{X}_\Delta \times Q_\Delta$, where the terms $\mathcal{L}$ and $\mathcal{F}$ are the SUPG/PSPG terms defined by

$$\mathcal{L}(U,V) = \sum_{K\in\mathcal{T}_\Delta} \delta_K \Big(\frac{3\boldsymbol{u}}{2\Delta t} - \nu\triangle\boldsymbol{u} + (\boldsymbol{v}\cdot\nabla)\boldsymbol{u} + \nabla p, \Psi \Big)_K,$$

$$\mathcal{F}(V) = \sum_{K\in\mathcal{T}_\Delta} \delta_K \Big(\frac{1}{2\Delta t}(4\tilde{\boldsymbol{u}}^n - \tilde{\boldsymbol{u}}^{n-1}), \Psi \Big)_K,$$

where the function $\overline{\boldsymbol{w}}^{n+1} = \boldsymbol{u}^* - \boldsymbol{w}_D^{n+1}$ stands for the transport velocity, and $\Psi = (\overline{\boldsymbol{w}}^{n+1}\cdot\nabla)\boldsymbol{z} + \nabla q$. The div-div stabilizing terms $\mathcal{P}(U,V)$ read

$$\mathcal{P}(U,V) = \sum_{K\in\mathcal{T}_\Delta} \tau_K (\nabla\cdot\boldsymbol{u}, \nabla\cdot\boldsymbol{z})_K. \tag{3.3}$$

Here, the following choice of the stabilizing parameters τ_K and δ_K based on the local element length h_K is used for the Taylor-Hood family of finite elements, $\tau_K = \max_{x\in\Omega} \|\boldsymbol{u}(x)\|_2$, $\delta_K = h_K^2/\tau_K$.

3.3. **Spatial discretization of the turbulence/transitional model.** Furthermore, the complete transitional model consisting of equations (2.3), (2.5), (2.6) is step-by-step time discretized, weakly formulated, and stabilized formulation is introduced. The time derivatives in equations (2.3), (2.5) and (2.6) are approximated using the 2nd order backward difference formula (3.1), the equations for k, ω, γ and $\overline{Re}_{\theta t}$ are multiplicated by φ_k, φ_ω, φ_γ and $\varphi_{\overline{Re}_{\theta t}}$, respectively, integrated over Ω_t, and Green's theorem is applied. The function spaces are then approximated by their finite element counterparts consisting of piecewise linear functions defined over the triangulation $\mathcal{T}_\Delta$. The stabilized formulation is obtained using a linearization of the non-linear terms and an application of the SUPG stabilization procedure.

4. Numerical results

The described method was verified using several test cases of laminar, turbulent and transitional flow, see [9], [19], [22]. Here, the method was applied to two test cases of aeroelastic simulation of flow induced aerofoil vibrations and the transient response to the sudden change of flow conditions (gust).

4.1. **Aeroelastic simulations for NACA 0012.** First, the numerical simulation of the fully coupled aeroelastic problem of flow induced vibrations of the aerofoil NACA 0012 was addressed. The following parameters of the flowing air and the profile were used: $m = 8.66\times10^{-2}$ kg, $S_\varphi = -7.797\times10^{-4}$ kg m, $I_\varphi = 4.87\times10^{-4}$ kg m^2, $k_h = 105.1$ N/m, $k_\varphi = 3.696$ N m/rad, $d = 0.05$ m, $c = 0.3$ m, $\rho = 1.225$ kg/m^3, $\nu = 1.5\times10^{-5}$ m/s^2, see also [9]. The elastic axis EA is located at 40% of the profile. The numerical simulation was performed for the sub- and also close to critical far field velocity $U_\infty = 37.7$ m s^{-1} determined by a linear approach.

The verification of the applied numerical method was done with the main attention paid to the resulting aeroelastic response. Figure 2 shows the aeroelastic response of

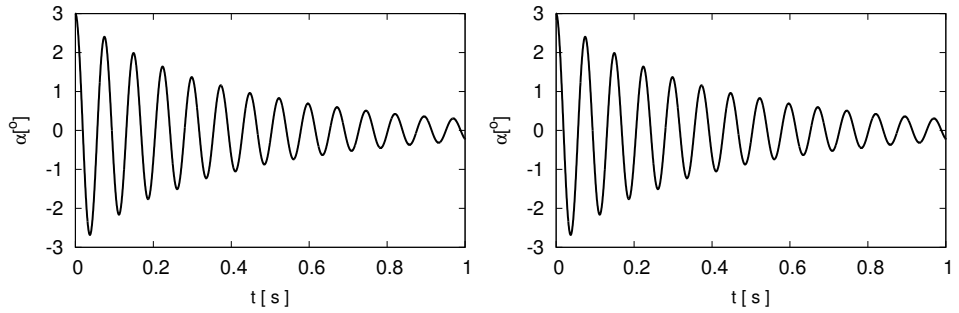

Figure 2. Aeroelastic response of NACA 0012 aerofoil for sub-critical far field velocity $U_\infty = 10\,\mathrm{m/s}$

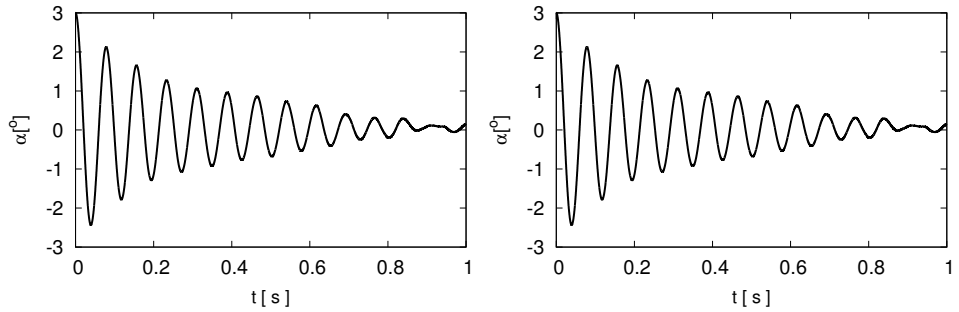

Figure 3. Aeroelastic response of NACA 0012 aerofoil for sub-critical far field velocity $U_\infty = 20\,\mathrm{m/s}$

the fully coupled FSI problem for far field velocity $U_\infty = 10\mathrm{m/s}$. The aeroelastic response predict stronger aerodynamical damping for flow velocity $U_\infty = 20\,\mathrm{m/s}$, see Figure 3. For higher flow velocities closer to the critical velocity the aeroelastic response seems to predict again decrease of the aerodynamical damping for $U_\infty = 35\,\mathrm{m/s}$, see Figure 4. For $U_\infty = 38\,\mathrm{m/s}$ the aeroelastic system is only weakly damped, see Figure 5, which agrees well with the results in the literature.

4.2. **Gust response.** The developed numerical method was applied on numerical approximation of flow around a flexibly supported aerofoil subject to the change of flow conditions, see [21]. The results are compared with the previous study of the authors [20], where turbulent and non-turbulent flows were considered without modelling of the turbulent-laminar flow transition. The considered aerofoil shape is given by

$$z = \frac{k_{\mathrm{KT}}(c_{\mathrm{KT}} - 1)}{((Z-1)/(Z - c_{\mathrm{KT}}))^{k_{\mathrm{KT}}} - 1}, \qquad k_{\mathrm{KT}} = \frac{360 - \alpha_T}{180}$$

where $Z = X + iY$ and $z = x + iy$ are complex variables describing the unit circle and the aerofoil shape in $X - Y$ and $x - y$ complex planes, respectively. The constants $c_{\mathrm{KT}} = -0.89 - 0.11i$ and $\alpha_T = 2\,\mathrm{deg}$ determine the aerofoil shape (A1), see Figure 1. The following values were used $m = 2 \times 10^{-4}\,\mathrm{kg}$, $I_\alpha = 1.2 \times 10^{-7}\,\mathrm{kg\ m^2}$ and $S_\alpha =$

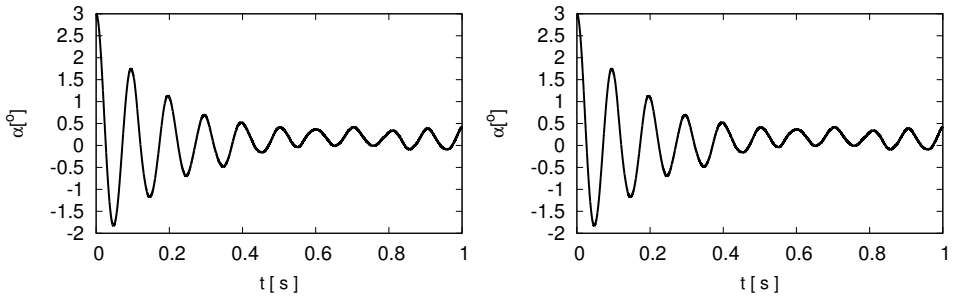

Figure 4. Aeroelastic response of NACA 0012 aerofoil for sub-critical far field velocity $U_\infty = 35\,\mathrm{m/s}$

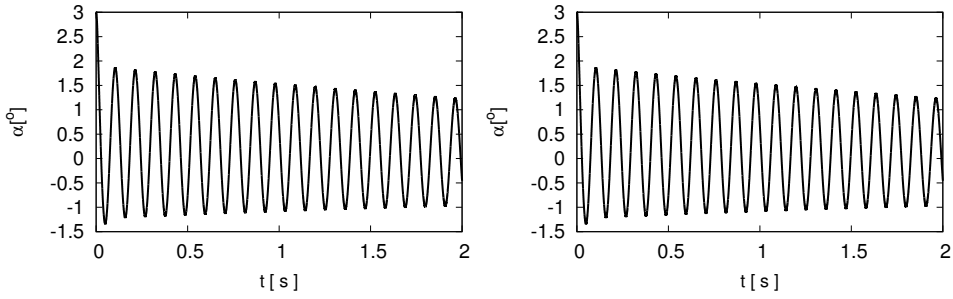

Figure 5. Aeroelastic response of NACA 0012 aerofoil for sub-critical far field velocity $U_\infty = 38\,\mathrm{m/s}$

$2 \times 10^{-6}\,\mathrm{kg\,m}$. The aerofoil chord was $c = 0.1\,m$, the elastic axis was located at 30 % of the chord, and the depth of the aerofoil section was $l = 0.03\,\mathrm{m}$. The stiffness coefficients of the springs were $k_h = 26\,\mathrm{N/m}$, $k_\alpha = 0.29\,\mathrm{N\,m/rad}$.

The air density was $\rho = 1.225\,\mathrm{kg\,m^{-3}}$ and the air kinematic viscosity was $\nu = 1.453 \times 10^{-5}\,\mathrm{m^2/s}$. The inlet turbulence intensity was 1% ($k = 1.5 \times 10^{-4}\,U_\infty^2$, $\omega = 10\,\mathrm{s^{-1}}$ on Γ_I). The finite element triangular mesh was used, anisotropically refined nearby the boundary in order to well capture the turbulent boundary layer, wake and also the separation region. The described stabilized FEM was used, and the computations were performed on the coarse and the fine mesh. A vertical gust of $1\,s$ duration was considered as a sudden perturbation of the inlet velocity $U_\infty = 15\,\mathrm{m/s}$, i.e.

$$V_g(t) = \frac{V_G}{2}\,(1 + \cos(\pi(t - t_0)))$$

for $t \in [t_0, t_0 + 1]$ and $V_g(t) \equiv 0$ otherwise. Here, $V_G = 1.5\,\mathrm{m\,s^{-1}}$ and $V_G = 5\,\mathrm{m\,s^{-1}}$ were considered for the light and heavy gusts, respectively. The aeroelastic aerofoil responses $h(t)$ and $\alpha(t)$ numerically simulated in the time domain for the light gust are shown in Figure 6. The numerically simulated aerofoil responses $h(t)$ and $\alpha(t)$ for the heavy gust are shown in Figure 7. The results for the transitional flow model are close to the simulations using the turbulence model, but before the gust starts and

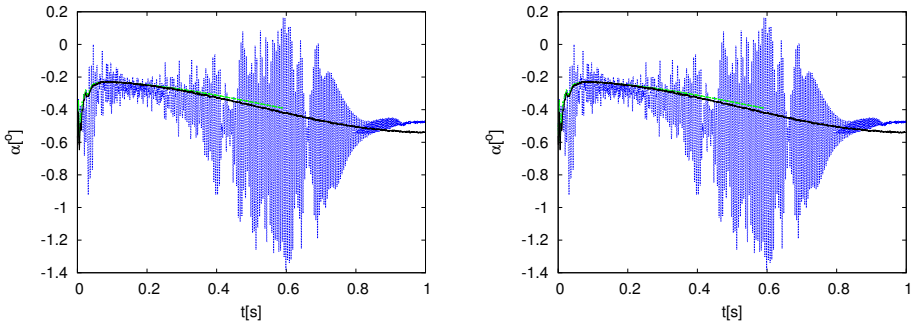

Figure 6. Aeroelastic response to the light gust: Comparison of results computed by laminar, turbulent and transitional models

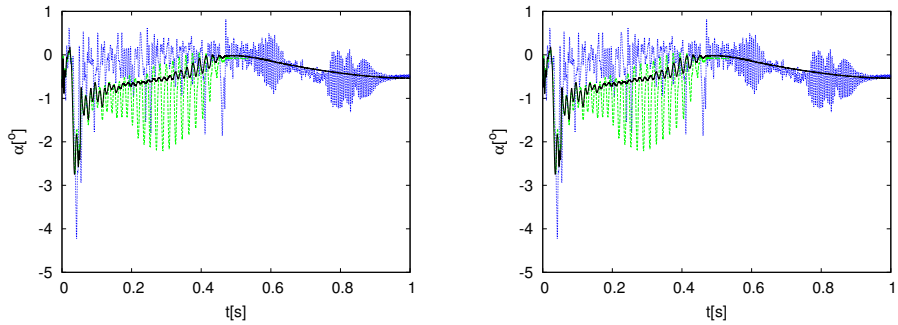

Figure 7. Aeroelastic response to the heavy gust: Comparison of results computed by laminar, turbulent and transitional models

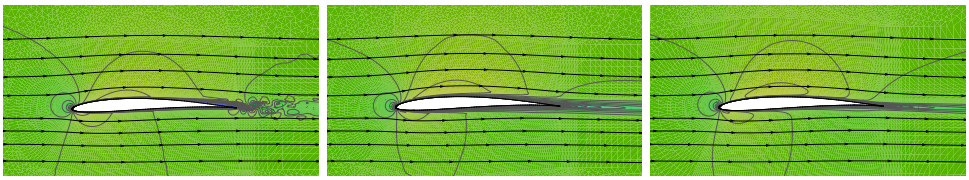

Figure 8. Comparison of velocity flow patterns for the laminar (left), turbulent (middle) and transitional(right) models just before the gust starts

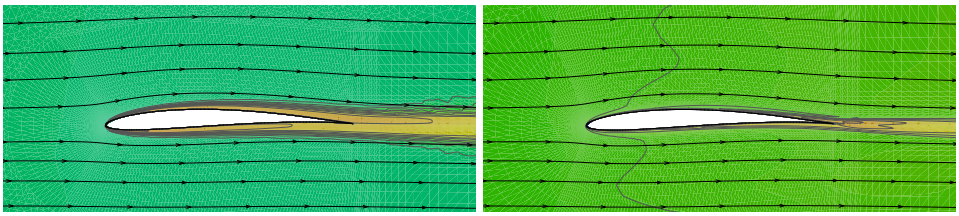

Figure 9. Comparison of the turbulent kinetic energy k distribution for the turbulent (left) and transitional (right) models just before the gust starts

also when it disappears, the fluid flow becomes almost laminar on the aerofoil surface. The comparison of the flow velocity patterns just before the gust starts computed by the laminar, turbulent and transitional model are shown in Figure 8. See also turbulent kinetic energy pattern at the same time instant shown in Figure 9, where the most of the turbulent kinetic energy for the transitional model is in a far wake and almost zero turbulent kinetic energy is at the aerofoil surface. On the other hand

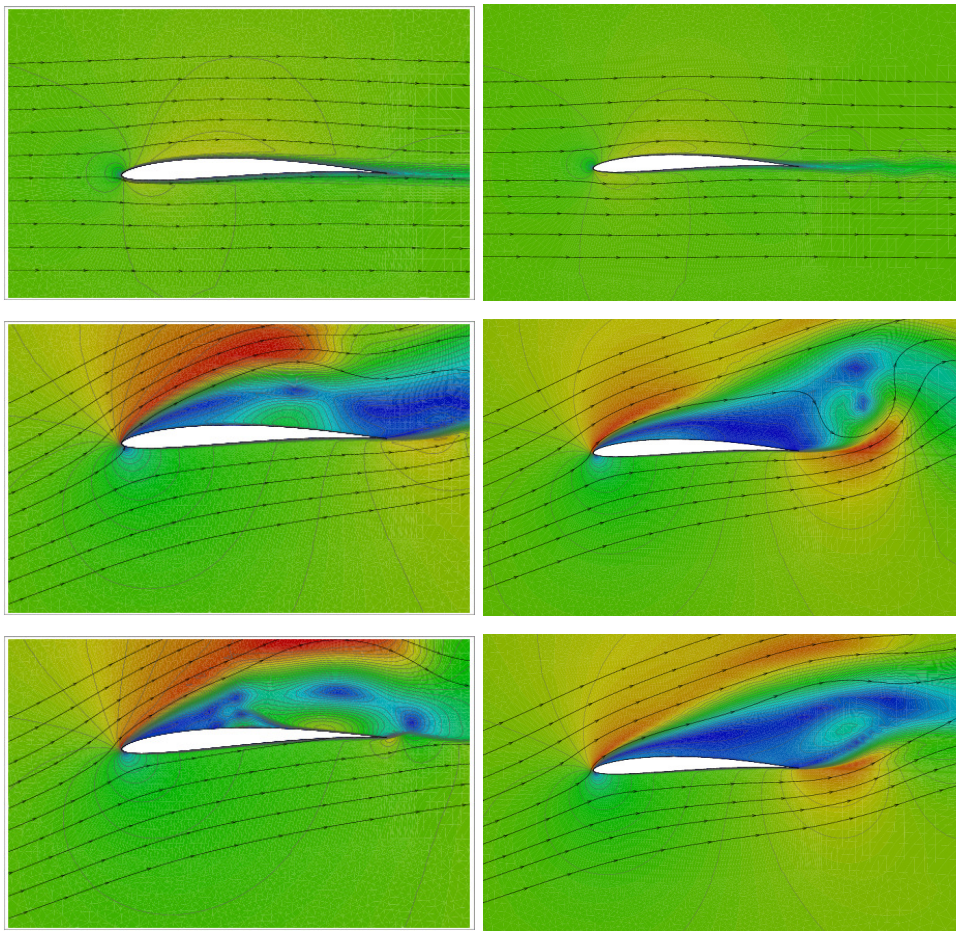

Figure 10. Heavy gust aeroelastic response: comparison of flow velocity patterns for turbulent (left) and transitional (right) models at three time instants

the flow velocity patterns shown in Figure 10 indicate that the transitional model is much closer to the turbulent model for high displacement of the aerofoil.

5. Conclusion

A new original FEM taking into account transition of the laminar to turbulent flow was developed and successfully applied on the FSI problem of flow induced vibrations for a 2-DOF aerofoil. The results were computed by the developed in-house software and the fully coupled FSI problem was solved. In addition to implementation of the laminar-turbulent flow transition, the developed method was also modified for application in the case of case of time dependent computational domain using the ALE method. First, the aeroelastic simulation were performed for the NACA 0012 aerofoil, whose vibrations were induced by the prescribed initial conditions. The results of the transitional model agree well with the reference results [9]. Further, the simulation of an 2-DOF aerofoil loaded by a sudden gust was performed. The results of the described method was compared with reference results [21]. The transitional model was shown to "switch" between the laminar/turbulent model in dependence on the displacements, i.e. the results of the transitional model correspond better to the results of the laminar model for the case of small displacements (light gust), whereas for large displacements (heavy gust) the results agree better with the results obtained by the fully turbulent model. This influence is particularly important for small displacements (light gust case).

Acknowledgment. This work was supported by project No. P101/12/1271 of the Czech Science Foundation.

References

1. Dowell, E. H. and Clark, R. N.: *A Modern Course in Aeroelasticity*. Solid mechanics and its applications, Kluwer Academic Publishers, Dordrecht, Boston, 2004.
2. Verhoosel, C., Scholcz, T., and Hulshoff, S.: Uncertainty and reliability analysis of fluid-structure stability boundaries. *AIAA Journal*, **47**, (2009), 91–104.
3. Jones, D. and Gaitonde, A.: Future fast methods for loads calculations: The 'FFAST' project. In D. Knorzer and J. Szodruch (eds.), *Innovation for Sustainable Aviation in a Global Environment*, pp. 110–115, IOS Press BV, 2012.
4. Berci, M., Gaskell, P. H., Hewson, R., and Toropov, V.: A semi-analytical model for the combined aeroelastic behaviour and gust response of a flexible aerofoil. *Journal of Fluids and Structures*, **38**, (2013), 3–21.
5. Sucipto, T., Berci, M., and Krier, J.: Gust response of a flexible typical section via high- and (tuned) low-fidelity simulations. *Computers & Structures*, **122**, (2013), 202–216.
6. Vos, J., Rizzi, A., Darracq, D., and Hirschel, E.: Navier-Stokes solvers in European aircraft design. *Progress in Aerospace Sciences*, **38**(8), (2002), 601–697.
7. Bukač, M., Čanič, S., and Muha, B.: A partitioned scheme for fluid-composite structure interaction problems. *Journal of Computational Physics*, **281**, (2015), 493–517.
8. Nomura, T. and Hughes, T. J. R.: An arbitrary Lagrangian-Eulerian finite element method for interaction of fluid and a rigid body. *Computer Methods in Applied Mechanics and Engineering*, **95**, (1992), 115–138.

9. Sváček, P., Feistauer, M., and Horáček, J.: Numerical simulation of flow induced airfoil vibrations with large amplitudes. *Journal of Fluids and Structures*, **23**(3), (2007), 391–411.

10. Boffi, D. and Gastaldi, L.: Stability and geometric conservation laws for ALE formulations. *Computational Methods in Applied Mechanical Engineering*, **193**, (2004), 4717–4739.

11. Farhat, C. and Geuzaine, P.: Design and analysis of robust ALE time-integrators for the solution of unsteady flow problems on moving grids. *Computational Methods in Applied Mechanical Engineering*, **193**, (2004), 4073–4095.

12. Gresho, P. M. and Sani, R. L.: *Incompressible Flow and the Finite Element Method.* Wiley, Chichester, 2000.

13. Roos, H.-G., Stynes, M., and Tobiska, L.: *Robust Numerical Methods for Singulary Perturbed Differential Equations: Convection Diffusion and Flow Problems*, vol. 24. Springer, Berlin, Heidelberg, 2008.

14. Lube, G. and Rapin, G.: Residual-based stabilized higher-order FEM for advection-dominated problems. *Computer Methods in Applied Mechanics and Engineering*, **195**(33-36), (2006), 4124–4138.

15. Linke, A., Rebholz, L. G., and Wilson, N. E.: On the convergence rate of grad-div stabilized Taylor-Hood to Scott-Vogelius solutions for incompressible flow problems. *Journal of Mathematical Analysis and Applications*, **381**(2), (2011), 612–626.

16. Gelhard, T., Lube, G., Olshanskii, M. A., and Starcke, J.-H.: Stabilized finite element schemes with LBB-stable elements for incompressible flows. *Journal of Computational and Applied Mathematics*, **177**, (2005), 243–267.

17. Feistauer, M., Horáček, J., Růžička, M., and Sváček, P.: Numerical analysis of flow-induced nonlinear vibrations of an airfoil with three degrees of freedom. *Computers & Fluids*, **49**(1), (2011), 110 – 127.

18. Wilcox, D. C.: *Turbulence Modeling for CFD.* DCW Industries, 1993.

19. Feistauer, M., Horáček, J., and Sváček, P.: Numerical simulation of vibrations of an airfoil induced by turbulent flow. *Communications in Computational Physics*, **17**(1), (2015), 146–188.

20. Sváček, P. and Horáček, J.: On mathematical modeling of fluid–structure interactions with nonlinear effects: Finite element approximations of gust response. *Journal of Computational and Applied Mathematics*, **273**(0), (2015), 394 – 403.

21. Berci, M., Mascetti, S., Incognito, A., Gaskell, P. H., and Toropov, V. V.: Gust response of a typical section via CFD and analytical solutions. In J. C. F. Pereira and A. Sequeira (eds.), *ECCOMAS CFD 2010, V. European Conference on Computational Fluid Dynamics*, 2010, p. 10 pp.

22. Horáček, J. and Sváček, P.: Finite element simulation of a gust response of an ultralight 2-DOF airfoil. In *Proceedings of the ASME 2014 Pressure Vessels & Piping Conference*, PVP2014-28390, Anaheim, California, USA, 2014, 10 pp.

23. Walters, D. K. and Cokljat, D.: A three-equation eddy-viscosity model for Reynolds-averaged Navier-Stokes simulations of transitional flow. *Journal of Fluids Engineering*, **130**(12), (2008), 121401.

24. Suluksna, K. and Juntasaro, E.: Assessment of intermittency transport equations for modeling transition in boundary layers subjected to freestream turbulence. *International Journal of Heat and Fluid Flow*, **29**(1), (2008), 48 – 61.

25. Suzen, Y., Huang, P., Hultgren, L., and Ashpis, D.: Predictions of separated and transitional boundary layers under low-pressure turbine airfoil conditions using an intermittency transport equation. *Journal of Turbomachinary-Transactions of the ASME*, **125**(3), (2003), 455–464.

26. Menter, F., Langtry, R., and Völker, S.: Transition modelling for general purpose CFD codes. *Flow, Turbulence and Combustion*, **77**(1-4), (2006), 277–303.

27. Suzen, Y., Huang, P., Hultgren, L. S., and Ashpis, D. E.: Predictions of separated and transitional boundary layers under low-pressure turbine airfoil conditions using an intermittency transport equation. *Journal of Turbomachinery*, **125**(3), (2003), 455–464.

28. Kim, S. W., Zaman, K. B. M. Q., and Panda, J.: Numerical investigation of unsteady transitional flow over oscillating airfoil. *Journal of Fluids Engineering-Transactions of the ASME*, **117**(1), (1995), 10–16.

29. Weber, S., Jones, K., Ekaterinaris, J., and Platzer, M.: Transonic flutter computations for the NLR 7301 supercritical airfoil. *Aerospace Science and Technology*, **5**, (2001), 293–304.

30. Poirel, D., Métivier, V., and Dumas, G.: Computational aeroelastic simulations of self-sustained pitch oscillations of a NACA0012 at transitional Reynolds numbers. *Journal of Fluids and Structures*, **27**, (2011), 1262–1277.

31. Yuan, W., Poirel, D., Wang, B., and Benaissa, A.: Effect of freestream turbulence on airfoil limit-cycle oscillations at transitional Reynolds numbers. *Journal of Aircraft*, **52**(4), (2015), 1214–1225.

32. Pope, S. B.: *Turbulent Flows*. Cambridge University Press, Cambridge, 2000.

33. Menter, F. R.: Two-equations eddy-viscosity turbulence models for engineering applications. *AIAA Journal*, **32**(8), (1994), 1598–1605.

34. Kok, J. C.: *Resolving the dependence on free-stream values for the k-omega turbulence model*. Tech. rep., National Aerospace Laboratory NLR, 1999.

35. Langtry, R. B. and Menter, F. R.: Correlation-based transition modeling for unstructured parallelized computational fluid dynamics codes. *AIAA Journal*, **47**(12), (2009), 2894–2906.

Notes for Contributors

to the Journal of Computational and Applied Mechanics

Aims and scope. The aim of the journal is to publish research papers on theoretical and applied mechanics. Special emphasis is given to articles on computational mechanics, continuum mechanics (mechanics of solid bodies, fluid mechanics, heat and mass transfer) and dynamics. Review papers on a research field and materials effective for teaching can also be accepted and are published as review papers or classroom notes. Papers devoted to mathematical problems relevant to mechanics will also be considered.

Frequency of the journal. Two issues a year (approximately 80 pages per issue).

Submission of Manuscripts. Submission of a manuscript implies that the paper has not been published, nor is being considered for publication elsewhere. Papers should be written in standard grammatical English. The manuscript is to be submitted in electronic, preferably in pdf, format. The text is to be 130 mm wide and 190 mm long and the main text should be typeset in 10pt CMR fonts. Though the length of a paper is not prescribed, authors are encouraged to write concisely. However, short communications or discussions on papers published in the journal must not be longer than 2 pages. Each manuscript should be provided with an English Abstract of about 50–70 words, reporting concisely on the objective and results of the paper. The Abstract is followed by the Mathematical Subject Classification – in case the author (or authors) give the classification codes – then the keywords (no more than five). References should be grouped at the end of the paper in numerical order of appearance. Author's name(s) and initials, paper titles, journal name, volume, issue, year and page numbers should be given for all journals referenced.

The journal prefers the submission of manuscripts in LaTeX. Authors should prefer the $\mathcal{AMS}$-LaTeX article class and are not recommended to define their own LaTeX commands. Visit our home page for further details concerning how to edit your paper.

For the purpose of refereeing the manuscripts should be sent either to Balázs Tóth (Balazs.TOTH@uni-miskolc.hu) or György SZEIDL (Gyorgy.SZEIDL@uni-miskolc.hu).

The eventual supply of an accepted for publication paper in its final camera-ready form will ensure more rapid publication. Format requirements are provided by the home page of the journal from which sample LaTeX files can be downloaded:

http://www.mech.uni-miskolc.hu/jcam

These sample files can also be obtained directly (via e-mail) from Balázs TÓTH (Balazs.TOTH@uni-miskolc.hu), upon request.

One issue of the journal and ten offprints will be provided free of charge and mailed to the correspondent author. Since JCAM is an open access journal each paper can be downloaded freely from the homepage of the journal.

The Journal of Computational and Applied Mechanics is abstracted in Zentralblatt für Mathematik and in the Russian Referativnij Zhurnal.

Secretariat of the Vice-Rector for Research and International Relations, University of Miskolc
Responsible for publication: Prof. Dr. Tamás Kékesi
Published by the Miskolc University Press under the leadership of Attila Szendi
Responsible for duplication: Works manager Erzsébet Pásztor
Number of copies printed: 75
Put to the Press on December 6, 2016
Number of permission: TNRT 2016-380-ME **HU ISSN 1586–2070**

A Short History of the Publications of the University of Miskolc

The University of Miskolc (Hungary) is an important center of research in Central Europe. Its parent university was founded by the Empress Maria Teresia in Selmecbánya (today Banska Štiavnica, Slovakia) in 1735. After the first World War the legal predecessor of the University of Miskolc moved to Sopron (Hungary) where, in 1929, it started the series of university publications with the title *Publications of the Mining and Metallurgical Division of the Hungarian Academy of Mining and Forestry Engineering* (Volumes I.-VI.). From 1934 to 1947 the Institution had the name Faculty of Mining, Metallurgical and Forestry Engineering of the József Nádor University of Technology and Economic Sciences at Sopron. Accordingly, the publications were given the title *Publications of the Mining and Metallurgical Engineering Division* (Volumes VII.-XVI.). For the last volume before 1950 – due to a further change in the name of the Institution – *Technical University, Faculties of Mining, Metallurgical and Forestry Engineering, Publications of the Mining and Metallurgical Divisions* was the title.

For some years after 1950 the Publications were temporarily suspended.

After the foundation of the Mechanical Engineering Faculty in Miskolc in 1949 and the movement of the Sopron Mining and Metallurgical Faculties to Miskolc, the Publications restarted with the general title *Publications of the Technical University of Heavy Industry* in 1955. Four new series - Series A (Mining), Series B (Metallurgy), Series C (Machinery) and Series D (Natural Sciences) - were founded in 1976. These came out both in foreign languages (English, German and Russian) and in Hungarian.

In 1990, right after the foundation of some new faculties, the university was renamed to University of Miskolc. At the same time the structure of the Publications was reorganized so that it could follow the faculty structure. Accordingly three new series were established: Series E (Legal Sciences), Series F (Economic Sciences) and Series G (Humanities and Social Sciences). The latest series, i.e., the series H (European Integration Studies) was founded in 2001. The eight series are formed by some periodicals and such publications which come out with various frequencies.

Papers on computational and applied mechanics were published in the

Publications of the University of Miskolc, Series D, Natural Sciences.

This series was given the name Natural Sciences, Mathematics in 1995. The name change reflects the fact that most of the papers published in the journal are of mathematical nature though papers on mechanics also come out.

The series

Publications of the University of Miskolc, Series C, Fundamental Engineering Sciences

founded in 1995 also published papers on mechanical issues. The present journal, which is published with the support of the Faculty of Mechanical Engineering and Informatics as a member of the Series C (Machinery), is the legal successor of the above journal.

Journal of Computational and Applied Mechanics

Volume 11, Number 2 (2016)

Contents

Contributed Papers